IMT School for Advanced Studies, Lucca
Lucca, Italy

Multi-scale and nonlinear simulation methods for cellulose materials and applications to paper

PhD Program in Systems Science

Track in Computational Mechanics

XXXVIII Cycle

By

Mohadeseh Fallah Yakhdani

2026

The dissertation of Mohadeseh Fallah Yakhdani is approved.

PhD Program Coordinator: Alberto Bemporad, IMT School for Advanced Studies Lucca

Advisor: Prof. Marco Paggi, IMT School for Advanced Studies Lucca

Co-Advisor: Prof. Pietro Lenarda, IMT School for Advanced Studies Lucca

The dissertation of Mohadeseh Fallah Yakhdani has been reviewed by:

Prof. Andrea Bacigalupo, Università di Genova

Prof. Emanuela Bosco, Eindhoven University of Technology

Prof. Mauro Corrado, Politecnico di Torino

IMT School for Advanced Studies Lucca
2026

Contents

List of Figures

List of Tables

Acknowledgements

I would like to express my deepest gratitude to my supervisor, Professor Marco Paggi, for his exceptional guidance, unwavering support, and inspiring mentorship throughout my PhD journey. His professionalism, patience, and profound knowledge have been invaluable to both my academic and personal growth. More than a supervisor, he has been a true mentor, illuminating the often complex and uncertain path of research and providing motivation at every step. I am sincerely thankful for his trust, advice, and the exemplary model he has set as a scientist and as a person.

I am also deeply grateful to my co-advisor, Professor Pietro Lenarda, for his insightful discussions, constructive feedback, and continuous support throughout the development of this work.

I would like to extend my sincere thanks to Dr. Hamed Zarei for his valuable collaboration on the experimental work presented in Chapter 2, which is co-authored with him. His guidance and assistance were instrumental in achieving the results reported in the corresponding published paper.

Finally, I owe my heartfelt gratitude to my family. My husband's constant support, understanding, and encouragement have sustained me throughout this demanding journey, and his belief in me has given me the strength to overcome many challenges. My deepest love and gratitude go to my son, whose patience, kindness, and cooperation—especially during periods when my attention was devoted to research—have been a continuous source of inspiration and motivation. This achievement belongs to them as much as it does to me.

Vita

June 01, 1992	Born, Yazd, Iran
2013	Bachelor's Degree in Mechanical Engineering Sharif University of Technology Tehran, Iran
2015	Research Fellow University of Bologna Bologna, Italy
2017	Master's Degree in Applied Mechanics University of Tehran Tehran, Iran
2026	PhD in Systems Science, Computational Mechanics IMT School for Advanced Studies Lucca Lucca, Italy

Publications

1. M. Fallah, H. Zarei, M. Paggi, “A novel in- situ micro-mechanical testing of paper fracture and its stochastic network model,” in *International Journal of Solids and Structures*, vol. 300, pp. 112 – 930, 2024.
2. M. Fallah, P. Lenarda, M. Paggi,“Nonlinear anisotropic hypo-elastic continuum models for paper materials and their relation to statistical micromechanics,” *Engineering Fracture Mechanics*, vol. 326, pp. 111 – 325, 2025.
3. M. Fallah, M. Paggi,“Modelling and experiments of filament-reinforced paper for sustainable packaging,” *submitted for publication*.

Presentations

1. M. Fallah, H. Zarei, M. Paggi, "A novel in-situ micro-mechanical testing campaign on paper fracture and its statistical mechanics model," in *Euromech Colloquium 634 – Multi-physics of fibrous networks and fiber-composite materials*, Eindhoven, The Netherlands, 2023.
2. M. Fallah, H. Zarei, M. Paggi, "A two-scale finite element model of paper materials based on a statistical physics microscale approach," in *International paper physics conference*, Wuppertal, Germany, 2024.
3. M. Fallah, P. Lenarda, M. Paggi, "A nonlinear anisotropic hypo-elastic continuum model for paper materials and its relation to statistical micromechanics," in *XVIII International Conference on Computational Plasticity, COMPLAS*, Barcelona, Spain, 2025.

Abstract

Paper is a sustainable and versatile material, yet its mechanical behavior (how it deforms and fractures) is complex. This complexity arises because paper is not uniform; it is composed of countless microscopic cellulose fibers with varying orientations and bonding conditions. Understanding how these fibers interact to carry loads and resist fracture is essential for improving paper-based products and developing greener alternatives to plastics.

This thesis presents an integrated experimental and modeling approach that connects the microscopic behavior of fibers with the overall mechanical response of paper and paperboard. At the microscale, specialized experiments and imaging techniques were used to observe how fibers stretch, bend, and separate during loading. These observations guided the development of a stochastic micromechanical model capable of describing the random fiber network and predicting its non-linear response and fracture behavior.

Building on this foundation, two continuum-scale models were proposed to predict the behavior of paper under complex loading conditions while preserving a clear link to the fiber-scale mechanisms. The same framework was extended to reinforced gummed papers, demonstrating that natural fibers such as flax can effectively replace synthetic glass fibers as sustainable reinforcements. Finally, experiments on paperboard with different fiber orientations confirmed the strong connection between material anisotropy and fracture direction, validating the predictive capability of the developed models.

Chapter 1

Introduction

1.1 Background and motivation

Paper and paperboard materials represent one of the most significant achievements in human engineering history, combining natural renewability with remarkable versatility. Originally developed as media for writing and communication, these cellulose-based materials have evolved into indispensable components in modern applications ranging from advanced packaging and flexible electronics to structural reinforcements [1, 2]. Their mechanical performance—lightweight, stiff, and recyclable—has positioned them as ideal candidates for replacing petroleum-based plastics and composites in many industrial sectors [3].

In recent years, the global shift toward sustainability and circular economy principles has significantly accelerated interest in paper-based materials, particularly within the packaging industry. The EC directive 904/2019 on single-use plastics gave an impulse to the use of paper and paperboard for packaging [4], with an expected market compounded average growth rate of about 5% from 2023 to 2030. This legislative momentum reflects a broader societal commitment to reducing plastic waste and minimizing dependence on fossil-based resources.

Within this evolving landscape, the mechanical performance of paper materials is critical—not only for ensuring structural integrity but also for meeting functional and user-centric demands [5]. Packaging applications increasingly require materials that are not only sustainable but also robust, durable, and mechanically reliable [6]. Among bio-based alternatives, paper and paperboard, derived from renewable cellulose fibers, stand out as some of the earliest and most extensively utilized packaging materials. Their inherent recyclability and biodegradability make them central to efforts aimed at reducing plastic dependency and advancing eco-friendly packaging technologies [7]. Advancing our understanding of their mechanical behavior is therefore vital to ensuring performance reliability and enabling the design of next-generation paper-based products capable of meeting increasingly demanding engineering requirements.

Structurally, paper belongs to the class of random fibrous materials, whose structure consists of a disordered network of interconnected fibers joined through adhesive bonds and cross-links. The mechanical response of such networks arises not only from the intrinsic properties of individual fibers but also from their geometric arrangement and interactions within the network. Parameters such as fiber orientation, density, cross-link distribution, and bonding strength collectively determine how the load is transferred and how deformation evolves under stress. Consequently, the inherent structural disorder and network connectivity make fibrous materials—such as paper—highly sensitive to their micro-structural configuration, leading to nonlinear and direction-dependent mechanical behavior[8, 9, 10].

Understanding and modeling this behavior remain challenging due to the multi-scale and stochastic nature of paper mechanics. At the microscale, the properties of individual fibers and their bonds determine local deformation mechanisms such as slippage, debonding, and breakage. At the macroscale, the collective response of the fiber network manifests as anisotropy, nonlinearity, and damage localization. Bridging these scales requires a multi-scale framework capable of connecting measurable microstructural characteristics to the overall continuum response [11].

The growing global emphasis on sustainability, circular economy, and environmental stewardship has renewed scientific interest in cellulose-based materials. Paper and paperboard are renewable, recyclable, and biodegradable, offering a clear ecological advantage over conventional synthetic polymers [12, 13]. However, extending their use to load-bearing and structural applications requires a deeper understanding of their mechanical behavior, as well as reliable predictive models capable of guiding the design of next-generation paper-based composites and reinforcements.

This thesis addresses these needs by developing and validating multiscale and nonlinear computational frameworks for paper and paperboard materials. The work integrates experimental evidence with micromechanical and continuum modeling, aiming to establish physically grounded constitutive descriptions of cellulose networks and their reinforced variants. Through this approach, the work aims to support the design and optimization of sustainable, high-performance paper-based materials for advanced engineering applications.

1.2 Historical overview of papermaking and fiber technology

Papermaking originated in China during the Western Han Dynasty and is traditionally credited to Cai Lun around 105 CE, who developed a process using plant fibers such as mulberry bark, hemp, rags, and fishnets. This invention revolutionized communication and documentation, as it enabled the production of lightweight, flexible, and affordable writing materials. The technology gradually spread across East Asia, reaching Korea by the 4th–5th centuries and Japan by the 7th century, where local adaptations led to unique varieties of handmade paper made from mulberry, cane, hemp, and bark fibers. Over time, papermaking techniques diffused westward to the Arab world and later to Europe, where parchment from animal hides remained common until the mastery of white paper production in the 17th century. The spread of papermaking was initially slow but accelerated after the invention of the printing press in 1440, which fueled the growing demand for paper. By the late 16th and 17th centuries, papermills were established in North America, continuing the evolution of this craft through the adaptation of European methods to local resources. Thus, the history of papermaking reflects a continuous process of technological exchange, material innovation, and cultural adaptation that shaped written communication across civilizations [14, 15].

As the craft advanced, papermaking gradually transformed into an industrial process driven by technological innovation. After spreading from China to the Arab world and Europe, key milestones—such as the introduction of watermills for pulp preparation and the invention of Louis Robert's papermaking machine in 1799—marked the shift from manual to mass production. The later use of wood and recycled fibers further enhanced efficiency and sustainability, establishing papermaking as a cornerstone of global communication and industry [16].

The papermaking process today is a highly integrated sequence of mechanical and chemical operations that convert raw fibrous materials into paper or paperboard. It begins with stock preparation, during which dry pulp or recycled paper is dispersed in water and mechanically refined to form a uniform fiber suspension. This suspension is then distributed onto a moving forming fabric, where water is drained to create a continuous wet web of interlaced fibers. In the subsequent pressing stage, the web is mechanically compacted to remove additional water and enhance fiber bonding, increasing the solids content to about 38–50%. The partially dried sheet then passes through heated drying cylinders, where remaining moisture is evaporated until the paper reaches a final moisture content between 2% and 10%. Finally, the calendering process smooths and densifies the surface, after which the paper is reeled into large rolls for further conversion or distribution [17].

The pulp and paper industry's raw materials are commonly classified into three categories: wood, non-wood, and non-plant (primarily recycled paper) sources [18]. Pulp and papermaking technology, which began China, originally relied on non-wood sources like textile rags. As the industry evolved, materials such as cereal straw, reeds, grasses, and bagasse became essential in regions with limited forest resources, especially across Asia. Today, although wood usage dominates, non-wood pulp production remains crucial in countries with limited forests, including China, India, and Egypt. This shift has also driven rapid advancements in pulping methods, marking a new era in the industry. Wood pulp accounts for 63% of global consumption, recycled pulp 34%, and non-wood pulp only 3%. Expanding the use of non-wood fibers could improve the sustainability and resource efficiency of the industry. Notably, fibers like flax, hemp, jute, kenaf, cotton, sisal, and abaca offer properties that resemble or even exceed those of softwood fibers, making them strong candidates for future material sourcing [19].

The use of agricultural residues in the pulp and paper industry is increasingly popular due to their abundance, low cost, and potential to produce fibers with qualities comparable to hardwoods. Cotton stalks, in particular, are a promising agricultural residue, offering mechanical properties similar to commonly used hardwood species. After cotton fibers are harvested, the remaining stalks provide fibers well-suited for paper production, particleboards, and corrugated boards. With fiber dimensions analogous to hardwood, cotton stalk fibers exhibit desirable tensile characteristics and flexibility, making them an effective alternative raw material for sustainable papermaking in regions with limited wood resources [20, 21].

[22] investigated the potential of textile fibers like cotton and silk as sustainable reinforcement materials in composites. Cotton fibers, high in cellulose content, provide substantial strength and tensile properties, while silk offers exceptional tensile strength and flexibility, presenting a promising alternative to synthetic fibers. The distinct mechanical performance of these natural fibers, attributed to their unique structure and composition, positions them as viable options for applications in industries such as automotive and biomedical, supporting a shift toward eco-friendly materials.

[23] investigate the paper-making properties of non-wood pulps, particularly highlighting the runnability of these materials in pilot-scale paper machines operating at high speeds (1100–1380 m/min). Their findings demonstrate that high-quality paper can be produced from non-wood pulp, specifically reed, with dewatering properties comparable to traditional wood pulp, thus challenging the conventional belief that non-wood fibers limit runnability. The research emphasizes the superior printing

properties of reed-containing paper and the potential of non-wood materials in sustainable pulp production. The authors advocate for innovative processes, such as the Chempolis method, which facilitates efficient utilization of non-wood materials while addressing environmental concerns, thereby promoting sustainable development in the pulp and paper industry.

[18] review the potential of non-wood fibers, such as cotton stalk, cotton linters, and cotton rags, as sustainable alternatives in the paper industry, emphasizing their environmental and economic benefits. While primarily targeted at papermaking, these renewable fibers present promising applications for textiles, especially within circular economies focused on recycling fibers, including textile waste. The distinct properties of non-wood fibers, like the high silica content in straw, necessitate specific processing adaptations but contribute to the eco-friendly shift in both paper and textile industries.

Cellulose, derived primarily from wood fibers, is the most abundant renewable and biodegradable biopolymer on Earth. The structure of wood fibers spans multiple length scales—from the macroscopic fiber level down to the nanoscopic cellulose fibrils—resulting in a hierarchical organization that governs the mechanical and physical properties of cellulose-based materials. In recent years, microfibrillated cellulose (MFC) and nanofibrillated cellulose (NFC) have emerged as promising cellulosic nanomaterials with significant potential in the forest products and papermaking industries. Despite extensive research efforts and increasing industrial interest, further advances in processing, characterization, and property optimization are still required to fully exploit the potential of these nanocellulose materials [24, 25, 26]

1.3 Mechanical behavior of paper materials

Paper materials have a complex random microstructure characterized by compressed and interconnected fibers within a dense network. They are a notable example at the engineering scale of what has been recently called *network materials* [27]. This category includes all the materials that are inherently network-based systems and whose emergent physical properties are defined by the structure of the chemical bonds that connect their atoms or molecules, or other micromechanical links. Cellulose-based materials undergo deformation processes that span multiple scales, from nanometer-scale fiber interactions to the macro-scale performance of the entire sheet/component. As emphasized in [11], multi-scale modeling approaches capable of capturing the interactions at fiber, network, sheet, and laminate levels are a timely research topic.

At the micro-scale, accurately modeling individual cellulose fibers is crucial to understand the broader mechanical behavior of paper and paperboard. However, those fibers exhibit highly complex morphologies, making their characterization including the determination of fibers length, orientation, and thickness, both essential and challenging [28, 29, 30, 31]. While mechanical characterization at the fiber level remains difficult but feasible [32], organically-formed cellulose fibers introduce additional complexities due to irregularities along their length. Such irregularities contribute to variations in mechanical properties along the fiber, which must be carefully considered for reliable modeling [32, 33]. Furthermore, fiber-to-fiber bonds have been shown to play a vital role in determining both the strength and elongation properties of fiber networks [34]. Accurately simulating the cross-linking properties [35] and the inter-fiber bond strength [36, 37] is therefore important for predictive modeling. Above all, the statistical variability of cellulose fibers orientations and cross-linking are crucial also for technological applications where bonding of paper with other layers is a concern, such as in case of paper-aluminum packaging [38], or for paper-paper adhesion [39]. On the fiber network scale, characterizing the structure of fiber networks necessitates the development of network models, and μ-CT image reconstructions [40, 41, 42], structured networks [43, 44], or synthetic networks with random or statistical distributions [45, 8, 46, 47] offer a series of methods for digital twins.

At the macroscale, paper is often modeled as an anisotropic continuum material, allowing its complex mechanical behavior to be described within the framework of continuum mechanics. Various constitutive formulations have been developed to capture its nonlinear, anisotropic, and damage-dependent response, typically treating paper as an elasto-plastic material undergoing fracture [48, 49, 50, 51]. A recent comprehensive review by Sanjon et al. [1] examines current methodologies for characterizing the inhomogeneous structure and mechanical properties of paper and paperboard, emphasizing advanced non-contact techniques such as laser profilometry, X-ray microtomography, and THz spectroscopy for thickness and density measurements, as well as fiber segmentation and orientation analysis. The study further highlights the role of in-plane mechanical testing—tensile, compressive, and shear experiments—in elucidating anisotropic behavior, and discusses how these insights support the development of accurate continuum models that account for structural heterogeneity and guide process optimization.

To numerically simulate these continuum formulations, researchers have extensively applied the finite element method (FEM) to analyze the deformation and fracture of paper under various loading and environmental conditions [52, 53, 54, 55, 56, 35, 57]. FEM simulations have provided valuable insights into stress and strain distributions, anisotropic effects, and crack propagation mechanisms. However, directly modeling the fibrous network at the macroscale remains computationally demanding due to the inherent randomness and the large number of interacting fibers.

To mitigate these challenges, the concept of a Representative Volume Element (RVE) is commonly adopted to approximate the macroscopic response of the heterogeneous fiber network while maintaining computational efficiency. The appropriate RVE size must be sufficiently large to statistically capture the structural heterogeneity of the network, yet small enough to ensure numerical tractability—a subject investigated in detail in several studies [52, 58, 55]. Nevertheless, homogenization approaches based on RVEs lose validity once strain localization develops, particularly around the peak load and during the post-peak softening phase, where damage accumulation and crack growth dominate the material response.

1.4 Objectives

Despite decades of research, several limitations persist in the current understanding and modeling of paper mechanics. Many continuum models rely heavily on empirical fitting and simplified assumptions, without explicitly accounting for the underlying microstructural mechanisms that govern fiber recruitment, reorientation, and debonding. This lack of microstructural linkage limits their predictive capability, especially under complex loading conditions where the material response depends on the evolving fiber network configuration.

At the other end of the modeling spectrum, discrete fiber network simulations provide valuable insights into local deformation and failure mechanisms but are computationally prohibitive for large-scale or industrial applications. The high computational cost associated with representing thousands of interacting fibers and bonds restricts their use to small domains, preventing direct application to macroscopic engineering problems.

Another major challenge concerns the nonlinear anisotropic behavior of paper materials. Many existing models are unable to reproduce the anisotropic response of paper using a single set of constitutive parameters that remains valid for different fiber orientations. In addition, most of these models fail to accurately predict the material response under multiaxial loading conditions, which is crucial for realistic engineering applications. Furthermore, paper exhibits pronounced stochastic variability in its mechanical behavior, arising from natural heterogeneity and size effects. However, these sources of randomness as well as the representation of a realistic number of fibers within the network are seldom incorporated into current deterministic modeling frameworks.

Finally, as sustainability becomes an increasingly central concern, emerging reinforced paper materials that incorporate synthetic fibers highlight the need for new strategies to identify bio-based alternatives capable of maintaining comparable mechanical performance within the fiber network. Despite growing interest in such sustainable reinforcements, the integration of these aspects into mechanical modeling frameworks remains largely unexplored.

To address these gaps, this thesis aims to develop a multi-scale and nonlinear simulation framework for paper and paperboard materials that explicitly integrates microstructural stochasticity, nonlinear anisotropy, and constitutive evolution. The research first focuses on establishing a stochastic micromechanical model capable of describing fiber recruitment, bond failure, and fiber breakage under uniaxial loading conditions. Building on these insights, two nonlinear anisotropic continuum formulations based on a hypoelastic approach are developed, in which the constitutive parameters evolve with the mismatch between fiber orientation and the principal strain direction. The framework further establishes a quantitative linkage between continuum parameters and measurable microstructural features derived from the micromechanical model.

In addition, the proposed modeling strategy is extended to reinforced gummed paper networks, which are increasingly used in packaging applications, to evaluate their mechanical behavior and assess the potential of eco-friendly natural fibers as alternatives to synthetic reinforcements. The developed model is validated against experimental data, including mechanical testing, imaging, and fracture characterization, to ensure physical consistency and predictive robustness under tensile loading. Finally, some natural fibers are proposed as promising sustainable substitutes for synthetic fibers in reinforced gummed papers, aligning the study with the broader goal of environmentally responsible material development.

1.5 Outline of the thesis

The thesis is organized as follows:

Chapter 2 presents an integrated experimental and statistical mechanics analysis of paper fracture to elucidate how microstructural mechanisms govern macroscopic behavior. In-situ tensile tests combined with confocal microscopy are used to observe fiber activation, recruitment, and progressive failure in unnotched paper under uniaxial loading. A stochastic mechanics model is developed to describe the cellulose fiber network, decoupling morphological randomness from the intrinsic fiber constitutive law. The model successfully predicts the anisotropic response in the machine and cross-machine directions and is further employed to assess the effects of fiber orientation, strain redistribution, and fiber elasticity or elasto-plasticity on the overall mechanical behavior.

Chapter 3 introduces two nonlinear hypoelastic continuum models to simulate the macroscopic response of paper under biaxial plane-stress conditions. Based on the observation that fiber failure is governed by the direction of maximum principal strain relative to mean fiber orientation, the models incorporate an anisotropic damage variable dependent on these parameters. One model employs an orthotropic constitutive tensor, while the other uses a simplified isotropic formulation with an orientation-dependent elastic modulus. The framework also integrates the statistical micromechanics model at the material-point level and is validated against experimental data from tension tests on notched specimens.

Chapter 4 develops a statistical micromechanical model to analyze the uniaxial tensile response of reinforced paper materials, accounting for fiber orientation, free segment length, and failure mechanisms. After calibration using tests on pure cellulose paper, the model is extended to fiberglass-reinforced specimens and then applied to evaluate natural fibers such as hemp, kenaf, and flax as sustainable alternatives, supporting the development of eco-friendly paper-based reinforcements for packaging applications.

Chapter 5 presents an experimental study on the anisotropic fracture behavior of paperboard under uniaxial tension. Dog-bone specimens oriented at 0°, 30°, 45°, 60°, and 90° relative to the machine direction are tested to investigate how anisotropy influences crack initiation and propagation. The comparison of fracture angles and failure mechanisms across orientations provides valuable insights for validating the modeling approaches developed in earlier chapters.

Chapter 6 concludes the thesis by summarizing the main findings and emphasizing their relevance for multi-scale and nonlinear modeling of cellulose-based and reinforced paper materials. The chapter also outlines perspectives for future research on the design of sustainable, high-performance fiber-based materials and their broader application in environmentally responsible engineering solutions.

Chapter 2

A novel in-situ micro-mechanical testing of paper fracture and its stochastic network model [1]

The mechanical characteristics of paper materials as fiber networks are known to be influenced significantly by interactions between fibers and the properties of individual fibers. These attributes, including densities and distribution of fibers segment lengths and their geometrical properties, have been shown to undergo statistical changes within a fiber network [60, 61, 62]. Consequently, in this chapter, we are going to introduce a statistical mechanics theoretical model and its numerical implementation designed not only for efficient computational modelling of fiber networks at the macroscale, but also for accurate prediction of their fracture behavior at the microscale, without limitations on the number of fibers simulated. In parallel, in-situ testing is proposed by conducting tensile test experiments and observing the material evolution under loading, examining the microscopical phenomena involved during deformation up to fracture. Researchers have done some micromechanical tests for

[1] This chapter is based on our own publication Fallah, Zarei, and Paggi [59].

the characterization of fiber properties [32, 63, 64]. However, in the context of paper materials, results regarding in-situ testing are quite scarce. Therefore, we propose an experimental campaign by combining the micromechanical tensile stage and the confocal microscope with a setup which offers a versatile way to explore the microstructural mechanisms responsible for fracture.

2.1 Experimental methods: in-situ material testing setup

The equipment includes the micro-mechanical tensile stage DEBEN placed under the confocal microscope Leica DCM3D, see Fig. 1, both available in the MUSAM-Lab of the IMT School for Advanced Studies Lucca. This setup allows the in-situ visualization of the cellulose fibers and also the out-of-plane deformation of the specimen surface during the whole loading history [65], while the force-displacement curve is progressively recorded by the tensile stage.

The microstructure of the cellulose-based materials was further characterized through confocal microscopy imaging performed on different regions of the specimens. Each inspected area covered approximately $637 \times 477\ \mu m^2$, thus containing a sufficiently large number of fibers to provide a representative description of the fibrous network. An optical magnification of 20× was employed, allowing the individual cellulose fibers and the fiber-to-fiber bonding regions within the network to be clearly identified. These observations provide important insight into the heterogeneous microstructure governing the macroscopic mechanical response and fracture behavior of the material. Additional details regarding the micro-structural characterization procedure and image analysis are provided in Section 2.3.

A series of uniaxial tensile tests on unnotched rectangular paper specimens with dimensions $B \times L \times t$ (width, span and thickness) has been carried out. The specimens have been clamped at the extremes. The displacement loading rate has been set equal to 0.1 mm/min, which is sufficiently low to monitor all the micromechanical damage phenomena

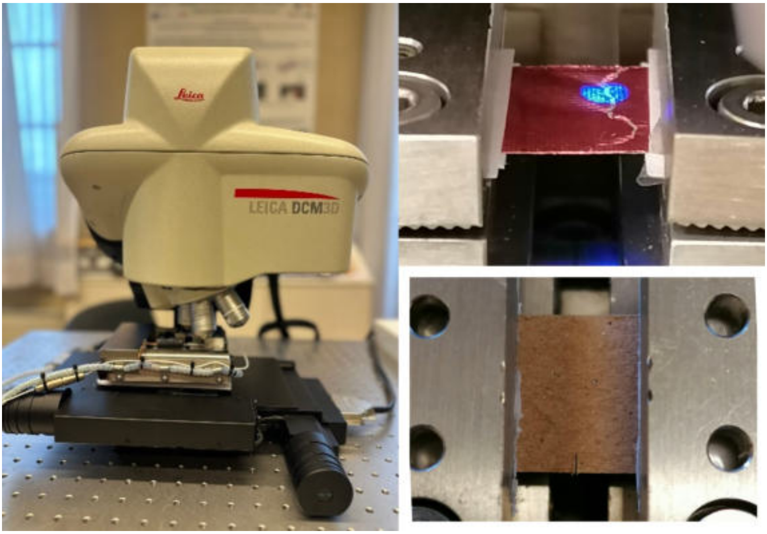

Figure 1: In-situ micro-mechanical tensile testing setup: DEBEN micro-mechanical tensile stage and the Leica DCM3D confocal microscope (left panel); photos of unnotched Al-paper laminate (right panel, top) and notched paper (right panel, bottom) specimens that can be tested in uniaxial tension.

with the confocal microscope and perform a single test in a reasonable amount of time. As exemplified in Fig. 2, single cellulose fibers that bridge a propagating crack can be clearly observed, as well as those debonded and broken.

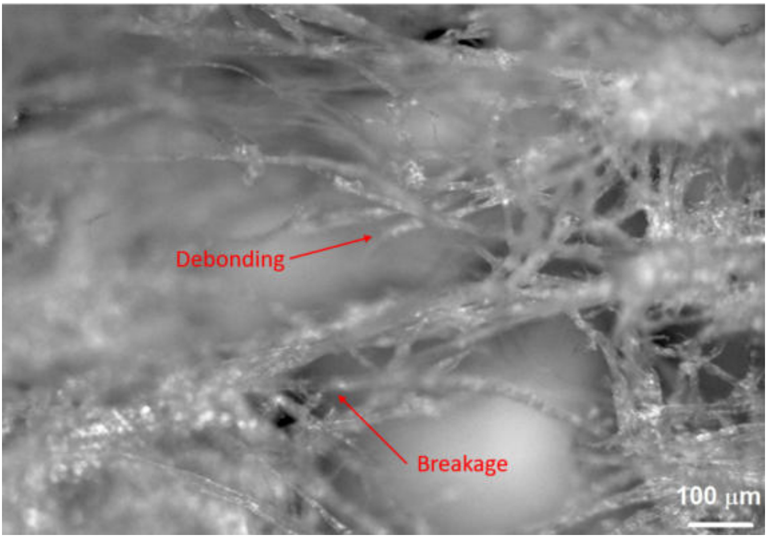

Figure 2: Microstructural alterations within a localised specimen region after reaching a defined load threshold during tensile testing, including fiber debonding and breakage, taken by confocal microscopy (20x magnification).

Furthermore, the employed tensile stage allows us to determine the overall mechanical behavior of paper -which is an emergent mechanical response- by measuring the force-displacement curve under displacement control which is of the type depicted in Fig. 3 (paper tested in the cross-machine CD direction). The response is initially linear and then it departs from linearity up to reaching a maximum load carrying capacity. After the peak load, a sharp softening branch takes place. This mechanical response, which can be converted into a conventional stress-strain diagram by dividing the force by the cross-section area and the displacement by the initial free span, has been recently interpreted through a phase field model for fracture driven by elastoplasticity with hardening [66].

However, the present authors consider this modelling assumption quite controversial, since the observed microscopical mechanisms do not always support a continuum model ruled by elastoplastic hardening. The mechanical system is in fact composed by a discrete set of cellulose fibers with strong adhesion between them caused by the pressure acted during production. When subject to tensile loading, fibers can partially move and align along the loading direction depending on the free length of each fiber intercurring between two subsequent fiber bonds. This leads to a phenomenon which is similar to *fiber recruitment* in biological tissues [67, 68, 69].

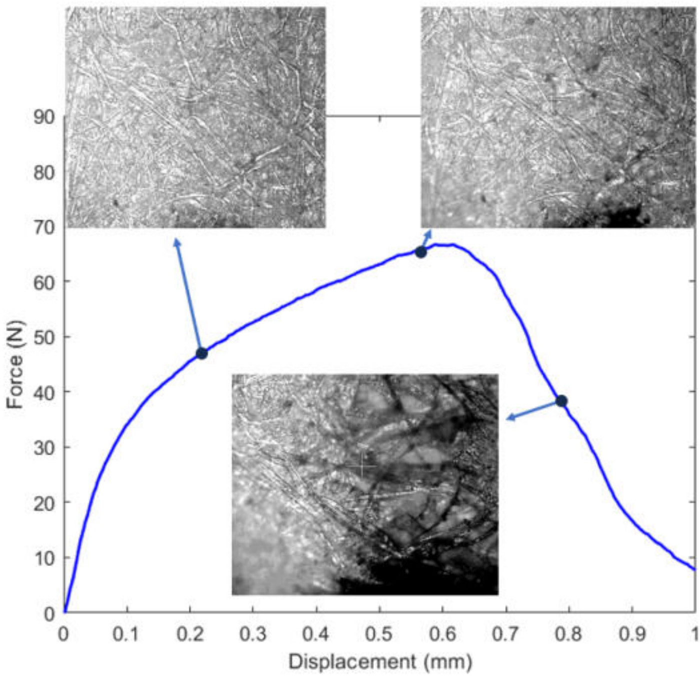

Figure 3: A typical mechanical response of a paper sample under tensile loading in the cross-machine direction (CD), with fiber recruitement followed by fiber debonding and slippage during crack growth. A video of the test is available as an electronic supplementary material.

It should be noted that fiber recruitment can occur at different loading levels depending on the fibers network and its density. In denser fiber networks, such as paper, we anticipate that fiber recruitment happens at low strains due to the restricted deformability of individual fibers. Conversely, in rarefied networks, like those obtained by electrospinning, fiber recruitment takes place at very large strains, see Fig. 4 where a representative fiber is colored in yellow to visualize its recruitment and realignment (tensile tests on PLLA electrospun layers using the DEBEN microtensile stage placed within the SEM Zeiss EVO MA15 at the MUSAM-Lab to achieve the required resolution).

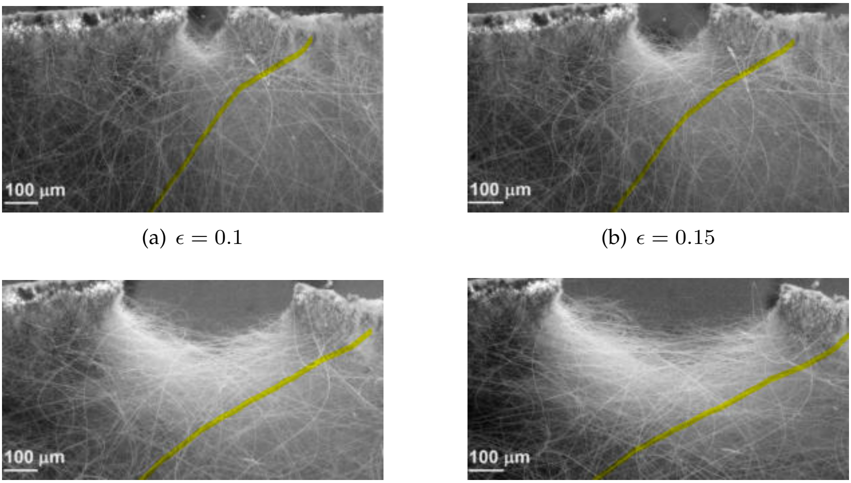

(a) $\epsilon = 0.1$ (b) $\epsilon = 0.15$

(c) $\epsilon = 0.2$ (d) $\epsilon = 0.25$

Figure 4: SEM images of PLLA electrospun layers at different strain levels, showing fiber recruitment and realignment along the axial (horizontal) direction of loading.

The fiber inclination is therefore relevant, since the fibers initially aligned along the loading direction mostly contribute to the load-carrying capacity. The fiber recruitment process continues until fiber slippage and bond failure is triggered. In some circumstances, fibers do not only slip with respect to each other, but also individually break, which is a catastrophic phenomenon leading to load redistribution to the remaining active fibers. These phenomena observed in our tests on paper are consistent with the microscopical mechanisms reported in the literature [70, 34]. Recent investigations [32] on single cellulose fibers tested under uniaxial test using an equipment similar to our setup showed that the slope of the stress-strain curves gradually decreases with increasing strain as a result of the development of inelastic deformations caused by micro-damage, up to the stage at which the fiber breaks. Furthermore, micro-plasticity was observed in [32] as a mechanism typical of polymer fibers, which inherently possess a distinct composition as compared to cellulose fibers that mostly behave linear elastically.

Hence, to elucidate on these fundamental modelling assumptions and derive a model that could predict the response as a direct consequence of quantifiable and observable microscopical mechanisms involving the network of fibers, a statistical mechanics model is put forward in the next section. As shown in [71, 72] for the problem of adhesion between paper tissues, the stochastic features of the fiber population play an essential role for a predictive model. Here, all the model parameters related to the random network topography will be estimated from data measurable from confocal images, leaving to be identified only few parameters describing the single fiber mechanical response, which is the key controversial aspect to be assessed.

2.2 Statistical mechanics model

In this section, we propose a model based on the network of cellulose fibers to simulate deformation and fracture of paper subject to uniaxial loading.

The starting point is a rectangular specimen of paper of $B \times L \times t$ dimensions, where B is its width, L its span, and t is its thickess. An orthogonal $x - y - z$ reference system is also introduced and an axial displacement w is applied along the $z-$direction (see the sketch in Fig. 5).

Under a macroscopically applied strain, $\epsilon = w/L$, resulting from the

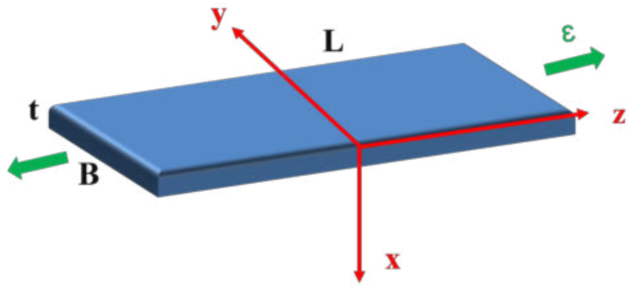

Figure 5: Schematic of the specimen and load orientation with respect to a global reference system.

imposed displacement w, fracture may occur at a randomly located single cross-section. Notably, the experimental tensile tests performed on both short-span and long-span specimens (referenced in [66]) demonstrate a variation in the force-displacement curves. These variations regard a simple linear scaling of the displacement with L, while forces do not change. This supports our model assumption that a cross-sectional model is adequate to describe the response of paper under uniaxial tension, where fracture occur at a single cross-section. Hence, under these assumptions, it is possible to focus the attention on the behavior of fibers crossing that representative cross-section. First, the average total number of fibers along such a cross-section can be quantified as:

$$N = N_l N_f \tag{2.1}$$

where N_l denotes the number of paper layers ($j = 1, \dots N_l$), each one with a thickness of a fiber, and N_f is the average number of fibers along the $y-$direction for each layer ($i = 1, \dots N_f$). Therefore, a fiber is univocally identified by the indices i and j.

At the microscale, fibers are assumed to have an average cross-section A, a random length $l_{i,j}$, and a random orientation angle $\alpha_{i,j}$ measured from the axial direction ($z-$axis). The centre of those fibers is placed at $x_{i,j} = jt/N_l$, $y_{i,j} = iB/N_f$, $z_{i,j} = 0$. The coordinates of the external nodes defining the beginning and the end of each fiber, see Fig. 6, are:

$$z_{i,j}^{(1)} = -l_{i,j}/2\cos(\alpha_{i,j}) \tag{2.2a}$$
$$y_{i,j}^{(1)} = y_{i,j} - l_{i,j}/2\sin(\alpha_{i,j}) \tag{2.2b}$$
$$x_{i,j}^{(1)} = x_{i,j} \tag{2.2c}$$
$$z_{i,j}^{(2)} = l_{i,j}/2\cos(\alpha_{i,j}) \tag{2.2d}$$
$$y_{i,j}^{(2)} = y_{i,j} + l_{i,j}/2\sin(\alpha_{i,j}) \tag{2.2e}$$
$$x_{i,j}^{(2)} = x_{i,j} \tag{2.2f}$$

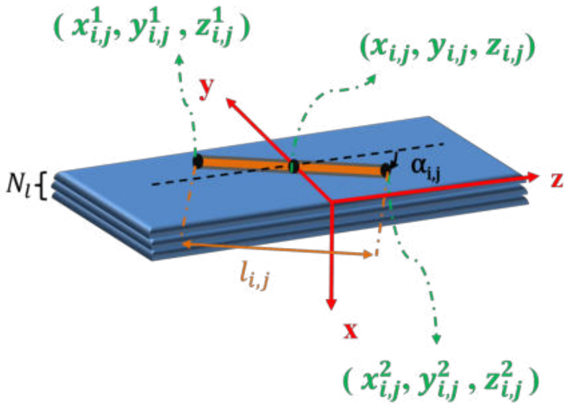

Figure 6: Orientation and coordinated of the extremes of the fibers along the critical cross-section at the microscale.

Fibre lengths are usually not constant, and therefore a Gaussian normal distribution is herein introduced to assign a random length $l_{i,j}$ to each fiber, specifying in input the mean (μ_l) and the root mean square (σ_l) values of the distribution. Moreover, cut-off lengths (l_0 and l_{max}) for the shortest and the longest fibres are also considered.

Fiber orientation is also a crucial parameter, since it is well-known that the macroscopic mechanical response of paper is anisotropic and it is particularly different in the machine direction (MD) and in the cross-machine direction (CD). Since this is primarily due to the different alignment of fibers caused by the machining process, we expect that the fiber orientation might strongly influence the overall mechanical response. In the present model, we explore three possible different distributions of fiber orientations along the cross-section line: (i) uniform distribution, (ii) non-uniform distribution with maximum probability in the machine direction, (iii) non-uniform distribution with maximum probability in the cross-machine direction. In the case of uniform distribution, the orientation angle $\alpha_{i,j}$ is assigned randomly with values ranging from 0 to $\pi/2$. For cases (ii) and (iii), on the other hand, Gaussian distributions with a mean value μ_α, a root mean square σ_α, and cut-off values $-\pi/2$ and $+\pi/2$ are considered. The mean value μ_α is set as:

$$\mu_\alpha = \begin{cases} 0, & \text{for the machine direction (MD)} \\ \pi/2, & \text{for the cross-machine direction (CD)} \end{cases} \tag{2.3}$$

It is worth mentioning that, considering the experimental findings from [73], which indicated fiber orientation distribution in the paper plane could resemble a normal distribution but with heavier tails, we adopt a Gaussian distribution with appropriate standard deviation and cut-off values, ensuring that the distribution does not approach zero probability for the tails. As a result, this model is capable of generating a population of fibers with different morphological characteristics, namely their lengths and orientations, representing the statistical features of paper materials.

Fibers often retain slack or curvature due to manufacturing and drying processes [74]. Mechanically, a loaded fiber begins to carry the load, when it overcomes this slackness and it gets straight, which leads to a phenomenon referred to as fiber recruitment in a fibrous network. To incorporate this phenomenon into our model, we assume that a cellulose fiber within a loaded paper material is recruited when the applied strain exceeds a specified activation strain. This activation strain serves as a threshold, indicating the point at which the external strain adequately overcomes the inherent curvature or slackness in the fibers, facilitating their effective involvement in the network's load-carrying mechanism. This activation strain can be reasonably related to the distance between two bonds along a given fiber, i.e., the distance between two subsequent points where a fiber is crossed by other fibers. We believe in fact that the average distance between subsequent bonds -which is a kind of *free segment length* [74], or a *mean free path* between two bonds, λ– is responsible for the stiffness of the fiber.

[74] discussed the probability distribution of free segment lengths and remarked it can be assumed to be exponential with its average value λ_{avg}. Experimentally, the average mean free path can be estimated from confocal miscroscopy images by dividing a fiber length by the number of bonds observed along its length, and averaging over a statistically representative number of fibers. Hence, we can associate to each individual fiber a randomly assigned mean free path, $\lambda_{i,j}$, extracted from an exponential distribution in the range from $\lambda_{\min}$ to $\lambda_{\max}$, where $\lambda_{\max}$ and $\lambda_{\min}$ signify the maximum an minimum distance between two adjacent bonds within the network respectively, the attributes that can be effectively observed from microscopy images.

It should be noted that the adopted fiber arrangement represents an idealized configuration in which the fibers are centered at $z_{i,j} = 0$ and equally spaced along the transverse direction, see Eqs. (2.2). These assumptions simplify the geometrical description of the fibrous network and facilitate the interpretation of the underlying micromechanical mechanisms. Nevertheless, the model incorporates an exponential distribution for the interfiber bond lengths, which implicitly introduces nonuniform bonding and local heterogeneities within the network. Therefore, although the geometrical arrangement is simplified, the stochastic nature of the interfiber interactions and the resulting variability of the mechanical response are still accounted for in the proposed formulation.

In the strain-controlled constitutive fiber model, the activation of fibers is determined based on their respective mean free paths. It is anticipated that fibers with shorter mean free paths will be activated earlier due to their relatively higher stiffness (less slackness). On the other hand, longer fibers, which may not be fully straight, do require more deformation to be engaged in the overall deformation process. Additionally, the model takes into account the connectivity of fibers, where multi-connected fibers are expected to be activated earlier than isolated ones.

To quantify the activation strain for each fiber, the following formulation is introduced:

$$\epsilon^{a}_{i,j} = \epsilon^{\text{act}} \left(\frac{\lambda_{i,j} - \lambda_{\min}}{\lambda_{\max} - \lambda_{\min}} \right) \tag{2.4}$$

where ϵ^{act} represents the maximum strain required for a fiber activation, equivalent to the strain necessary to activate a fiber possessing the maximum free path, $\lambda_{\max}$.

As cited in the literature [75], since the measured force required to break the inter-fiber bond is considerably lower than the force needed for the fiber to undergo nonlinear deformation, the fiber is assumed to respond elastically after recruitment. In the uni-axial tensile test on plain specimens, with all the fibers not slipping (either not yet recruited, or recruited), the strain level ϵ is assumed to be dictated by the imposed far field displacement at the boundary, i.e., $\epsilon = w/L$. This uniform condition is then perturbed when fiber slippage takes place, and the amount of strain redistribution will be discussed later. Hence, in the linear regime, the strain applied to each fiber along its axial direction is computed from the applied strain ϵ acting on the $z-$direction:

$$\epsilon_{i,j} = \epsilon \cos(\alpha_{i,j}) \tag{2.5}$$

Correspondingly, the elastic force supported by the fiber is:

$$f_{i,j} = K\epsilon_{i,j} \tag{2.6}$$

where K is the fiber stiffness. The fiber contribution to the uni-axial load is retrieved by projecting $f_{i,j}$ back to the axial direction:

$$F_{i,j} = K\epsilon \cos^2(\alpha_{i,j}) \tag{2.7}$$

We remark here that the model can be enhanced by an elasto-plastic constitutive relation instead of a linear elastic one, simply by modifying the constitutive relation in Eq. (2.6). In addition, the cross-section of the fibers (A) along with Young's modulus of a single cellulose fiber, E, contribute to the calculation of the fibers' stiffness $K = EA$.

In this study, similar to the Cox model [76], we incorporated the orientation of fibers to facilitate load transfer among them. While the Cox model is traditionally applied to analyze fibrous materials within a resin matrix, our adaptation extends its principles to fibrous materials without a matrix. However, for such materials, the influence of bond density becomes crucial. Hence, we accounted for this factor in our model by considering the mean free length of fibres, recognizing its significance in determining the strength of these materials. It should be noted that the present model is specifically developed for uniaxial tensile loading of plain specimens and can be regarded as a reduced-order stochastic model. Within this framework, non-affine deformation mechanisms, such as local fiber rotations, sliding, or bond compliance effects, are not explicitly resolved. The primary objective of the model is instead to reproduce the global tensile response of the material through a computationally efficient formulation. Moreover, the model parameters are identified through experimental calibration, which partially compensates for the simplified kinematic assumptions adopted in the constitutive description and mitigates the tendency of affine formulations to overestimate the elastic stiffness of the network.

The fiber linear response is limited in the model by the strain level, when a maximum strain $\epsilon_{i,j}^{\max}$ is reached. After that level, the fiber debonds and its contribution to the overall load is assumed to be negligible. Notably, if the maximum debonding strain for each fiber, $\epsilon_{i,j}^{\max}$, exceeds the fiber's breakage strain, ϵ^{f}, then the fiber breaks before experiencing debonding. In the model, the debonding strain for each fiber is assumed to be a random field dependent upon the mean free path of the fiber, i.e.:

$$\epsilon_{i,j}^{\max} = \epsilon^{\max} \left(\frac{\lambda_{\mathrm{avg}}}{\lambda_{i,j}} \right) \tag{2.8}$$

which implies that $\epsilon^{\max}$ can be estimated from the micromechanical test of bond failure with just two fibers bonded together, as for instance in [37].

In our simulation, when a fiber undergoes failure, we adopt a strain redistribution to neighboring fibers -a strategy consistent with the principles of fiber bundle models outlined in the literature, see e.g. [77, 78].

These models, acknowledged for their simplicity and effectiveness in understanding failure phenomena, detail the successive failure of fibers and subsequent adjustments in load distribution among the surviving fibers. In our model, resembling these fiber bundle models, redistributing strain is functionally equivalent to redistributing load, as all fibers are assumed to have the same elastic properties. The amount of redistribution is governed in the model by a parameter r ranging from 0 to 1. If the i^{th} fiber fails, its strain at failure will be equally redistributed to the $(i-1)^{th}$ and $(i+1)^{th}$ fibers as follows:

$$\epsilon_{i-1,j} \leftarrow \epsilon_{i-1,j} + r/2\epsilon_{i,j} \tag{2.9a}$$

$$\epsilon_{i+1,j} \leftarrow \epsilon_{i+1,j} + r/2\epsilon_{i,j} \tag{2.9b}$$

The mechanisms of fiber realignment has been found particularly relevant for the Poisson effect for the papers examined, in the range of densities. As a general trend, the lower the density, the more accurate is this assumption. As a limit case, fibrous materials obtained by electrospinning are for instance the fibrous materials where the progressive relative displacement and realignment of the fibers along the loading direction is giving the maximum contribution to the Poisson effect. By increasing the paper density, other forms of deformation of the fibers' joints may increase their role. In this study, to account also for the progressive alignment of the fibers along the direction of loading, which can lead to the macroscopic Poisson restriction effect, the z coordinates of the fiber nodes, the fiber angle and its stretched length are updated based on the deformation level (deformed configuration):

$$z^{(1)}_{i,j} \leftarrow z_{i,j} - l_{i,j}\cos(\alpha_{i,j})\epsilon_{i,j}/2 \tag{2.10a}$$

$$z^{(2)}_{i,j} \leftarrow z_{i,j} + l_{i,j}\cos(\alpha_{i,j})\epsilon_{i,j}/2 \tag{2.10b}$$

$$\alpha_{i,j} \leftarrow \arctan\left(\frac{y^{(2)}_{i,j} - y^{(1)}_{i,j}}{z^{(2)}_{i,j} - z^{(1)}_{i,j}}\right) \tag{2.10c}$$

$$l(i,j) \leftarrow \sqrt{\left(z^{(2)}_{i,j} - z^{(1)}_{i,j}\right)^2 + \left(y^{(2)}_{i,j} - y^{(1)}_{i,j}\right)^2} \tag{2.10d}$$

Consequently, we can assess the amount of realignment of fibers by calculating the norm of the difference between the fibers' orientation during the simulation with respect to the original (undeformed) one, i.e., α_0 before loading and α after loading as computed by Eq.(2.10), normalizing it by the total number of fibers. To quantify this effect and comparing it with the density of the networks, we anticipate that this measure of realignment in the MD direction for the materials with lower and higher densities, is equal to 1.01×10^{-4} (radians) for material 1 (the less dense paper), and 9.9×10^{-5} (radians) for material 3 (the more dense paper). These results confirm that realignment is a small quantity for paper materials, and is a decreasing function of paper density.

By summing all the forces $F_{i,j}$ acting on the active fibers during each loading step, the force-displacement curve of the sample can be finally predicted.

2.3 Algorithmic aspects and model parameters' identification

The algorithmic aspects of the proposed model implemented in MATLAB R2022 are presented in Alg. 1. Note that $\texttt{Label}_{i,j}$ stands for the status of each fiber during loading steps and can assume four different values: 0, for a not yet recruited fiber; 1 for a recruited fiber; 2 for a debonded fiber; and 3 for a broken fiber. Therefore, the total number of activated, debonded and failed fibers can be estimated by summing the fibers of each class identified by the corresponding labels.

Algorithm 1: Algorithm of the statistical mechanics model

Number of random realizations, N_g
Inputs for geometry and BCs: L, B, t, N_m, $w_{\max}$, isotropic/MD/CD
Inputs of the fibers' geometry: N_f, N_l, l_0, $l_{\max}$, d, μ_l, σ_l, μ_α, σ_α, $\lambda_{\min}$, λ_{avg}
Inputs of the fibers' mechanical properties: K, ϵ^{act}, $\epsilon^{\max}$, ϵ^{f}, r

for $s = 1, \ldots, N_g$ **do** ▷ Loop over random realizations

Construct the network:
Random generation of fibers' length, orientation, number of bonds
Position of fibers' coordinates $x_{i,j}^{(1)}, y_{i,j}^{(1)}, z_{i,j}^{(1)}, x_{i,j}^{(2)}, y_{i,j}^{(2)}, z_{i,j}^{(2)}$
Compute $\epsilon_{i,j}^{a}$ and $\epsilon_{i,j}^{f}$, Eqs.(2.4) and (2.8)
Set $F = 0$, $\epsilon_{i,j} = 0$, $\mathrm{d}\epsilon_{i,j} = 0$, $\mathtt{Label}_{i,j} = 0$, $w = w_{\max}/N_m$
for $m = 1, \ldots, N_m$ **do**
  for $j = 1, \ldots, N_l$ **do**
    for $i = 1, \ldots, N_f$ **do**
      $\epsilon_{i,j} \leftarrow \epsilon + \mathrm{d}\epsilon_{i,j}$
      if $\epsilon_{i,j} < \epsilon_{i,j}^{a}$ **then**
        $f_{i,j} \leftarrow 0$ ▷ Fiber not recruited
      end if
      if $\epsilon_{i,j} \geq \epsilon_{i,j}^{a}$ and $\epsilon_{i,j} <\min(\epsilon_{i,j}^{max}, \epsilon_{i,j}^{\mathrm{f}})$ **then**
        $\mathtt{Label}_{i,j} \leftarrow 1$ ▷ Active fiber
        Compute $f_{i,j}$, Eq.(2.6)
        Finite elasticity update, Eqs.(2.10)
      end if
      if $\epsilon_{i,j} \geq\min(\epsilon_{i,j}^{\max}, \epsilon_{i,j}^{\mathrm{f}})$ **then**
        if $\min(\epsilon_{i,j}^{\max}, \epsilon_{i,j}^{\mathrm{f}}) = \epsilon_{i,j}^{\max}$ **then**
          $\mathtt{Label}_{i,j} \leftarrow 2$ ▷ Debonded fiber
        end if
        if $\min(\epsilon_{i,j}^{\max}, \epsilon_{i,j}^{\mathrm{f}}) = \epsilon_{i,j}^{\mathrm{f}}$ **then**
          $\mathtt{Label}_{i,j} \leftarrow 3$ ▷ Broken fiber
        end if
        $f_{i,j} \leftarrow 0$
        $\mathrm{d}\epsilon_{i,j-1} \leftarrow \mathrm{d}\epsilon_{i,j-1} + r/2\epsilon_{i,j}^{f}$
        $\mathrm{d}\epsilon_{i,j+1} \leftarrow \mathrm{d}\epsilon_{i,j+1} + r/2\epsilon_{i,j}^{f}$
      end if
      $F \leftarrow F + f_{i,j}$
    end for
  end for
  $\epsilon \leftarrow mw/L$
end for
end for

Output: Stress-strain diagram, number of not recruited and recruited fibers, number of bonding and breakage failures.

The following input data are required: (i) inputs concerning the geometry and the boundary conditions, (ii) inputs related to the fiber geometry, and (iii) inputs for the fiber mechanical properties. Concerning the first set of inputs, in this study we used three paper samples with different density. For these samples, we specified $B = 12.5$ mm, $L = 10.0$ mm and their respective thickness values are provided in Tab. 1.

Material	Paper density, ρ (kg/m^3)	Thickness, t (mm)	Maximum imposed strain, $w_{\max}/L$
1	697.0	0.2	0.085
2	737.7	0.1	0.050
3	1230.0	0.2	0.100

Table 1: Paper samples properties and their boundary conditions.

For the paper configuration, the uni-axial tensile test was conducted in the both machine and cross-machine directions of the tested specimens, and the maximum imposed strain for each sample was $w_{\max}/L$, see Tab. 1. Hence, a uniform strain $\epsilon = w/L$ has been applied in the proposed model in $N_m = 100$ loading steps with a linear ramp.
At the microscale, the use of the confocal microscope Leica DCM3D allows to visualize fibers and determine the required geometrical parameters of the model, such as N_f, N_l, $\lambda_{\min}$, λ_{avg}.
Figure 7 shows an image of a paper specimen with $\rho = 1230$ (kg/m^3) captured using the confocal microscope with a $20\times$ magnification, which is 637×477 μm^2 size and contains a large number of fibers.
Thereby the number of fibers crossing an exemplary cross-section, e.g. the red line 477μm long in Fig. 7, is counted to be 28, which gives a density of fibers $28/477 = 0.00587$ fibers/μm and therefore a total number $N_f = 0.00587 \times B = 716$ of fibers in one layer for this sample.
In order to determine the number of layers within the paper specimen, N_l, we employed a methodology that relied on the assumption that N_l corre-

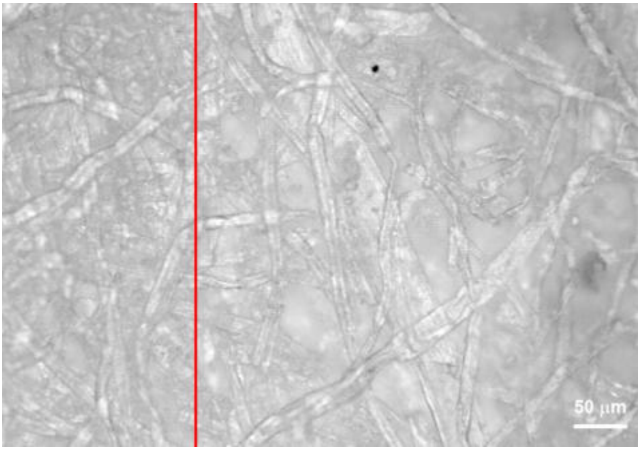

Figure 7: Confocal microscope image of a paper sample with $\rho = 1230$ (kg/m^3) at $20\times$ magnification, showing a random arrangement of cellulose fibers. The red line shows an exemplary cross-section.

sponds to the count of fibers with large widths capable of fitting through the thickness of the specimen. To establish the average of maximum fiber width, $w_{\max}$, present in the sample, we employed a rigorous methodology that combined microscopy and image-processing techniques. The analysis involved the random selection of multiple snippets from the specimen, ensuring the inclusion of fibers with maximum widths. These snippets were carefully examined using a microscope and high-resolution images were captured. Leveraging the capabilities of the ImageJ software, we accurately measured the widths of the largest fibers in the selected snippets, accounting for the image scaling. To ensure statistical significance, measurements were taken for the largest fibers within each snippet. By averaging these measurements, we determined the average value for maximum fiber width to be 36.3 μm, for the samples of material 3, and consequently, 6 layers of fibers are packed through this sample thickness. Subsequently, the number of layers, N_l, and cross-sectional fibers, N_f, for two additional samples were derived; see Tab. 2, by scaling their corresponding thickness and density with the thickness and density of sample 3, respectively.

The parameters related to the free segment length, which are $\lambda_{\min}$, and λ_{avg} were determined experimentally: the ImageJ software was employed to calculate and compare the free distance between two bonds in each snippet, leading to the derivation of its minimum and the average values given in Tab. 2. It should be noted that determining these free segment lengths using a 2D image from confocal microscopy requires careful inspection of possible bonds. In this context, fibers that are crossing each other and observable on the surface are considered sufficiently pressed and therefore bonded when they belong to the same focal plane. For instance, in area A of Fig. 8, fibers are in the same focal plane and can be considered in contact and bonded. Conversely, in the area B, fibers appear more blurry, belong to different focal planes, and are not sufficiently pressed to be bonded.

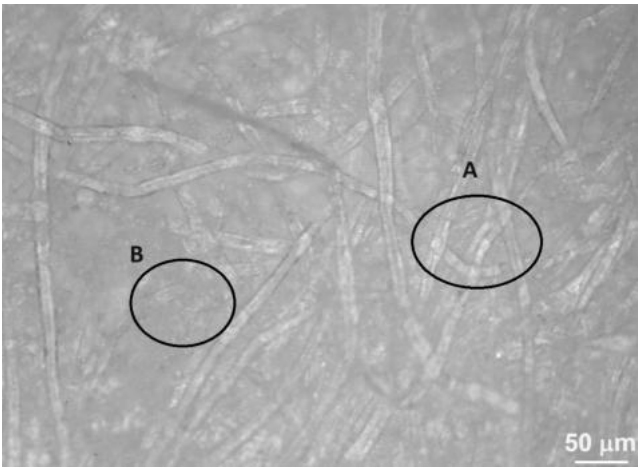

Figure 8: Confocal microscope image of a paper sample with $\rho = 1230$ (kg/m^3) at 20× magnification. Fibers in area "A" are considered bonded compared to the area "B", where fibers are blurry and belong to different focal planes.

Material	N_l	N_f	λ_{min} (μm)	λ_{avg} (μm)
1	6	406	7	48
2	3	859	6	45
3	6	716	6	37

Table 2: Fibers' geometry parameters derived from confocal microscopy.

The other morphological parameters used for the proposed model are collected in Tab. 3, which were taken from the literature (the parameters related to the fibers' length and cross-section area are based on [34], the orientation parameter is based on [79]).

$\mu_l \pm \sigma_l$ (mm)	l_0 (mm)	l_{max} (mm)	A (μm^2)	σ_α
2.5±0.5	0.25	5	230	$\pi/2$

Table 3: Fibers' geometry parameters taken from the literature.

The last set of input data relates to the mechanical properties of fibers, a crucial and debatable aspect that requires a careful examination. The mechanical properties of cellulose fibers, such as Young modulus (E) and breakage strain of fibers (ϵ^{f}), exhibit variability in a network as reported in the literature [32] based on single fiber tests. [34]'s experimental and micro-mechanical simulations emphasize the crucial role of fiber bonding in determining both the strength and elongation of fiber networks. To determine appropriate values for the mechanical parameters in our model, given the potential changes in these parameters during the paper-making process, we minimized the error between simulated and experimental stress-strain curves (Fig. 9) for each material, introducing a force redistribution factor (r) equal to 0.005 for all the cases (see the section on parametric analysis). The results of three replica for each material showed a very good repeatability of the experimental results, as illustrated in Fig. 9. The identified mechanical parameters for each material and sample are collected in Tab. 4. The identified Young modulus of fibers (E_f) resulted in values consistent with the range reported in recent experimental studies [32]. The maximum strain for fiber activation (ϵ^{act}) was identified to align with the nonlinear part of the experimental curve in the initial linear

regime and has been set to 0.002 for all the materials. The maximum strain for debonding, ϵ^{max}, and the fiber breakage strain, ϵ^{f}, were determined by matching the second part of the experimental curves, where the steepness changes until reaching the peak.
Results shown in Tab. 4 highlight that fiber stiffness is independent of the specimen tested, while it depends upon the material density. Parameters related to the failure strain, ϵ^{max} and ϵ^{f}, are dependent not only on the specimen tested, but also on the material density. On the other hand, variations in papermaking conditions, such as drying process, can impact the mechanical properties of paper materials. Notably, the mechanical properties of fibers in the machine direction (MD) and cross-machine direction (CD) may differ due to distinct drying conditions in those directions. Research presented by [80] indicates that reducing shrinkage or applying stretch significantly decreases the strain at break, potentially explaining the lower values of ϵ^{f} in the MD direction as compared to those in the CD direction. The variability in the debonding strain, ϵ^{max} could be subject to changes during the papermaking process as well.
A simple guideline on how to identify the mechanical model parameters from an experimental uniaxial stress-strain curve is provided in Fig. 10. The activation strain ϵ^{act} has a specific role on the recruitment of fibers and on the nonlinear response for very small strains. Then, the fiber stiffness K influences the slope of the linear regime. The parameter ϵ^{max} is modulating the transition from linear elastic to ipoelastic regimes, and finally ϵ^{f} is the strain at the peak of the diagram, at the onset of catastrophic failure.
The model provides further insight into the effect of paper anisotropy due to fiber orientation resulting from the machining process, which leads to distinct characteristics along the machine direction (MD) and the cross-machine direction (CD). The total number of fibers in a cross-section of the network model comprises the sum of not-activated fibers, activated fibers, and failed fibers (including both broken and debonded fibers). We remark that the sum of the percentages of fibers in different states (active, not-active, debonded and broken in Figs. 11), for each material in a given configuration (MD or CD), always amount to 100% at any strain level,

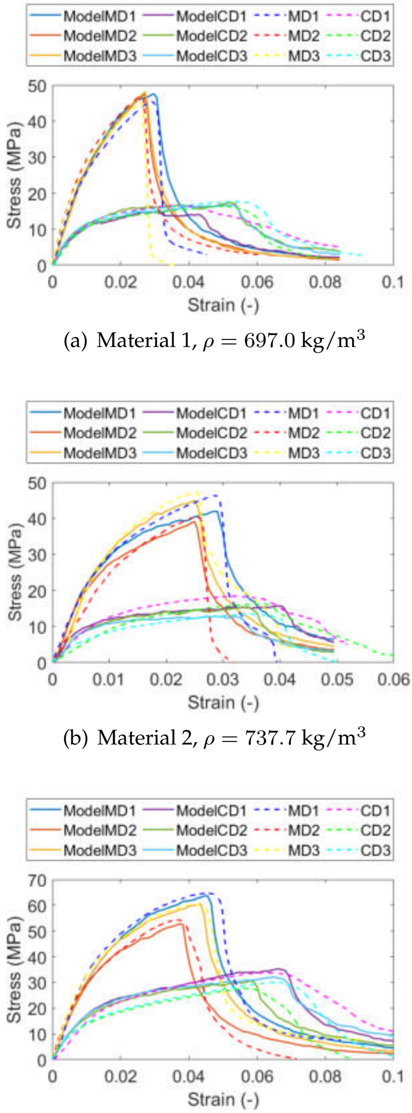

(a) Material 1, $\rho = 697.0$ kg/m^3

(b) Material 2, $\rho = 737.7$ kg/m^3

(c) Material 3, $\rho = 1230.0$ kg/m^3

Figure 9: Simulated (solid lines) and experimental (dashed lines) stress-strain curves of the paper materials with different densities. Each material had three repetitions of the test.

Material	Sample	E_f (GPa)	$\epsilon^{\max}$ (MD)	ϵ^{f} (MD)	$\epsilon^{\max}$ (CD)	ϵ^{f} (CD)
1	1	31	0.022	0.031	0.0080	0.045
1	2	31	0.024	0.028	0.0080	0.058
1	3	31	0.023	0.028	0.0080	0.061
2	1	22	0.012	0.030	0.0055	0.037
2	2	22	0.010	0.026	0.0048	0.037
2	3	22	0.013	0.026	0.0045	0.037
3	1	21	0.020	0.047	0.0135	0.070
3	2	21	0.017	0.039	0.0130	0.060
3	3	21	0.019	0.045	0.0130	0.070

Table 4: Identified properties of the model for the simulation results shown in Fig. 9.

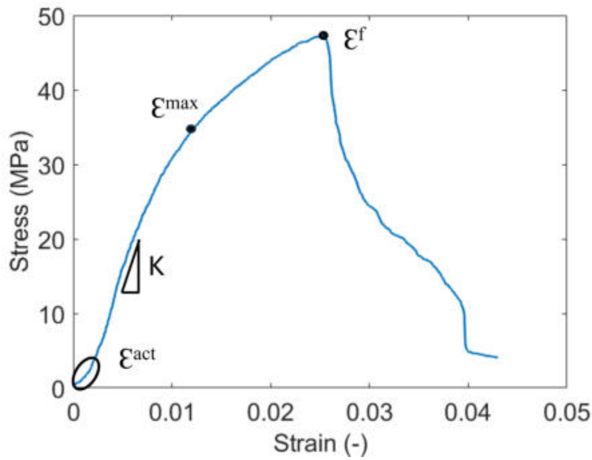

Figure 10: Guideline for the identification of model parameters based on experimental the stress-strain curves.

which is the total number of fibers of the cross-section.
Simulation results, depicted in Figs. 11(a), 11(c) and 11(e), compare the percentage of fibers that become active during the test in the MD and CD cases for material 1, 2, and 3 respectively. In the MD configuration, around 70% of fibers were recruited and activated during the loading process, for all the materials with different paper densities. This can be explained by the fact that loading the specimen along the machine direction, which has the majority of fibers oriented in the same direction, accelerates reaching the activation strain required to contribute to load transfer. In contrast, for the CD configuration, lower percentages of fibers between 40% and 50 % are recruited, since most of the fibers are not aligned along the direction of loading. Moreover, in the case of material 3, the difference between the percentages of active fibers for the MD and CD directions is smaller than in the other materials, indicating a lower degree of anisotropy for it.
Furthermore, the model offers predictive insights into the evolution of the percentage of failed fibers during loading, considering both debonding and breakage. As depicted in Figs. 11(b), 11(d), and 11(f), the total number of failed fibers, encompassing both debonded and broken fibers, is higher in the MD direction across all samples. Significantly, the simulations show that paper fracture predominantly occurs due to debonding in both the MD and CD configurations, with the count of broken fibers in the CD being much lower than in the MD. This correlates with [81] findings, indicating internal delamination as the primary failure mode in CD-tested samples, further supporting our observation of fewer broken fibers in the CD as compared to the MD.
Figure 12 illustrates the probability distribution of the mean free length, λ, and of the fiber failure strain, ϵ^f, in the CD direction for the three materials herein analyzed. Material 3, characterized by the highest density, has a λ distribution exhibiting a lower average value, indicating denser regions near λ_{min}. This implies that denser papers have a higher probability of having λ close to zero and a lower probability of having large λ, resulting in reduced porosity and enhanced strength, consistent with the maximum tensile stress and maximum elongation at the peak point in Fig. 9. The distribution of ϵ^f is influenced not only by the λ distribution but also

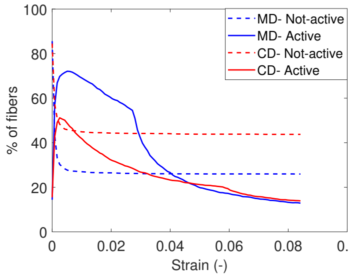

(a) Percentage of active and not-active fibers - material 1

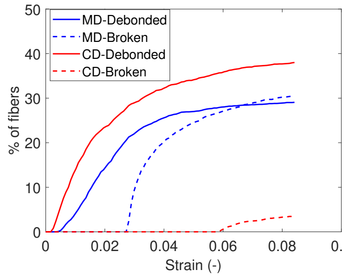

(b) Percentage of failed fibers - material 1

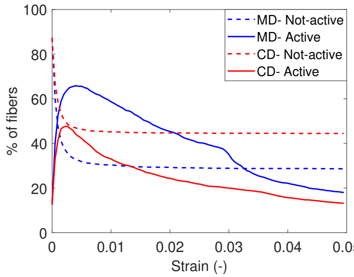

(c) Percentage of active and not-active fibers - material 2

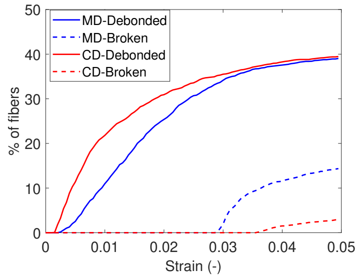

(d) Percentage of failed fibers - material 2

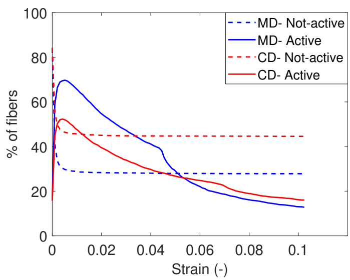

(e) Percentage of active and not-active fibers - material 3

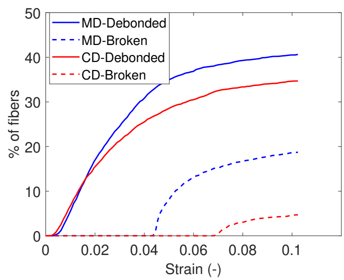

(f) Percentage of failed fibers - material 3

Figure 11: a, c, and e: Percentage of active fibers during a uniaxial tensile test of paper materials 1, 2, and 3 respectively. b, d, and f: Percentage of failed fibers (debonded and broken) during loading for materials 1, 2, and 3, respectively, for both the MD and CD directions.

by the papermaking process. Surprisingly, materials 1 and 2, with similar densities, show distinct ϵ^f distributions, possibly attributed to layer effects. Conversely, materials 1 and 3, despite having significantly different densities, exhibit similar ϵ^f distributions, likely due to their equal thicknesses.

A crucial question arises concerning the observed changes in the slope of the stress-strain curve in our model, given that we have considered a linear constitutive relation for fibers, encompassing their elastic behavior. To address this, we present the stress-strain curves of material 1 alongside the percentage of failed fibers (the sum of debonded and broken fibers shown in Fig. 11(b)) vs. strain in Fig. 13. This figure clarifies that the alteration in the slope of the stress-strain curve in both MD and CD directions is attributed to the increasing number of failed fibers beyond certain strains. In the CD configuration, fibers begin debonding from a strain of approximately 0.01 until the peak point. Subsequently, the slope of failed fibers increases, signifying a significant decrease in the number of fibers capable of bearing the load and, consequently, leading to the observed post-peak behavior in the stress-strain curve. Interestingly, in the MD direction, the number of failed fibers is initially lower than in the CD configuration until the peak load. However, it significantly increases afterward, surpassing the CD's count, resulting in a sharp decline in the MD stress-strain curve. This is due to the parameter ϵ_f which differs between MD and CD directions because of variations in papermaking conditions. These variations result in fibers being more brittle in the MD, leading to have significantly higher percentage of broken fibers in the MD compared to the CD.

An additional test under cyclic loading conditions with variable strain amplitudes has been conducted to confirm some key assumptions of the proposed model. The analysis of the cyclic stress-strain curves provide the amount of *recovered strain* during unloading, see the sketch in Fig. 14 for its computation.

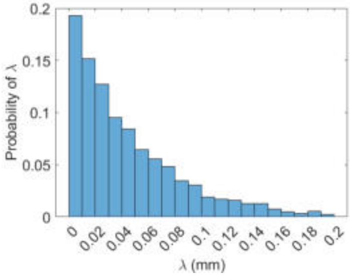

(a) Material 1

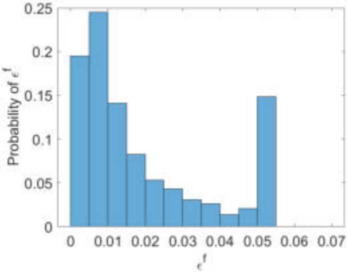

(b) Material 1

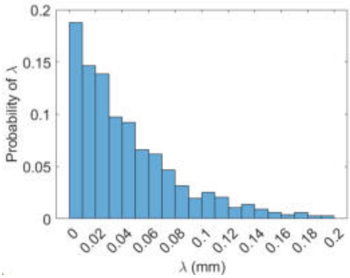

(c) Material 2

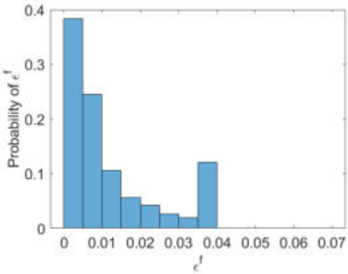

(d) Material 2

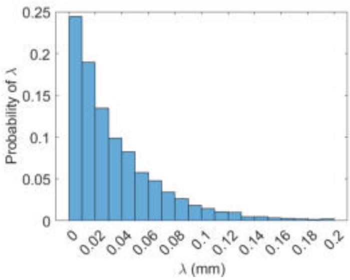

(e) Material 3

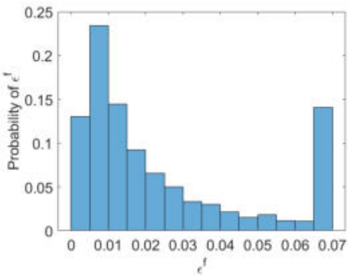

(f) Material 3

Figure 12: a, c, e : Probability distribution of mean free length in materials 1, 2, and 3 respectively. b, d, f : Distribution of failure strain of fibers in the cross-machine direction in materials 1, 2, and 3 respectively.

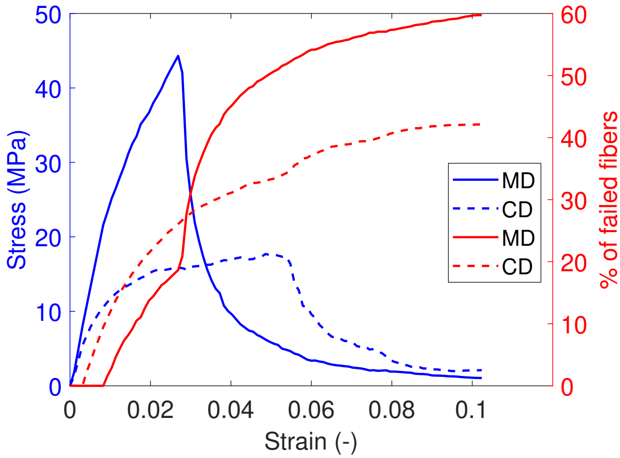

Figure 13: Experimental stress-strain curve of material 1, blue curves, accompanied by the corresponding failed fibers percentage relative to strain, red ones, in the both MD and CD directions.

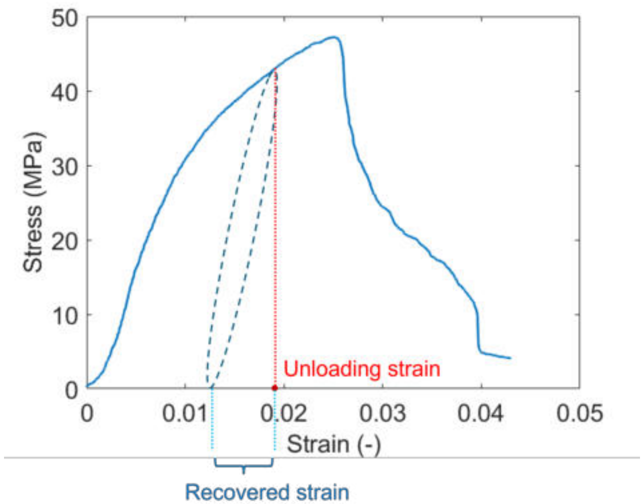

Figure 14: Measurement of the recovered strain from cyclic loading tests.

Specifically, material 3 was tested both in the MD and CD directions by applying uniaxial tensile loading to the samples until reaching predetermined strains, incrementally increased by steps of about 20% from zero to the strain at the peak load. Subsequently, the samples underwent unloading to zero load, followed by reloading. The results of these tests are shown in Fig. 15(a). Based on the proposed model, at unloading we expect to have an amount of recovered strain associated to the active fibers that at the unloading strain had a linear elastical behaviour. On the other hand, the amount of irreversible strain not recovered during unloading is caused by those fibers that achieved debonding failure. Therefore, the *expected recovered strain* provided by the model should be equal to:

$$\epsilon_r = \epsilon_{\text{un}} \left(\frac{N_a}{N_t} \right) \tag{2.11}$$

where ϵ_{un} is the strain at the point of unloading, N_a is the number of linear elastic active fibers at that point, and N_t is the total number of fibers. The comparison between the expected (model predicted) recovered strains and the experimentally observed recovered strains at different levels of unloading strain is shown in Fig. 15(b). Remarkably, the results demonstrate that the two set of data are closely aligned on the $45°$ line shown in black, which implies that the model is accurately predicting the amount of recovered strain measured in the experiments and, as a consequence, it confirms the ability of the model to correctly predict the evolution of active fibers with loading and the underlying model assumptions.

2.4 Sensitivity analysis

To further assess the robustness of the developed statistical mechanics model and further understand the effect of each model parameter, a sensitivity analysis is herein put forward. It's important to note that the parameters employed in this analysis are specifically related to material 1, ensuring a focused examination of its sensitivity to variations in these key factors.

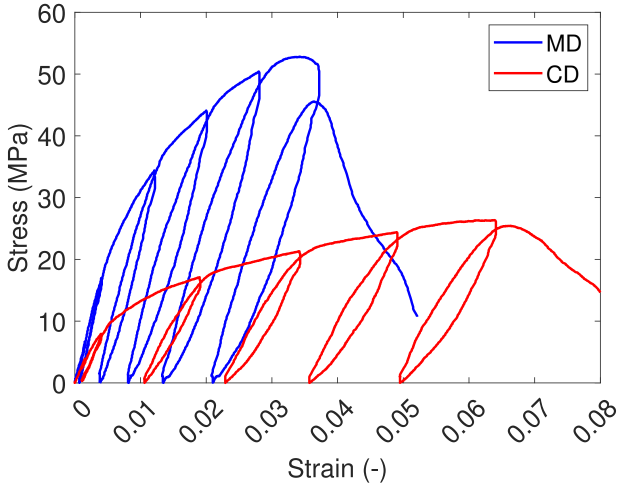

(a)

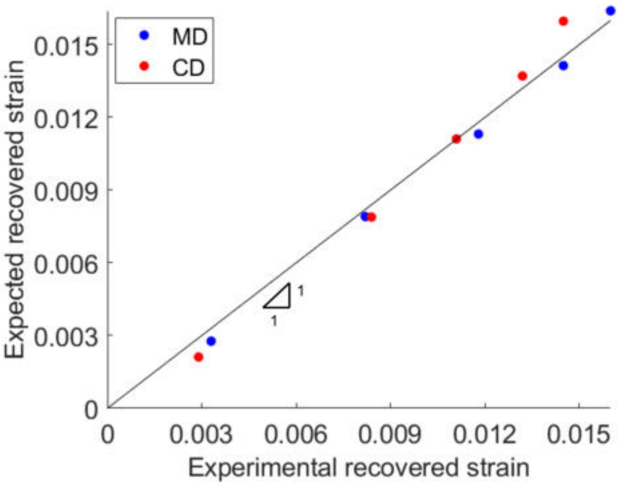

(b)

Figure 15: (a) Stress-strain curves from cyclic tests with variable amplitude strain conducted on Material 3 in the MD and CD directions. (b) Expected vs. and experimentally measured recovered strains at zero stress during unloading.

The first aspect investigated is the effect of randomness of the network for the set of parameters identified in the previous section. As previously outlined, in fact, the proposed model involves the construction of networks comprising fibers characterized by stochastic variations in length, orientation, and mean free path. The model is in fact not a pure cross-sectional model, since the parameters include also the free segment length of the fibers, which is an additional information relevant for this type of networks and includes longitudinal features of the network. This allows for a more comprehensive analysis that acknowledges the non-affine behavior introduced by phenomena like fiber recruitment and debonding failure To evaluate the impact of this randomness, we repeated a series of 100 simulations by extracting the parameters of the fibers from the statistical distributions in each run. Figure 16 presents the mean value of these simulations (dashed line) accompanied by a shaded region representing the standard deviation from the mean. Results show that the underlying randomness of the network properties have a minimal influence on the model outcomes due to the large size of the fibers accounted in the model. Previous results in the literature [34] showed that the macroscopic mechanical behavior of paper is strongly influenced by the inter-fiber bond strength and fiber elongation. To gain an insight into these effects, we conducted simulations with three distinct values of ϵ^{max}: 0.01, 0.015, and 0.022. High values of this parameter can be obtained by exerting a higher pressure during wet pressing of paper, or by adding some chemical additives to increase bonding during the production process. Simulation results are shown in Fig. 17(a) and clearly demonstrate that the strength of fiber-to-fiber bonds has a profound effect on the overall strength of paper materials, without significantly altering the initial stiffness and the ductility of the paper specimen. This result can be explained by the fact that fibers requiring a higher strain to debond contribute more substantially to the load-bearing capacity of the paper. Consequently, papers with stronger inter-fiber bonds exhibit higher maximum forces at the point of failure.

The influence of fiber elongation at failure, on the other hand, has been analysed by simulating three networks with ϵ^{f} equal to 0.028, 0.04 and

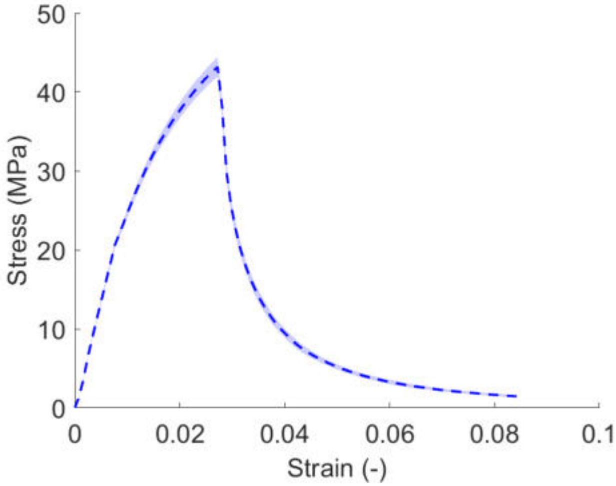

(a) Loading in the machine direction

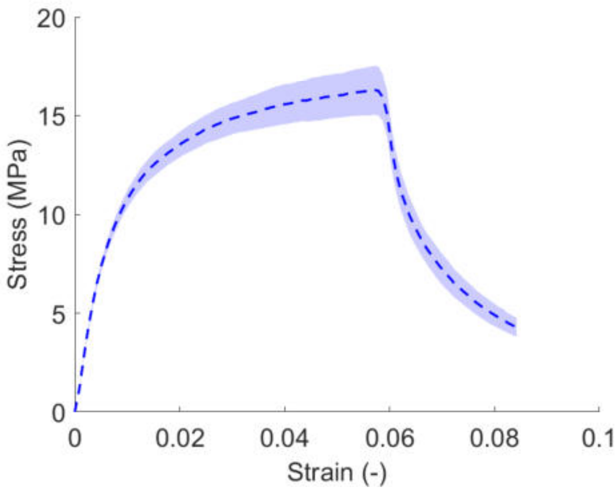

(b) Loading in the cross-machine direction

Figure 16: Mean stress-strain diagram of 100 simulations (dashed line); the shaded area represents the envelope related to the standard variation from the mean value.

0.06, while keeping other parameters constant. The outcomes of these simulations shown in Fig. 17(b) pinpoint that this parameter has a strong impact on paper ductility and also on the load-carrying capacity.

The mechanical properties of fibers, which eventually affect the fibers' stiffness K in the present model, can be changed during paper-making process by adding additives or in case of recycled fibers [82, 83, 84]. Results of simulations of fiber networks with different values of the Young's modulus equal to 11, 21, and 31 GPa are shown in Fig. 18(a). Stiffer fibers result in networks with increased stiffness and also a higher peak force. This outcome not only provides valuable insights into the underlying mechanics of paper materials but also carries practical significance. Specifically, it implies that according to [82], since recycled papers characterized by enhanced fiber stiffness compared to the virgin one, could possess the potential for greater mechanical robustness.

The role played by strain redistribution, which essentially means that when one fiber of the simulated paper network fails some of its strain is redistributed to its neighboring fibers, is herein analyzed. In the present model, redistribution has been confined to the closest fiber neighbors, but it could be extended to include a wider non-locality. Figure 18(b) shows three force-displacement curves, each one representing a paper network response under tensile loading with three different strain redistribution factors $r = 0.005$, 0.08, and 0.2. Higher strain redistribution anticipates the achievement of the peak load and, at the same time, it flattens the curve before the softening branch.

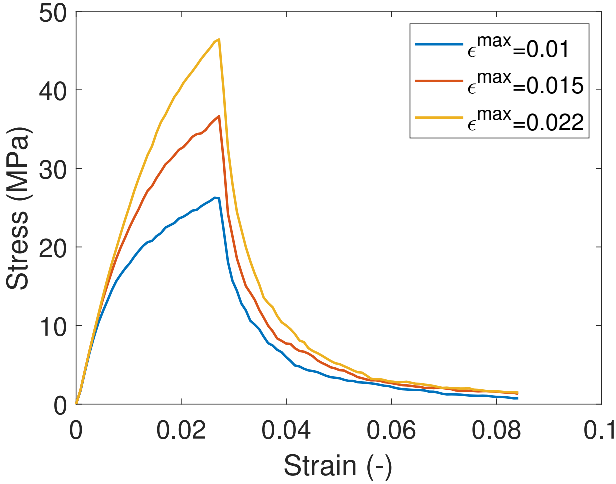

(a) Effect of ϵ^{max}

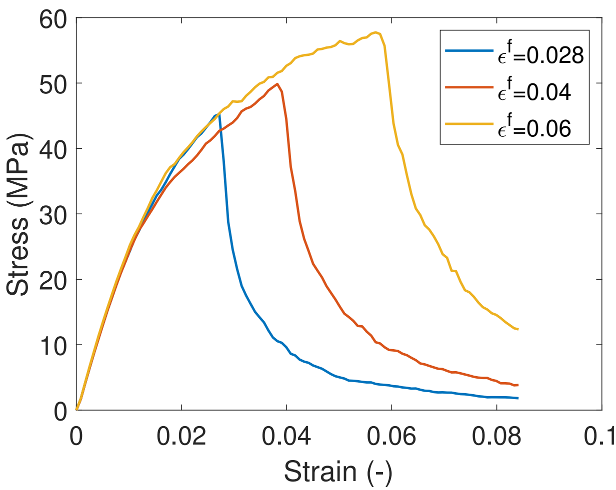

(b) Effect of ϵ^{f}

Figure 17: Effect of (a) inter-fiber bond strength, and (b) fiber elongation at failure.

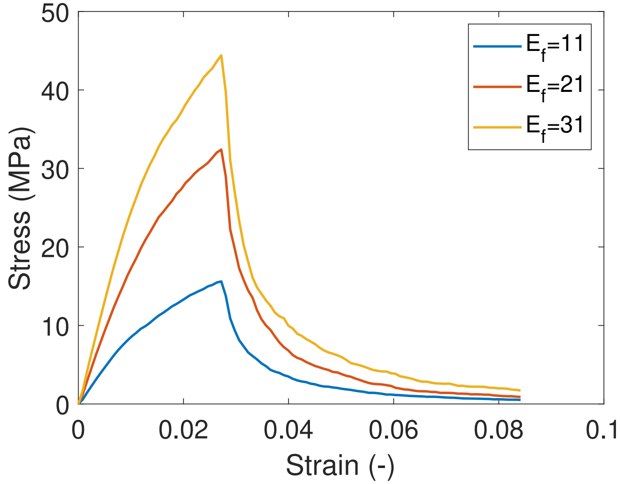

(a)

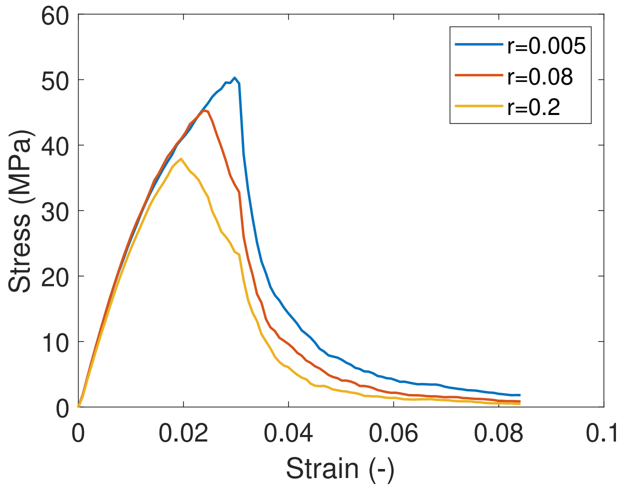

(b)

Figure 18: Effect of (a) the Young's modulus of fibers, and (b) strain redistribution factor.

Chapter 3

Nonlinear anisotropic hypo-elastic continuum models for paper materials and their relation to statistical micro-mechanics [1]

One recent study on continuum modeling of paper materials is the work presented in [86] which introduces an elasto-plastic model coupled with a phase-field approach to simulate fracture in orthotropic paperboard. The model effectively addresses the continuum representation of paper as an orthotropic material, incorporating both ductility and fracture processes. However, several research questions remain open, especially in relation to model parameters identification. The internal length scale of phase field fracture, for instance, should depend on the microstructural properties of the cellulose fiber network, but no correlation is known at the moment. Similarly, testing paper specimens in uniaxial tension under various loading directions with respect to its material orientation often required the

[1] This chapter is based on our own publication Fallah, Lenarda, and Paggi [85].

choice of different sets of elasto-plastic parameters, suggesting a potential limitation for the model's forecasting ability. Additionally, the complexity of elasto-plastic models, particularly those incorporating phase-field methods, necessitates tailored computational techniques, which are computationally expensive. *This underscores the need for continuum models as simple as possible whose parameters can be directly related to microstructural and morphological paper properties.*

Moreover, the majority of current models primarily focus on uniaxial stress states. Although they are undoubtedly important for standard material testing, they do not fully represent the real-world loading conditions of paper and packaging. Multiaxial stress states still remain largely unexplored and their simulation would enable the development of digital twin models for complex packaging design.

To address the above challenges, we propose an approximated formulation for elasto-plasticity applicable to monotonic loading conditions within the framework of nonlinear hypo-elasticity. Based on the evidence that paper is made of random fibers not embedded into a matrix like composite materials, and that uniaxial tensile tests reveal that failure of the fibers is triggered by stretching along the direction of the maximum principal strain, an anisotropic damage variable function of the maximum principal strain, ϵ_1, and its direction with respect to the mean fiber orientation, $\overline{\phi}$, is proposed. This damage function is then used to degrade the constitutive tensors of an orthotropic constitutive model and of a simplified isotropic model with an effective elastic modulus function of $\overline{\phi}$. We will show that the parameters of those continuum models can be fully identified from uniaxial tensile tests on plain specimens. Their application to biaxial stress states proves the validity of the initial assumption and the reliability of the approach and its use in engineering practice.

3.1 Paper material modeling at the micro- and macro-scales

At the micro-scale, the fibrous network can be explicitly modeled using a statistical mechanics framework [59]. The orientation of a cellulose

fiber can be defined by an angle α measured with respect to the $x-$axis in the global reference frame shown in Fig. 19 and the fiber population will have an average orientation angle μ_α. This is the result of the paper manufacturing process, since the direction of machining/rolling (MD) is aligning the majority of cellulose fibers in that direction. The orthogonal direction is usually called cross-machining direction (CD). Fibers are then cross-linked along several points, and this is crucial for their activation during the loading process and their progressive failure. Curvy cellulose fibers with a low degree of cross-linking are in fact progressively put in tension and a certain amount of strain is spent to realign those fibers along the direction of loading, a phenomenon that shares some similarities with the recruitment of collagen fibers in biological tissues [87] and that has been shown in [59] to occur also in low density paper where a matrix embedding the fibers is absent. For higher strains, the mechanical response becomes nonlinear and it is the result of a progressive failure of the network through debonding of cross-linking between fibers, which can anticipate or can be anticipated by fiber breakage. *Both failure phenomena tend to be driven by the direction where the principal strain is maximum and strongly depend on the degree of fibers cross-linking.*
As demonstrated in [59], the statistical mechanics approach can predict the degradation of the uniaxial stress-strain response of paper samples in the MD and CD directions. In Sec. 2.1 we recast the discrete fiber model in [59] within a continuous probabilistic framework, to gain further insight into material anisotropy and damage evolution. Moreover, the statistical mechanics model is exploited for the prediction of the mechanical response of a representative volume element (RVE) of the continuum, to be called by the macro-scale models at the material point level to provide further insight into the failure mechanisms at the micro-scale.
At the macro-scale, the most general scenario for arbitrary boundary conditions and geometry is a lack of symmetry (like in case of a hole or any other geometrical feature that causes localized stress concentrations as in the sketch on the left of Fig. 19). Therefore, the strain field is no longer uniaxial and a nonuniform distribution takes place over the domain Ω. This is evidenced by the maximum principal strain, ϵ_1, whose value and

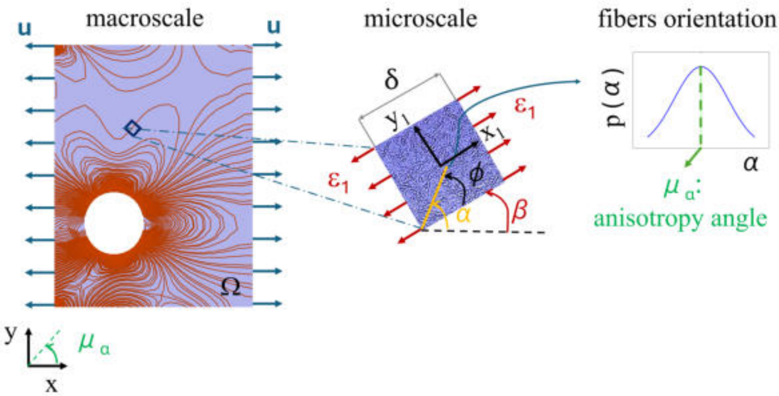

Figure 19: Sketch illustrating a paper network occupying the domain Ω at the macro-scale, with applied displacements on its boundaries and a nonuniform strain field. In each material point, the micro-scale model includes the information on the statistical distribution of fibers orientation.

direction change over the domain in Fig. 19. Consequently, the stress and strain fields are inherently biaxial. At each material point, considering the peculiar paper composition, the elastic response of the material is anisotropic, and in particular orthotropic, being the mechanical properties unique and independent in three mutually perpendicular directions, two in the plane and one out-of-plane. As anticipated, in the engineering practice, the machining direction (MD) and the cross-machining direction (CD) are typically characterized in the laboratory through uniaxial tensile tests. The MD direction is tested by aligning μ_α with the direction of loading β, while the CD direction is tested by rotating μ_α by $\pi/2$ with respect to the direction of loading.

At the continuum scale, damage and failure of paper has been promisingly modeled in the literature using anisotropic elasto-plastic models coupled with damage mechanics [48] or elasto-plastic formulations coupled with phase field fracture [86]. Although they are potentially very accurate, they are rather complex for the engineering practice. Moreover, the rela-

tion between the constitutive parameters of such continuum models and the morphological and mechanical features of the underlying network material at the micro-scale is still an open question.
In Sec. 3.1.2 we propose new continuum formulations for paper damage within the nonlinear elasticity framework, as a simpler yet effective computational approach that simplifies elasto-plasticity and can be applied to monotonic loading. In Sec. 3.1.3 we will make an attempt to establish the relations between the macro-scale continua and the micro-scale statistical mechanics model that can be called at each integration point to investigate the response of the underlying RVE of paper.

3.1.1 Micro-scale statistical mechanics model

At the micro-scale, a network of cellulose fibers pressed and bonded together to form a plane specimen of paper is considered. A micro-scale statistical mechanics model can provide the response of a paper sample tested under uniaxial tension, or can be invoked to predict the response of a representative volume element (RVE) of paper in terms of principal stress vs. principal strain. In this case, the RVE should have an out-of-plane thickness t and should be of squared shape with lateral size δ large enough to contain enough cellulose fibers to be statistically representative of the whole paper [55]. Hence, since the statistical mechanics model is conceived to predict uniaxial stress-strain relations, we assume that this RVE is oriented along a local reference frame $x_1 - y_1 - z$, where x_1 is aligned along the axis of principal tensile strain, y_1 is orthogonal to x_1 in the plane, and z is aligned with the out-of-plane direction. Moreover, a fixed global reference frame $x - y - z$ is introduced at the macro-scale to define the average inclination of the fiber distribution, μ_α, and the generic angle of inclination of a fiber, α. Hence, each fiber deviates from the average angle by the quantity $\alpha - \mu_\alpha$.
From the physical point of view, one can image that a cut of the RVE in the direction y_1 leads to $i = 1, \ldots, N_f$ fibers crossing that cross-section, for each layer $j = 1, \ldots, N_l$ of fibers pressed together in the $z-$direction.

The total number of crossed fibers is given by $N = N_l N_f$, where:

$$N_f = \rho_c \delta. \tag{3.1}$$

Here, ρ_c represents the fiber density of a layer measured as the number of fibers cut by a straight cross-section, divided by the length of the cross-section segment (number of fibers/length). This quantity can be experimentally determined from paper surface images taken by a microscope by counting fibers crossed by a line. The average width of fibers cut by the above cross-section is called d, and its average thickness in the $z-$direction is called t_f. Hence, each fiber has an average cross-sectional area $A \sim d t_f$, and an axial stiffness $K = E_f A$, where E_f is Young's modulus of fibers. The exact shape of the cross-section is not needed in the present model and it can be determined as a free parameter to fit the experimental stiffness of a paper sample. The bending stiffness of a fiber is assumed to be negligible for the type of paper herein analyzed. Therefore, we implicitly assume that a single cellulose fiber primarily contributes to stress transfer along its axial direction. The number of layers N_l in the model can be estimated as:

$$N_l = \frac{t}{d^{\max}} \tag{3.2}$$

where $d^{\max}$ denotes the maximum fiber width and t the paper sheet thickness, that can be accurately deduced from the observation of the paper surface.

The nonlinear response of the RVE is the result of the emergent response of the ensemble of the individual behaviors of the cellulose fibers. In this regard, consistent with the discrete statistical mechanics model in [59], each fiber is assumed to contribute when its strain exceeds a threshold value for recruitment, ϵ^r. Results in [59] have shown that the deformation to realign curvy fibers to recover their straight configuration necessary to achieve their full load carrying capacity has some analogies with the response of fibrous collagen tissues [87]. This can relevant for low density paper materials or for tissues produced by electrospinning that do not possess any matrix embedding the fibers. For dense fibrous papers, ϵ^r becomes smaller and smaller up to becoming negligible.

The fiber responds linearly elastically to the applied axial strain, up to reaching a level (failure strain ϵ^f) which is the minimum between the strain for debonding of its cross-links, and the strain for fiber breakage. Here, we remark that those quantities may depend on the direction of loading with respect to the orientation of the fibers, due to manufacturing reasons. Hence, it is convenient to define the angle ϕ as follows:

$$\phi = \alpha - \beta, \tag{3.3}$$

where β is the direction of the principal strain ϵ_1 computed with respect to the global reference system $O - x - y$. We also introduce an average angle $\overline{\phi}$ for the RVE computed as:

$$\overline{\phi} = \langle \alpha \rangle - \beta = \mu_\alpha - \beta, \tag{3.4}$$

where the operator $\langle \cdot \rangle$ denotes an ensemble average of the fiber orientations, which is giving the expected mean value μ_α of the fiber orientation distribution.
Each fiber is assumed to respond with an axial force proportional to its axial stretch within the limits $\epsilon^r \leq \epsilon < \epsilon^f$:

$$f = \begin{cases} 0, & \text{if } \epsilon < \epsilon^r \\ K\epsilon, & \text{if } \epsilon^r \leq \epsilon < \epsilon^f \\ 0, & \text{if } \epsilon \geq \epsilon^f \end{cases} \tag{3.5}$$

where, as we will discuss in the sequel, it is important to consider ϵ^r and ϵ^f not constant but variable from fiber to fiber as a result of the paper production process. The axial strain acting on a fiber, ϵ, is related to the applied maximum principal strain ϵ_1 and to the cosine of the fiber angle ϕ:

$$\epsilon = \epsilon_1 \cos(\phi) = \epsilon_1 \cos(\alpha - \beta). \tag{3.6}$$

The reacting force of the cellulose fiber along the x_1−axis is computed by projecting f from the axial direction of the inclined fiber to the direction defined by the principal axis x_1, that is:

$$F = f\cos(\phi) = \begin{cases} 0, & \text{if } \epsilon < \epsilon^r \\ K\epsilon_1 \cos^2(\alpha - \beta), & \text{if } \epsilon^r \leq \epsilon < \epsilon^f \\ 0, & \text{if } \epsilon \geq \epsilon^f \end{cases} \tag{3.7}$$

The micromechanical model is therefore predicting the average stress σ_1 of the RVE subject to ϵ_1 through the computation of the total load in response to ϵ_1 as the integral of the fiber force F multiplied by the joint probability density function (PDF) of the multivariate distribution related to the probability of finding a fiber with a given orientation α and a *mean free path* or *free segment length* λ, multiplied by the number N of fibers along the cross-section and divided by the nominal cross-section area δt:

$$\sigma_1 = \frac{N}{\delta t}\int_{\alpha=-\pi/2}^{\pi/2}\int_{\lambda=\lambda_{\min}}^{\lambda_{\max}} F\,p(\alpha,\lambda)\,\mathrm{d}\alpha\,\mathrm{d}\lambda \tag{3.8a}$$

$$= \frac{\rho_c}{d_{\max}}\int_{\alpha=-\pi/2}^{\pi/2}\int_{\lambda=\lambda_{\min}}^{\lambda_{\max}} F\,p(\alpha,\lambda)\,\mathrm{d}\alpha\,\mathrm{d}\lambda. \tag{3.8b}$$

The parameter λ defines the average distance measured along the cellulose fiber between two subsequent bonds [74], is related to the degree of cross-linking, and it can be assessed experimentally from the visual inspection of the paper surface with a microscope.
According to [59], λ is responsible for the values of ϵ^r and ϵ^f:

$$\epsilon^r = \epsilon^r_{\max}\left(\frac{\lambda-\lambda_{\min}}{\lambda_{\max}-\lambda_{\min}}\right), \quad \lambda_{\min}\le\lambda\le\lambda_{\max}, \tag{3.9a}$$

$$\epsilon^f = \min\left\{\epsilon^d\left(\frac{\lambda_{\text{avg}}}{\lambda}\right), \epsilon^b\right\}, \quad \lambda_{\min}\le\lambda\le\lambda_{\max}, \tag{3.9b}$$

where $\epsilon^r_{\max}$ is the maximum value of the activation strain for the non-straight fibers (achieved for $\lambda=\lambda_{\max}$). The parameter λ_{avg} is the average mean segment length estimated from confocal microscopy images by dividing a fiber length by the number of bonds observed along its length, and averaging over a statistically representative number of fibers. The parameters $\lambda_{\max}$ and $\lambda_{\min}$ correspond to the maximum and minimum distances between two adjacent bonds within the network. As previously anticipated, ϵ^d and ϵ^b are not constant but do depend on the angle ϕ as a result of the manufacturing process which is leading to an anisotropic response of fiber failure. Equation (3.9b) implies that fibers having $\lambda < \lambda_{\text{avg}}$ may have breakage occurring before debonding, and this is physically motivated by their strong cross-linking that make them stiffer and, under

an applied strain, easier to reach their strength. On the other hand, fibers having $\lambda > \lambda_{\text{avg}}$ are more likely to fail due to cross-linking debonding rather than breakage.
This joint PDF $p(\alpha, \lambda)$ is difficult to determine in closed form, since it involves the interdependencies between geometrical features that are intrinsic properties of the fiber network resulting from the production process, and cannot be estimated from testing of individual fibers. However, a reasonable approximation is to consider the two variables α and λ as statistically independent, which simplifies the expression of the PDF as:

$$p(\alpha, \lambda) = p_\alpha(\alpha) \times p_\lambda(\lambda). \tag{3.10}$$

In this case, $p_\alpha(\alpha)$ can be determined from the statistical analysis of the inclination of fibers on the surface of paper sheets, and it can be reasonably well represented by a truncated Gaussian distribution centered in 0 as proposed in [59], as an alterative to von Mises or wrapped Cauchy distributions used in [79]:

$$p_\alpha(\alpha) = \begin{cases} \dfrac{\dfrac{1}{\sigma_\alpha\sqrt{2\pi}} \exp\left[-\dfrac{1}{2}\left(\dfrac{\alpha-\mu_\alpha}{\sigma_\alpha}\right)^2\right]}{\sigma_\alpha\left[\Phi_\alpha\left(\dfrac{\pi/2}{\sigma_\alpha}\right) - \Phi_\alpha\left(\dfrac{-\pi/2}{\sigma_\alpha}\right)\right]}, & \text{if } -\dfrac{\pi}{2} \leq \alpha \leq \dfrac{\pi}{2} \\ 0, & \text{otherwise} \end{cases} \tag{3.11}$$

where Φ_α is the cumulative function of the standard Gaussian PDF and σ_α is the standard deviation that is approximately equal to 1 to have about 20% of fibers oriented at $\alpha = \pi/2$ as reported in [79].
Moreover, according to [74], λ is typically distributed according to a truncated exponential distribution:

$$p_\lambda(\lambda) = \frac{\lambda_{\text{avg}} \exp\big(-\lambda_{\text{avg}}\lambda\big)}{\exp\big(-\lambda_{\text{avg}}\lambda_{\min}\big) - \exp\big(-\lambda_{\text{avg}}\lambda_{\max}\big)}, \quad \lambda_{\min} \leq \lambda \leq \lambda_{\max}. \tag{3.12}$$

Therefore, the final expression for the average traction σ_1 reads:

$$\sigma_1 = \frac{\rho_c}{d_{\max}} \int_{\alpha=-\pi/2}^{\pi/2} \int_{\lambda=\lambda_{\min}}^{\lambda_{\max}} F\, p_\alpha(\alpha)\, p_\lambda(\lambda)\, \mathrm{d}\alpha\, \mathrm{d}\lambda. \tag{3.13}$$

The integrals that provide the expected axial force acting along the axis x_1 in response to ϵ_1 cannot be solved in closed form, but can be efficiently addressed numerically. Following the methodology proposed in [59], integrals are transformed into discrete sums applied to a randomly generated population of fibers (i, j) with $i = 1, \ldots, N_f$ and $j = 1, \ldots, N_l$ extracted from the prescribed PDFs. This approach leads to a kind of fiber-bundle model with all the inherent stochastic features, where the continuous variables α, λ, ϕ and the functions ϵ, f and F are also discretized. In addition to pure cross-sectional information, the model incorporates important longitudinal information on the fiber network through the mean free path λ of each fiber, which is a crucial aspect for cellulose paper materials.
An approximate estimation of the relation between σ_1 and ϵ_1 in the linear elastic regime can be obtained by assuming $\epsilon^r = 0$ and considering a maximum strain such that it does not lead to fiber debonding or breakage of any fiber. Therefore, in this case, the integrand F becomes dependent only on α and $\int p_\lambda(\lambda)\mathrm{d}\lambda = 1$ can be factorized:

$$\sigma_1 = \frac{K\rho_c}{d_{\max}}\epsilon_1 \int_{-\pi/2}^{\pi/2} \cos^2(\alpha - \beta)\, p_\alpha(\alpha)\, \mathrm{d}\alpha. \tag{3.14}$$

If we consider the material oriented such that $\mu_\alpha = 0$ and if paper is loaded in the direction $\beta = 0$, then we are testing the MD direction and the numerical integration carried out with a Gaussian quadrature formula leads:

$$\sigma_1 = \frac{K\rho_c}{d_{\max}}\epsilon_1 \int_{-\pi/2}^{\pi/2} \cos^2(\alpha)\, p_\alpha(\alpha)\, \mathrm{d}\alpha = 0.613\frac{K\rho_c}{d_{\max}}\epsilon_1 = E_{MD}\,\epsilon_1, \tag{3.15}$$

where the multiplicative coefficient between ϵ_1 and σ_1 gives an estimate of the elastic modulus E_{MD}. Following a similar procedure, setting $\beta = \pi/2$, we assess the elastic modulus of paper in the cross-machining direction CD:

$$\begin{aligned}\sigma_1 &= \frac{K\rho_c}{d_{\max}}\epsilon_1 \int_{-\pi/2}^{\pi/2} \cos^2(\alpha - \pi/2)\, p_\alpha(\alpha)\, \mathrm{d}\alpha \\ &= \frac{K\rho_c}{d_{\max}}\epsilon_1 \int_{-\pi/2}^{\pi/2} \sin^2(\alpha)\, p_\alpha(\alpha)\, \mathrm{d}\alpha = \frac{0.386\, K\rho_c}{d_{\max}}\epsilon_1 = E_{CD}\,\epsilon_1.\end{aligned} \tag{3.16}$$

As an interesting result, this provides a rough estimate of the degree of anisotropy through the ratio $E_{CD}/E_{MD} \simeq 0.386/0.613 \cong 0.6$, under the simplification of negligible cross-linking effects and within the linear elastic regime.

3.1.2 Macro-scale nonlinear hypo-elastic continuum models

A nonlinear hypo-elastic continuum mechanics framework is herein proposed to simulate the behaviour of paper materials at the macroscale, accounting for the key nonlinear features observed in experiments, as a simplified, yet accurate, alternative for monotonic loading to elasto-plastic formulations.
Hypo-elasticity is used to model materials that exhibit nonlinear, but reversible, stress-strain behavior even at small strains. Its most common application is in the so-called 'deformation theory of plasticity', which is an approximation of the behavior of metals loaded beyond the elastic limit. A hypo-elastic material deforms reversibly and the strain in the specimen depends only on the stress applied to it, while it does not depend on the rate of loading or the history of loading [88][Ch. 3.3]. Stress is a nonlinear function of strain, even when strains are small, which is a situation observed in paper materials which show a nonlinear stress-strain curve as a result of the progressive failure of cellulose fibers.
Here, we extend the basic isotropic formulation of a hypo-elastic material in [88][Ch. 3.3] to the anisotropic case, to capture the observed directional dependence of the mechanical properties of paper [89].
Paper is essentially an orthotropic material, whose constitutive relation is:

$$\mathbf{C} = \frac{1}{1-\nu_{xy}\nu_{yx}} \begin{bmatrix} E_x & \nu_{xy}E_y & 0 \\ \nu_{yx}E_x & E_y & 0 \\ 0 & 0 & (1-\nu_{xy}\nu_{yx})G \end{bmatrix}, \qquad (3.17)$$

where $\nu_{yx}E_x = \nu_{xy}E_y$ for symmetry considerations. Introducing $\nu =$

$\sqrt{\nu_{xy}\nu_{yx}}$ as in [90], we can also use the following equivalent expression:

$$\mathbf{C} = \frac{1}{1-\nu^2}\begin{bmatrix} E_x & \nu\sqrt{\dfrac{E_y}{E_x}}E_x & 0 \\ \nu\sqrt{\dfrac{E_x}{E_y}}E_y & E_y & 0 \\ 0 & 0 & (1-\nu^2)G \end{bmatrix}. \tag{3.18}$$

Here, E_x and E_y can be conveniently defined by setting a reference frame such that the x direction coincides with the MD direction and the y direction coincides with the CD direction, which is the case corresponding to $\mu_\alpha = 0$. For any rotation of the fiber distribution μ_α, the constitutive tensor is computed as:

$$\mathbf{C}^*(\mu_\alpha) = \mathbf{R}(\mu_\alpha)\,\mathbf{C}(\mu_\alpha = 0)\,\mathbf{R}'(\mu_\alpha), \tag{3.19a}$$

$$\mathbf{R}(\mu_\alpha) = \begin{bmatrix} \cos^2(\mu_\alpha) & \sin^2(\mu_\alpha) & \sin(2\mu_\alpha) \\ \sin^2(\mu_\alpha) & \cos^2(\mu_\alpha) & -\sin(2\mu_\alpha) \\ -\dfrac{1}{2}\sin(2\mu_\alpha) & \dfrac{1}{2}\sin(2\mu_\alpha) & \cos^2(\mu_\alpha) - \sin^2(\mu_\alpha) \end{bmatrix}. \tag{3.19b}$$

We suppose now that the material undergoes damage as a result of stretching in the direction where the tensile strain is maximum, and we make the fundamental assumption that the maximum principal strain ϵ_1 in a point is the driving parameter for an anisotropic damage variable $d(\epsilon_1, \overline{\phi})$. This assumption will be eventually tested in the validation section 3.1.3. The angle β, in the context of the continuum model, is the angle corresponding with the direction of the maximum principal strain. Based on these assumptions, we define the anisotropic damage variable function of ϵ_1 and $\overline{\phi}$ as:

$$d(\epsilon_1, \overline{\phi}) = \begin{cases} 0, & \epsilon_1 < \epsilon_y \\ a(\overline{\phi})\dfrac{\left[\epsilon_1 - \epsilon_y(\overline{\phi})\right]^{n(\overline{\phi})}}{\epsilon_1}, & \epsilon_y \le \epsilon_1 < \epsilon_1^c \\ 0.99, & \epsilon_1 \ge \epsilon_1^c \end{cases} \tag{3.20}$$

where the last condition has been introduced to avoid ill-conditioning when the material is fully damaged. Therefore, for $\epsilon_1 < \epsilon_y$, no damage develops, and afterwards damage builds up according to the above power-law equation. Consequently, the damaged constitutive tensor is computed as:

$$\mathbf{C}^*_d(\mu_\alpha, \epsilon_1, \overline{\phi}) = (1-d)\mathbf{C}^*. \tag{3.21}$$

In absence of body forces, the strong form of equilibrium for a body occupying the domain Ω is governed by the linear momentum equation, accompanied by the Dirichlet and Neumann boundary conditions specified on $\partial\Omega_D$ and $\partial\Omega_N$, respectively, as follows:

$$\nabla \cdot \boldsymbol{\sigma} = \mathbf{0}, \text{in } \Omega \tag{3.22a}$$

$$\mathbf{u} = \mathbf{u}_D, \text{on } \partial\Omega_D \tag{3.22b}$$

$$\boldsymbol{\sigma} \cdot \mathbf{n} = t_N, \text{on } \partial\Omega_N \tag{3.22c}$$

where $\boldsymbol{\sigma} = \mathbf{C}^*_d \boldsymbol{\epsilon}$ in the Voigt notation, $\mathbf{u}_D$ denotes the imposed displacement, $\mathbf{n}$ is the outward unit normal vector on $\partial\Omega_N$, and t_N is the corresponding applied normal traction vector.

The weak form of the differential problem in (3.22) is obtained by virtue of the Principle of Virtual Work:

$$\int_\Omega \boldsymbol{\epsilon}'(\mathbf{v})\, \mathbf{C}^*_d\, \boldsymbol{\epsilon}(\mathbf{u})\, t\, \mathrm{d}\Omega - \int_{\partial\Omega_N} t_N\, \mathbf{v}\, t\, \mathrm{d}\Gamma = 0, \tag{3.23}$$

where t is the sheet thickness and $\boldsymbol{\epsilon}(\mathbf{u}) = (\partial u_x/\partial x, \partial u_y/\partial y, \partial u_x/\partial y + \partial u_y/\partial x)'$ and $\boldsymbol{\epsilon}(\mathbf{v}) = (\partial v_x/\partial x, \partial v_y/\partial y, \partial v_x/\partial y + \partial v_y/\partial x)'$ represent, respectively, the strain vectors associated with the real and the virtual displacement fields $\mathbf{u} = (u_x, u_y)'$ and $\mathbf{v} = (v_x, v_y)'$. The apostrophe symbol $(')$ denotes the transpose of vectors and matrices.

Equation (3.23) is discretized within the finite element method to obtain a set of algebraic equations:

$$\int_\Omega (1-d)\mathbf{B}'\, \mathbf{C}^*\, \mathbf{B}\, \mathbf{d}_\mathbf{u}\, t\, \mathrm{d}\Omega - \int_{\partial\Omega_N} t_N\, \mathbf{N}\, t\, \mathrm{d}\Gamma = 0, \tag{3.24}$$

where the relations $\boldsymbol{\epsilon}(\mathbf{u}) = \mathbf{B}\mathbf{d}_\mathbf{u}$, $\boldsymbol{\epsilon}(\mathbf{v}) = \mathbf{B}\mathbf{d}_\mathbf{v}$, $\mathbf{u} = \mathbf{N}\mathbf{d}_\mathbf{u}$ and $\mathbf{v} = \mathbf{N}\mathbf{d}_\mathbf{v}$ have been introduced, being $\mathbf{d}_\mathbf{u}$ and $\mathbf{d}_\mathbf{v}$ the vectors containing the real and the virtual nodal displacements, $\mathbf{B}$ the matrix operator containing the

derivatives of the shape functions, and $\mathbf{N}$ the matrix of the shape functions, to be specialized according to the chosen finite element topology.
Due to the nonlinearity introduced by the degradation function, a nonlinear solution scheme has to be invoked. Introducing the Newton-Raphson implicit algorithm, we write the residual vector at the iteration $k+1$ as:

$$\mathbf{p}^{k+1} = \mathbf{p}^k + \left(\frac{\partial \mathbf{p}}{\partial \mathbf{d_u}}\right)_k \Delta \mathbf{d_u}^{k+1} = \mathbf{0}, \tag{3.25a}$$

$$\mathbf{p}^k = \int_\Omega (1-d^k)\mathbf{B}'\mathbf{C}^*\mathbf{B}\,\mathbf{d_u}^k\, t\,\mathrm{d}\Omega - \int_{\partial\Omega_N} t_N\,\mathbf{N}\,t\,\mathrm{d}\Gamma, \tag{3.25b}$$

$$\begin{aligned}\left(\frac{\partial \mathbf{p}}{\partial \mathbf{d_u}}\right)_k &= \int_\Omega (1-d^k)\mathbf{B}'\mathbf{C}^*\mathbf{B}\,t\,\mathrm{d}\Omega \\ &\quad - \int_\Omega \left[\frac{\partial d^k}{\partial \epsilon_1}\frac{\partial \epsilon_1^k}{\partial \boldsymbol{\epsilon}} + \frac{\partial d^k}{\partial \overline{\phi}}\frac{\partial \overline{\phi}}{\partial \boldsymbol{\epsilon}}\right]\frac{\partial \boldsymbol{\epsilon}}{\partial \mathbf{d_u}}\mathbf{d_u}^k\ (\mathbf{B}'\mathbf{C}^*\mathbf{B})\ t\,\mathrm{d}\Omega.\end{aligned} \tag{3.25c}$$

The solution of the linearized set of equations (3.25) provides the increment $\Delta\mathbf{d_u}^{k+1}$ to update the solution vector at the next iteration, $\mathbf{d_u}^{k+1} = \mathbf{d_u}^k + \Delta\mathbf{d_u}^{k+1}$. The algorithm proceeds with a rate of convergence at most quadratic until the norm of the correction $\|\Delta\mathbf{d_u}^{k+1}\|$ is less than a user-defined tolerance.
The non-standard terms in square brackets in Eq.(3.25c) evaluated at the previous iteration k, multiplied by $\partial\boldsymbol{\epsilon}/\partial\mathbf{d_u} = \mathbf{B}$ and $\mathbf{d_u}^k$ give a scalar coefficient pre-multiplying the standard stiffness matrix $\mathbf{B}'\mathbf{C}^*\mathbf{B}$ and, for the range $\epsilon_y \le \epsilon_1 < \epsilon_1^c$, the terms are not vanishing and are computed according to the following relations:

$$\frac{\partial d}{\partial \epsilon_1} = a(\phi)\frac{\epsilon_1 n(\phi)[\epsilon_1 - \epsilon_y(\phi)]^{n(\phi)-1} + [\epsilon_1 - \epsilon_y(\phi)]^{n(\phi)}}{\epsilon_1^2}, \tag{3.26a}$$

$$\frac{\partial \epsilon_1}{\partial \boldsymbol{\epsilon}} = \left(\frac{\partial \epsilon_1}{\partial \epsilon_x}, \frac{\partial \epsilon_1}{\partial \epsilon_y}, \frac{\partial \epsilon_1}{\partial \epsilon_{xy}}\right), \tag{3.26b}$$

$$\frac{\partial d}{\partial \overline{\phi}} = \frac{\partial a}{\partial \overline{\phi}}\frac{d}{a} + d\left(-\frac{n\dfrac{\partial \epsilon_y}{\partial \overline{\phi}}}{(\epsilon_1 - \epsilon_y)} + \frac{\partial n}{\partial \overline{\phi}}\log(\epsilon_1 - \epsilon_y)\right), \tag{3.26c}$$

$$\frac{\partial \overline{\phi}}{\partial \boldsymbol{\epsilon}} = \left(\frac{\partial \overline{\phi}}{\partial \epsilon_x}, \frac{\partial \overline{\phi}}{\partial \epsilon_y}, \frac{\partial \overline{\phi}}{\partial \epsilon_{xy}}\right). \tag{3.26d}$$

where ϵ_1 and $\overline{\phi}$ are evaluated based on strains at the iteration k as:

$$\epsilon_1 = \frac{\epsilon_x + \epsilon_y}{2} + \sqrt{\left(\frac{\epsilon_x - \epsilon_y}{2}\right)^2 + (\epsilon_{xy})^2}, \tag{3.27a}$$

$$\phi = \mu_\alpha - \beta = \mu_\alpha - \frac{1}{2}\tan^{-1}\left(\frac{2\epsilon_{xy}}{\epsilon_x - \epsilon_y}\right). \tag{3.27b}$$

A simpler yet quite accurate solution can also be obtained by treating the damage function explicitly, that is, by computing the damage function d from a previous pseudo-time step, which renders the problem linear. Of course, small load increments have to be used.

A second nonlinear continuum model is now proposed, where the constitutive tensor is approximated with an isotropic expression with a constant Poisson ratio ν and an elastic modulus E function of $\overline{\phi}$ in the material point, and degraded according to the same anisotropic damage function $d(\epsilon_1, \overline{\phi})$ as before. Building on this formulation, for 2D plane stress conditions we redefine $\mathbf{C}^*$ as:

$$\mathbf{C}^* = \frac{E(\overline{\phi})}{1-\nu^2}\begin{bmatrix} 1 & \nu & 0 \\ \nu & 1 & 0 \\ 0 & 0 & (1-\nu)/2 \end{bmatrix}, \tag{3.28}$$

so that $\mathbf{C}^*_d = (1 - d(\epsilon_1, \overline{\phi}))\mathbf{C}^*$. Therefore the weak form and its discretization in Eqs. (3.23) and (3.24) still hold. The linearization of the residual vector in Eq.(3.25c) presents and additional term due to the dependency of E upon $\overline{\phi}$:

$$\begin{aligned} \left(\frac{\partial \mathbf{p}}{\partial \mathbf{d_u}}\right)_k &= \int_\Omega (1-d^k)\mathbf{B}'\mathbf{C}^*\mathbf{B}\, t\, \mathrm{d}\Omega \\ &- \int_\Omega \left[\frac{\partial d^k}{\partial \epsilon_1}\frac{\partial \epsilon_1^k}{\partial \boldsymbol{\epsilon}} + \frac{\partial d^k}{\partial \overline{\phi}}\frac{\partial \overline{\phi}}{\partial \boldsymbol{\epsilon}}\right]\mathbf{B}\mathbf{d_u}^k\ (\mathbf{B}'\mathbf{C}^*\mathbf{B})\ t\, \mathrm{d}\Omega \\ &+ \int_\Omega \frac{(1-d^k)}{E^k}\frac{\partial E^k}{\partial \overline{\phi}}\frac{\partial \overline{\phi}}{\partial \boldsymbol{\epsilon}}\mathbf{B}\mathbf{d_u}^k\, (\mathbf{B}'\mathbf{C}^*\mathbf{B})\ t\, \mathrm{d}\Omega \end{aligned} \tag{3.29}$$

with the derivatives given again by Eqs. (3.26) and $\mathbf{C}^*$ evaluated as a function of E^k.

It should be emphasized that the present homogenization strategy represents a reduced-order approximation of the fibrous network response. More advanced approaches based on representative volume elements (RVE) combined with periodic boundary conditions could provide a more rigorous evaluation of the effective constitutive behavior by explicitly resolving the network topology and local microstructural interactions. However, such formulations generally involve significantly higher computational cost and greater implementation complexity. In the present work, the adopted continuum formulation was intentionally developed as a computationally efficient framework aimed at reproducing the global tensile response of paper materials while maintaining a limited number of model parameters. Therefore, the proposed approach represents a compromise between physical accuracy and computational efficiency.
Furthermore although paper exhibits an inherently anisotropic fibrous microstructure, the isotropic constitutive tensor adopted in the present formulation represents a simplified continuum approximation intended to isolate the role of the degradation mechanism governed by the maximum principal strain and its orientation relative to the average fiber direction. This choice was motivated by the excellent predictive capability previously demonstrated by the statistical micro-mechanics model under uniaxial loading conditions, despite its reduced uniaxial nature. Moreover, unlike classical composite materials, paper consists of a random network of interacting cellulose fibers without a continuous matrix phase, such that the dominant failure mechanisms are strongly associated with the principal tensile deformation direction. The isotropic approximation therefore allows a reduced and computationally efficient continuum representation while still retaining the directional dependence through the degradation law.

3.1.3 Relation between the continuum and the statistical micromechanics models

To investigate the relation between the two macro-scale continuum models and the micro-scale statistical mechanics approach, we exploit uniaxial tensile tests where the response of the three models reduces to the scalar relation $\sigma = C_d^* \epsilon$, where C_d^* is the (1,1) component of the constitutive tensor.

Benchmark experimental results have been obtained by pursuing the approach recently proposed in [59], where an experimental setup that combines a micromechanical tensile stage (DEBEN) with a confocal microscope (Leica DCM3D) is exploited to perform in-situ uniaxial tensile tests on paper samples. This setup allows for real-time mechanical testing while capturing high-resolution microstructural details, enabling the identification of key microstructural parameters. Utilizing this setup, we conducted uniaxial tensile tests on rectangular plain paper samples of $B \times L \times t$ dimensions, where $B = 20$ mm represents the width, $L = 33.1$ mm the span, and $t = 0.2$ mm the thickness of the samples. The tested papers had a density of 1230 kg/m^3. To capture the anisotropic mechanical response, a series of samples have been cut under different orientations with respect to the machining direction. Testing these samples under uniaxial tension allows determining the force-displacement curves that can be converted into stress-strain curves as customary.

Morphological parameters required by the application of the statistical micro-mechanics model have been deduced from confocal images of the paper surface, see Fig. 20 that shows a portion of a paper specimen captured using the 20× magnification, with an image size of 637 × 477 μm. The count of the visible cellulose fibers crossing an exemplary cross-section (depicted by the red line of length 477 μm) is 28, resulting in a fiber density $\rho_c = 28/477 = 0.0587$ fibers/μm. We also reported 6 layers of fibers through the thickness with a value of $d_{\max} = 39.2$ μm and a total of $N = 1174 \times 6 = 7044$ fibers.

In addition to the fiber width measurements, the minimum, maximum and average free segment lengths have been quantified as $\lambda_{\min} = 6$ μm, $\lambda_{\text{avg}} = 37$ μm, and $\lambda_{\max} = 187$ μm. The other parameters for the micro-scale statistical mechanics model, including the average cross-sectional area of fibers, $A = 230$ μm^2, and the root mean square of the fibers orientations, $\sigma_\alpha = 1$ have been taken from the literature [34, 79].

The experimental uniaxial stress-strain curves performed under the condi-

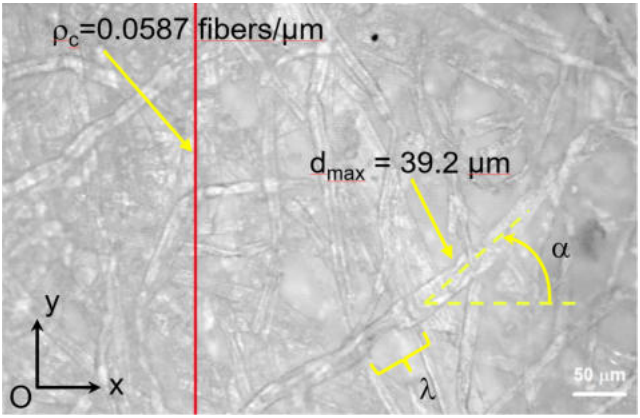

Figure 20: Confocal microscope image of a paper sample with $\rho = 1230$ kg/m^3 at 20× magnification, showing a random arrangement of cellulose fibers. The red line shows the exemplary cross-section used for computations of the morphological parameters of the micro-mechanical model.

tion $\beta = 0$ (imposed displacement along the x-direction) and for $\mu_\alpha = 0$, $\pi/12$, $\pi/6$, $\pi/4$, $\pi/3$, $5\pi/12$, and $\pi/2$ are shown in Fig. 21(a) for the tested values of $\overline{\phi} = \mu_\alpha - \beta = \mu_\alpha$. The experimental values of C_d^* in the experiments have been computed from the tangent to the stress-strain curves in the linear elastic regime in the range $3 \times 10^{-3} < \epsilon < 6 \times 10^{-3}$, see the linear red curves superimposed to the experimental data in Fig. 21(b).
In terms of mechanical quantities, the application of the micro-mechanical model required the identification of the Young modulus of the fibers, E_f, the maximum activation strain ϵ^r, the parameter ϵ^d for the distribution of fiber debonding strains, and the fiber breakage strain, ϵ^b. A very good agreement between experiments and micro-mechanical predictions has been achieved by setting constant values of $E_f = 22$ GPa and $\epsilon^r = 0.002$, see Fig. 22(a). The micromechanical model predicts also the evolution of fiber failure, see Fig.22(b).
On the other hand, we found that ϵ^d and ϵ^b have to be considered functions of $\overline{\phi}$, see Fig. 23. Quadratic equations have found to optimally interpolate

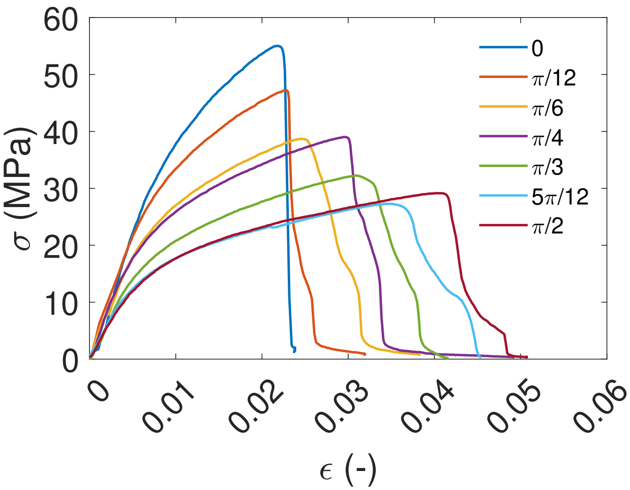

(a) Experimental results

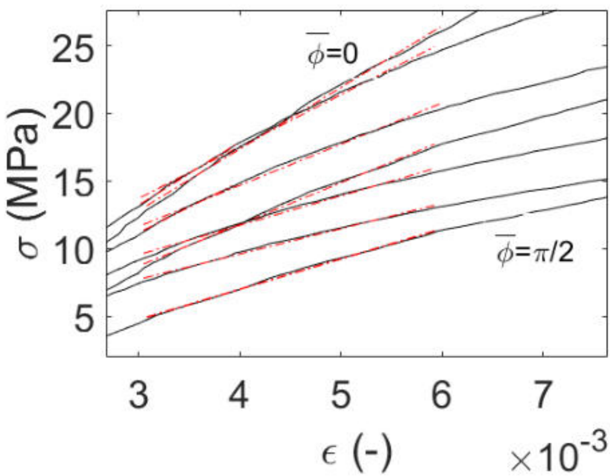

(b) Tangent elastic moduli

Figure 21: Experimental stress-strain curves from uniaxial tensile tests on plain samples, for different misalignment angles $\overline{\phi}$ from 0 to $\phi/2$.

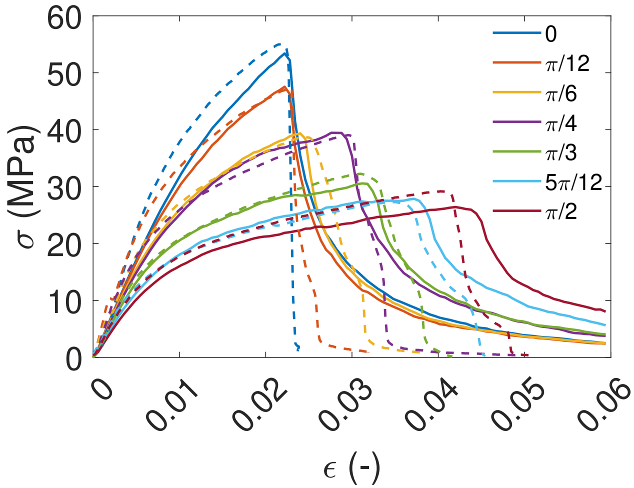

(a) Micromechanical model predictions

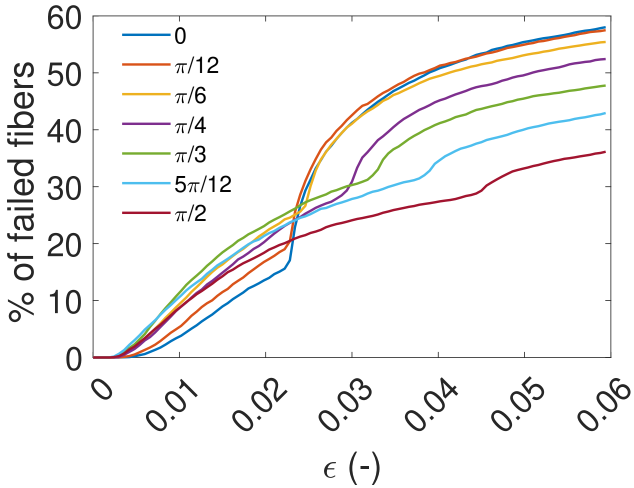

(b) Predicted evolution of fiber failure

Figure 22: Comparison between experimental results (dashed lines) and predictions by the micromechanical model (solid lines) for uniaxial tensile tests on plain samples and different misalignment angles $\overline{\phi}$ from 0 to $\pi/2$. The model is also predicting the evolution of fiber failure, Fig. 22(b).

the identified data:

$$\epsilon^d(\overline{\phi}) = 0.0059\,\overline{\phi}^2 - 0.0165\,\overline{\phi} + 0.022, \tag{3.30a}$$

$$\epsilon^b(\overline{\phi}) = 0.008\,\overline{\phi}^2 + 0.0019\,\overline{\phi} + 0.022. \tag{3.30b}$$

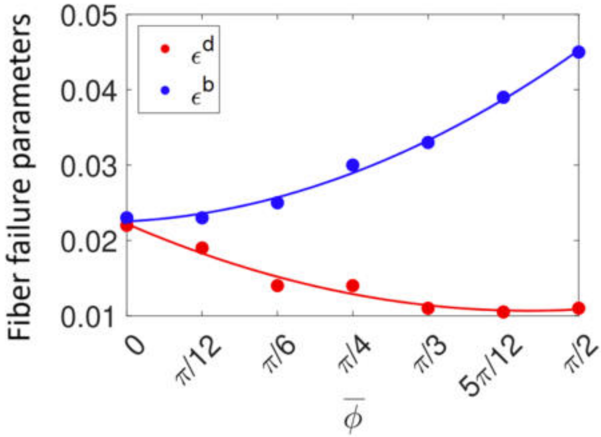

Figure 23: Identified fiber failure parameters as a function of the misalignment angle $\overline{\phi}$. The fiber debonding strain is computed as the product between ϵ^d and $(\lambda/\lambda_{\text{avg}})$ as per Eq. (3.9b). Therefore, fibers with high cross-linking may have a debonding strain lower then ϵ^b, especially for low $\overline{\phi}$.

A summary of the identified parameters entering the statistical micromechanics model is provided in Tab.5. The agreement between model predictions and experimental results in Fig. 22 is very good and the model provides interesting information on the evolution of fiber failure, with the percentage of fibers broken, debonded, and the total percentage as shown in Fig. 22(b).

Parameter	Value
ρ	1230 $\mathrm{kg/m^3}$
ρ_c	0.0587 fibers/μm
$d_{\max}$	39.2 μm
$\lambda_{\min}$	6 μm
λ_{avg}	37 μm
$\lambda_{\max}$	187 μm
μ_α	variable from 0 to $\pi/2$
σ_α	1
A	230 $\mu\mathrm{m}^2$
$\epsilon^d(\overline{\phi})$	see Eq.(30a)
$\epsilon^b(\overline{\phi})$	see Eq.(30b)

Table 5: Identified parameters of the statistical micromechanics model.

The parameters of the two continuum models for macro-scale modeling have also been identified by matching the same experimental stress-strain curve from uniaxial loading. Therefore, these elastic parameters should be interpreted as effective continuum properties of the fibrous network rather than as the intrinsic mechanical properties of individual cellulose fibers. Consequently, they implicitly account for the influence of network porosity, inter-fiber bond compliance, and other microstructural effects that are not explicitly resolved within the homogenized formulation.
For the orthotropic model with anisotropic damage evolution, we set $E_x = 4.4$ GPa and $E_y = 2.4$ GPa corresponding to the elastic modulus of paper in the MD and in the CD directions, respectively; $\nu = 0.25$, and $G = \sqrt{E_x E_y}/[2(1+\nu)]$. The value of $\nu = 0.25$ is not far from 0.293, a value reported in [90] and obtained from experimental tests on paper under different relative humidity and paper quality.
The coefficients of the constitutive tensor, and in particular $C^*(\mu_\alpha)$ in position (1,1) relevant for the uniaxial tensile tests, are automatically derived by the application of the rotation matrices corresponding to each test case characterized by a different value of μ_α from 0 to $\pi/2$ according to Eq.(3.19a). The identified damage model parameters are collected in Tab. 6. The variation of strain ϵ_y may be attributed to the shear strain acting on the fiber lateral surface caused by friction, since the shear component

promotes yielding in the J2 plastic model. The role of friction is expected to become even more important in case of low density fibrous materials like those produced by electrospinning, demanding for further research in this direction. While ϵ_y has a random trend around an average value of $\epsilon_y^{\text{avg}} = 0.0056$, all the dependencies of the other parameters upon $\overline{\phi}$ are well approximated by linear relations:

$$E(\overline{\phi}) = -1.274\,\overline{\phi} + 4.40, \tag{3.31a}$$

$$a(\overline{\phi}) = -0.382\,\overline{\phi} + 1.80, \tag{3.31b}$$

$$n(\overline{\phi}) = -0.089\,\overline{\phi} + 1.25. \tag{3.31c}$$

	$\overline{\phi} = 0$	$\pi/12$	$\pi/6$	$\pi/4$	$\pi/3$	$5\pi/12$	$\pi/2$
ϵ_y $(-)$	0.0068	0.0066	0.0053	0.0053	0.0048	0.0045	0.0058
a	1.8	1.7	1.6	1.5	1.4	1.3	1.2
n	1.25	1.23	1.20	1.18	1.16	1.13	1.11
E (GPa)	4.4	4.07	3.73	3.40	3.07	2.73	2.40

Table 6: Identified parameters for the orthotropic model with anisotropic damage (first three rows), plus the value of $E(\overline{\phi})$ used for the isotropic model with anisotropic damage.

The predictions of the two continuum models and the experimental results are compared in Fig. 24. Simulations have been stopped in correspondence of the onset of material failure $d \sim 1$. The agreement of both models is pretty good, and the simplified model demonstrates that the introduced assumptions do not compromise the accuracy of the simulations.

Focusing on the linear elastic regime, we compare the three models in terms of elastic stiffness $C^*_{1,1}$ for different values of $\overline{\phi}$ in Fig. 25. Experimental data are also shown with dots and correspond to the tangent elastic moduli determined from Fig. 21(a) and graphically shown in Fig. 21(b). The micro-scale model, using the values ρ_c, $K = E_f A$, and $d_{\max}$ identified from images and literature, leads to the blue curve which slightly overestimates the experimental data. Its variability with respect to $\overline{\phi}$ is a straightforward result of the term $\cos^2(\overline{\phi})$ of the formulation. The orthotropic macro-scale continuum model with anisotropic damage, using $C^*_{1,1} = 4.4$ GPa for the elastic modulus in the MD direction ($\overline{\phi} = 0$)

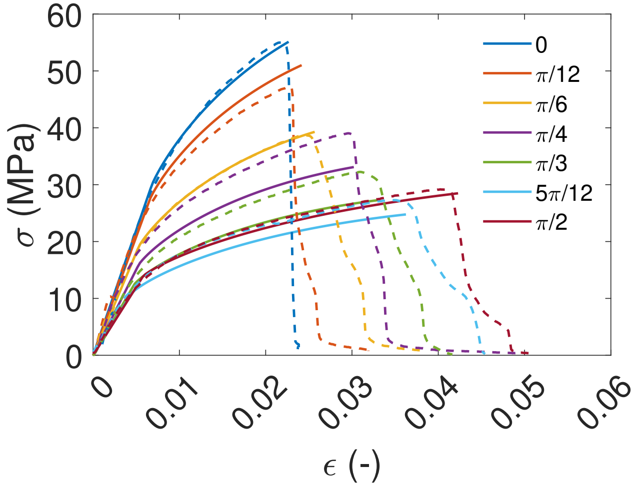

(a) Orthotropic model with anisotropic damage

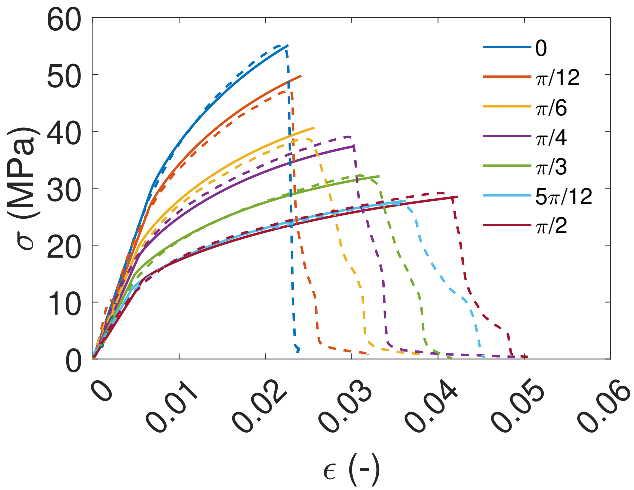

(b) Isotropic model with anisotropic damage

Figure 24: Comparison between experimental results (dashed lines) and predictions by the macro-scale continuum models (solid lines).

and $C^*_{2,2} = 2.4$ GPa for the elastic modulus in the CD direction ($\overline{\phi} = \pi/2$), leads to the black curve in Fig. 25. The intermediate values of $C^*_{11}(\overline{\phi})$ for $0 < \overline{\phi} < \pi/2$ are given as a straightforward result of the application of the rotation matrices $\mathbf{R}$. For the isotropic continuum model with the anisotropic damage law, a linear dependence between $C^*_{11}(\overline{\phi}) = E(\overline{\phi})$ and $\overline{\phi}$ has been found optimal in an average sense, see the red line in Fig. 25.

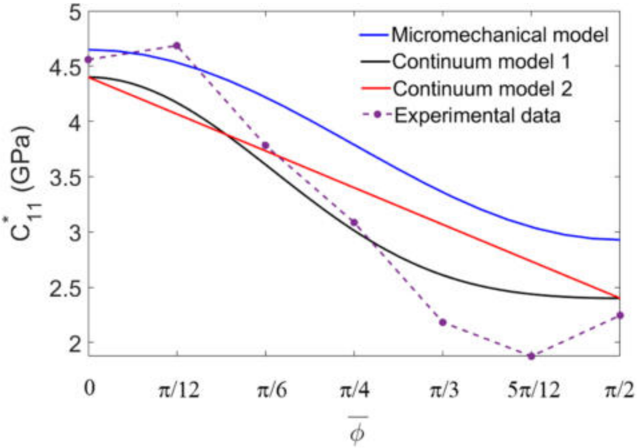

Figure 25: Comparison of $C^*_{11}(\overline{\phi})$ vs. $\overline{\phi}$ for the three models with experiments.

To exploit the macro-scale continuum models in conjunction with the micro-scale statistical approach with the aim to acquire additional information on the statistics of fiber failure at any point of the domain, the following procedure has to be executed. Considering a paper domain with a distribution of fibers with an average angle μ_α, the boundary value problem is solved according to one of the continuum models that determine, for each point of the domain, the displacement field and the strain field. The maximum principal strain ϵ_1 and its direction β are then computed from the strain field. Using these values, the statistical micromechanics model whose parameters have been identified in this section is called to compute the statistics of fibers failure. This can be done even for the points of interest in the material, where ϵ_1 is high and the micromechanical model can provide detailed information on the fibers response that is not provided by the continuum approach.

3.2 Models validation for biaxial plane stress states

With the above models available, we proceed to analyze problems subject to biaxial plane stress states. The continuum formulations have been implemented within the FreeFem++ software [91], discretizing the continuum with quadratic triangular elements. No mesh dependencies have been identified in the simulations carried out up to the peak loads.
For this purpose, we considered paper samples made of the same material as in Sec. 3.1.3 and perforated by an eccentric hole of diameter $D = 5.4$ mm, 9.8 mm distant from the left boundary, see the sketch in Fig. 26. The samples have been cut from a paper sheet under three different inclinations $\mu_\alpha = 0$, $\mu_\alpha = \pi/4$ and $\mu_\alpha = \pi/2$. The boundary conditions are an imposed displacement u increasing from zero up to failure with a loading rate of 0.5 mm/min. In this case, the principal strain ϵ_1 is no longer uniform and changes from point to point, especially in proximity of the circular hole, that is, $\overline{\phi}(x, y) = \mu_\alpha - \beta(x, y)$.
The numerical predictions of the continuum models (solid lines) are compared with the experimental results (dashed lines) in Fig. 27. The linear elastic part of the force-displacement curves is well predicted. The models are also able to capture the maximum load. After that, simulations present a drop caused by the progressive vanishing stiffness of finite elements. The isotropic model with an effective elastic modulus linear function of $\overline{\phi}$ returns to be very accurate.
The contour plots of the maximum principal strain are shown in Fig.28 in correspondence to the maximum loads in Fig.27, just before the onset of failure. The photos of the specimens at failure are shown in the same figure to the right panels. The maximum values of ϵ_1 in the contour plots correspond to the three values of $\epsilon_1(\overline{\phi})$ that lead to the critical condition $d \cong 1$ for the examined cases.
To further validate the model, we conducted another set of tensile tests on

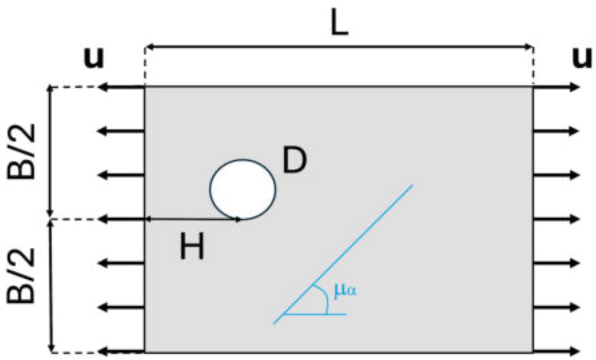

Figure 26: Schematic representation of paper samples with an eccentric hole. The fibrous cellulose network has a mean orientation μ_α defined as in the sketch.

paper samples with a semi-circular hole on the edge of diameter $D = 5.4$ mm, see the sketch in Fig. 29. These samples have been also tested considering three different fiber orientation angles, $\mu_\alpha = 0$, $\mu_\alpha = \pi/4$ and $\mu_\alpha = \pi/2$, under the same loading conditions as in the previous example. Figure 30 shows the comparison between the numerical predictions of the two continuum models (solid lines) and the experimental results (dashed lines). As in the previous validation, both models capture the force-displacement curves and effectively predict the maximum load carrying capacity, again with the simplified isotropic model providing the most accurate predictions. The contour plots of the maximum principal strain ϵ_1 at the peak load predicted by the continuum models are shown in Fig. 31, along with the corresponding photos of specimens at failure.
The application of the statistical micromechanical model at the points subject to the maximum principal tensile strain leads to further information on the percentage of debonded and broken fibers in the RVE in the point that is not available from the continuum simulations and that are particularly interesting from the technical viewpoint.
Specifically, we found in the two test cases for $\mu_\alpha = 0$ that 25% of the fibers were debonded and 39% were broken; for $\mu_\alpha = \pi/4$, 38% of the

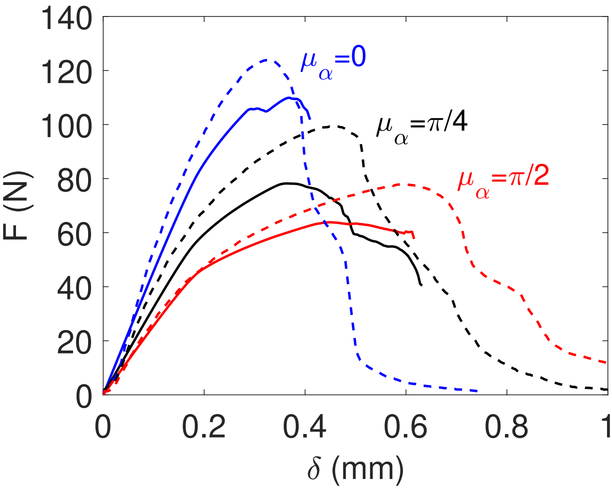

(a) Orthotropic model with anisotropic damage

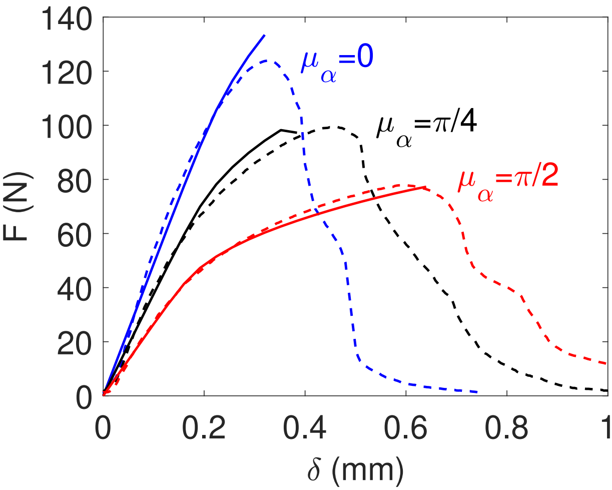

(b) Isotropic model with anisotropic damage

Figure 27: Force-displacement curve for the test in Fig.26. Solid curves refer to continuum models predictions and dashed curves to experimental results. Three angles μ_α have been tested.

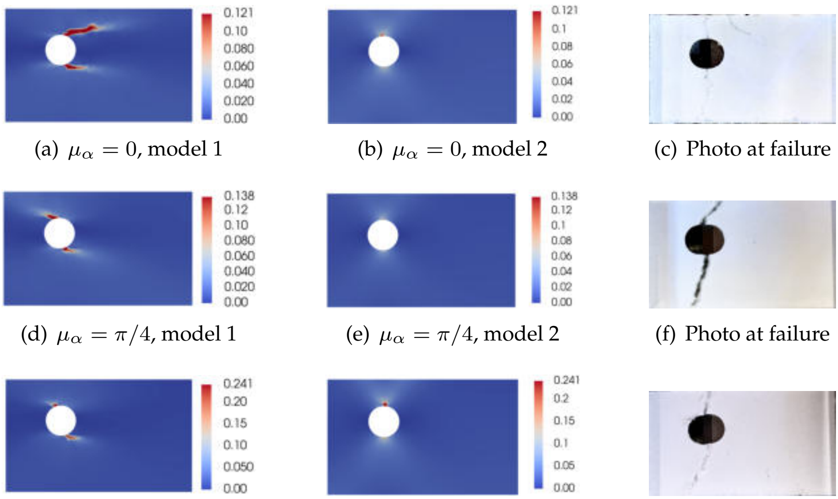

(a) $\mu_\alpha = 0$, model 1 (b) $\mu_\alpha = 0$, model 2 (c) Photo at failure

(d) $\mu_\alpha = \pi/4$, model 1 (e) $\mu_\alpha = \pi/4$, model 2 (f) Photo at failure

(g) $\mu_\alpha = \pi/2$, model 1 (h) $\mu_\alpha = \pi/2$, model 2 (i) Photo at failure

Figure 28: Contour plots of the maximum principal strain ϵ_1 at the maximum load, for the three samples tested under different ϕ and for the two continuum models (model 1: orthotropic model with anisotropic damage; model 2: isotropic model with anisotropic damage. The maximum value of ϵ_1 in each plot corresponds to the critical value for $d \cong 1$ in each case.

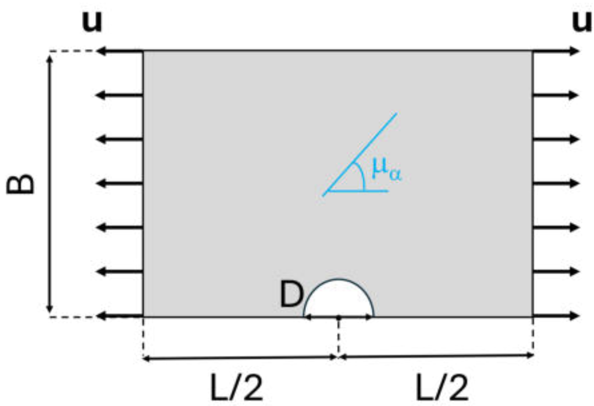

Figure 29: Schematic representation of paper samples with an external hole. The fibrous cellulose network has a mean orientation μ_α defined as in the sketch.

fibers were debonded, and 21% were broken; for $\mu_\alpha = \pi/2$, 36% of the fibers were debonded, and 9% were broken. These results indicate that, for $\mu_\alpha = 0$, the fibers in the RVE are almost aligned with the loading direction and experience the highest strain at each loading step, substantially increasing the number of broken fibers as compared to the other values of μ_α. Moreover, as a result of the machine pressure applied in the same direction during the papermaking process, the fiber bonds are stronger than in the other directions and the ratio between broken fibers and debonded ones is the highest. The opposite trend occurs for $\mu_\alpha = \pi/2$, where the bonds are inherently weaker due to the manufacturing process and the highest percentage of debonded fibers is observed. Macroscopically, this leads to two completely different mechanical responses terms of force-displacement diagrams: the case with $\mu_\alpha = 0$ presents a lower deviation from linearity and then a sudden catastrophic failure at the peak load, with a sharp drop in the load carrying capacity due to extensive fiber breakage. The case with $\mu_\alpha = \pi/2$ shows a progressive stiffness degradation caused by progressive fibers debonding and a smoother post-peak

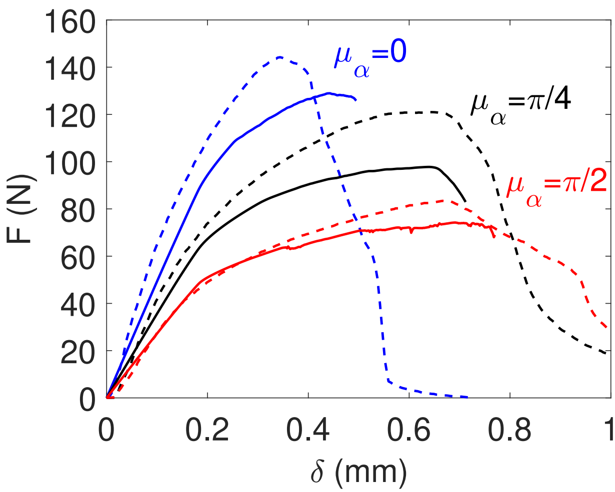

(a) Orthotropic model with anisotropic damage

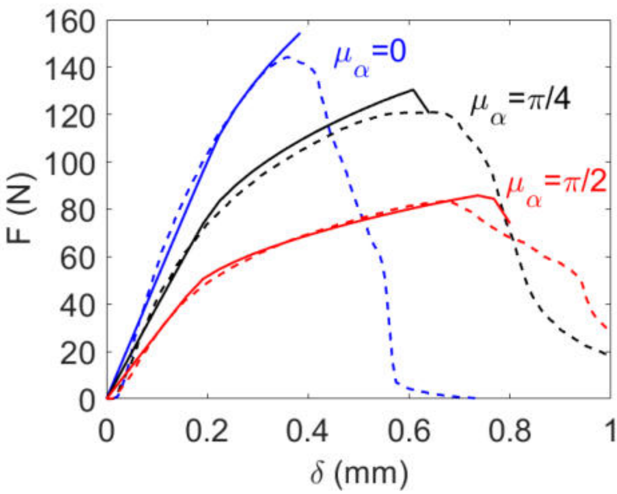

(b) Isotropic model with anisotropic damage

Figure 30: Force-displacement curve for the test in Fig. 29. Solid curves refer to continuum models predictions and dashed curves to experimental results. Three angles μ_α have been tested.

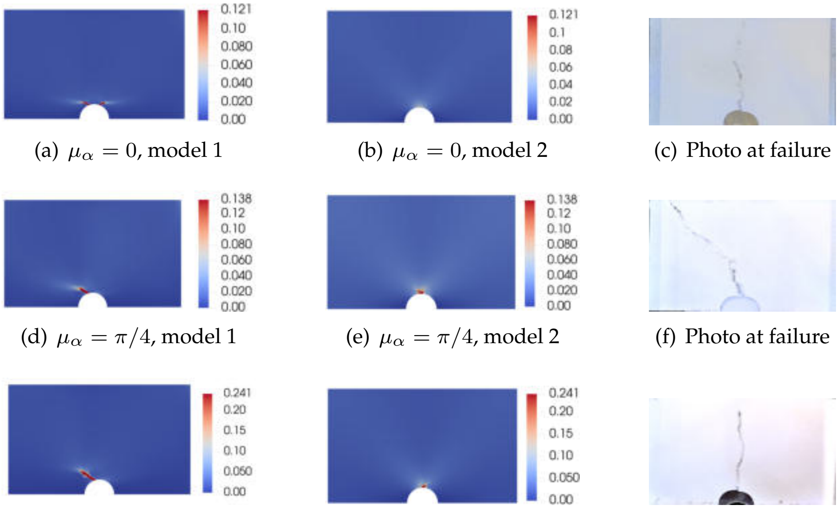

(a) $\mu_\alpha = 0$, model 1 (b) $\mu_\alpha = 0$, model 2 (c) Photo at failure

(d) $\mu_\alpha = \pi/4$, model 1 (e) $\mu_\alpha = \pi/4$, model 2 (f) Photo at failure

(g) $\mu_\alpha = \pi/2$, model 1 (h) $\mu_\alpha = \pi/2$, model 2 (i) Photo at failure

Figure 31: Contour plots of the maximum principal strain ϵ_1 at the maximum load, for the three samples tested under different ϕ and for the two continuum models (model 1: orthotropic model with anisotropic damage; model 2: isotropic model with anisotropic damage. The maximum value of ϵ_1 in each plot corresponds to the critical value for $d \cong 1$ in each case.

branch. These findings highlight that fiber breakage dominates the failure mechanisms for $\mu_\alpha = 0$, while the wider stiffness degradation is primarily due to fibers debonding for $\mu_\alpha = \pi/2$.

Chapter 4

Modeling and experiments of filament-reinforced paper for sustainable packaging

4.1 Reinforced gummed paper and its microstructure

Despite the growing industrial use of reinforced gummed papers, their mechanical behavior remains poorly understood, particularly due to its complex internal composition. In this section, we investigate the internal structure of gummed paper using microscopic imaging, and we characterize its mechanical response through uniaxial tensile tests, aiming to provide insight into the underlying mechanisms governing its performance.

To investigate the role of the reinforcing filaments, two square samples with side length $\delta = 10$ mm were cut from the same reinforced gummed paper material: sample 1 from a region composed solely of the cellulose paper layers without reinforcement; sample 2 from a region containing the embedded reinforcement, see Fig. 32. This approach enables a direct comparison of the mechanical response with and without the contribution of the fiberglass filaments.

To investigate the role of the reinforcing filaments, two types of specimens were extracted from a commercial reinforced gummed paper. Rectangular specimens of length 30 mm and base 10 mm were cut manually using a sharp precision cutter to avoid damaging the embedded filaments or disturbing the layered structure of the material. Samples were then placed within a DEBEN tensile stage, clamping 10 mm of paper on both sides, providing a free span $\delta = 10$ mm for each sample, see Fig. 32.
The specimens were extracted from the same sheet but from different regions: specimen 1 is related to a region composed solely of the cellulose paper layers without reinforcement, while the specimen 2 is extracted from a region containing the embedded reinforcement, perfectly aligned in the middle of the specimen. Three replicas were considered for each type of specimen. This enables a direct comparison of the mechanical response of gummed paper with and without the contribution of the fiberglass filament.

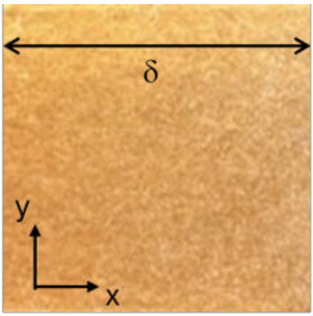

(a) Sample 1

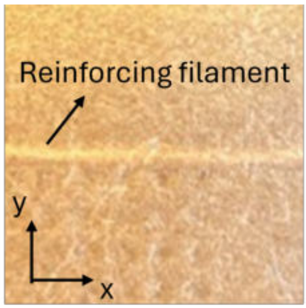

(b) Sample 2

Figure 32: Reinforced gummed paper specimens. (a) Region without reinforcing filaments, consisting only of cellulose layers; (b) Region containing an embedded fiberglass filament between the cellulose strips, visible in the middle of the specimen.

To analyze the internal structure of the reinforced paper, confocal microscopy was employed to image both the through-thickness and in-plane surfaces of the sample containing the embedded fiber. The confocal microscopy observations were carried out using a Leica DCM3D confocal microscope at 10× magnification, available in the MUSAM-Lab. The microscopy image of the surface from a region of the sample containing reinforcing fibers, shown in Fig. 33(a), reveals only the network of cellulose fibers and the reinforcing filaments are not visible. In contrast, the cross-sectional view presented in Fig. 33(b) clearly shows the presence of a reinforcing filament embedded between the two cellulose paper strips, confirming the layered configuration of the material.

A single reinforcing filament used in reinforced gummed paper typically consists of a bundle of fiberglass fibers twisted together into a single thread. This structural detail is further confirmed by the surface topography of the sample's cross-section, acquired using the same Leica DCM3D under confocal profilometer mode shown in Fig. 34, where multiple fiberglass fibers are clearly identifiable by their circular cross-sections.

To quantify the impact of adding fiberglass filament to paper on the mechanical response, uniaxial tensile tests were performed on both samples using the micro-mechanical tensile stage DEBEN available in the MUSAM Laboratory at the IMT School for Advanced Studies Lucca. The tensile load was applied along the $x-$axis, corresponding to the direction in which the reinforcing fiberglass filament is embedded longitudinally in the material. The specimens were clamped on both sides, with a grip separation δ of 10 mm. The displacement loading rate was set to 0.1 mm/min, to obtain quasi-static conditions, and the force data were recorded directly from the loading cell of the equipment, for each imposed displacement. Those data can be then transformed into stress-strain curves by diving the force by the nominal cross-section area and the displacement by the initial free span, as is customary.

Figure 35 shows a comparison of the stress–strain responses of the two samples, highlighting the effect of the reinforcement. For each specimen type, three samples were tested. The blue curves correspond to the non-reinforced specimens, while the red curves represent the fiberglass-reinforced specimens; different line styles denote the individual samples tested for each specimen type.

The results for the filament-reinforced samples are highly consistent across

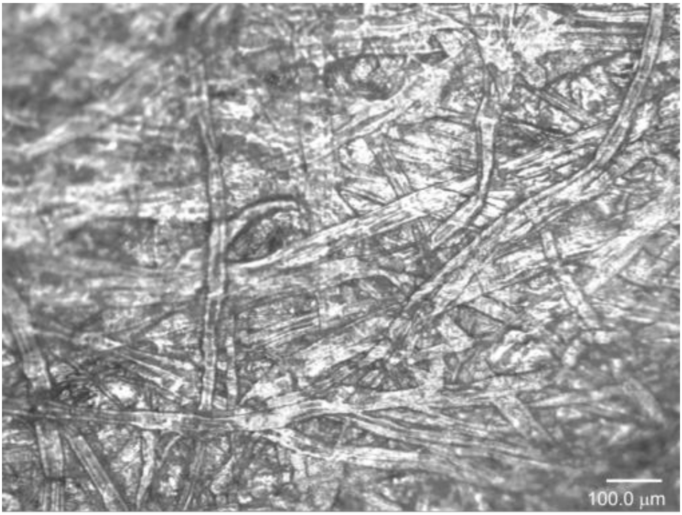

(a) In-plane view

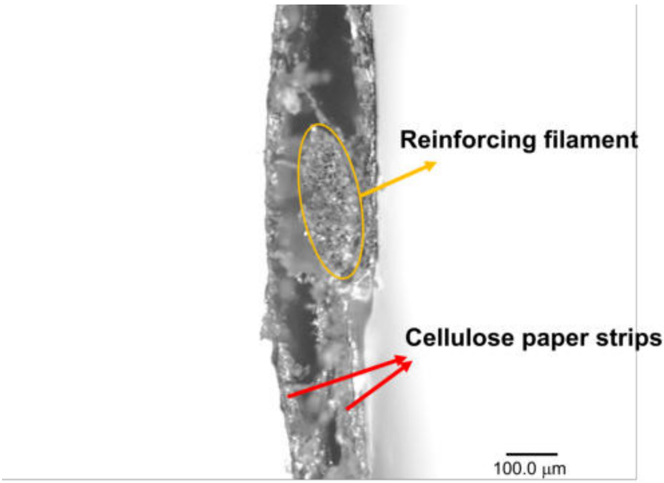

(b) Cross-sectional view

Figure 33: Confocal microscopy images of reinforced gummed paper (10× magnification). (a) In-plane surface showing the cellulose fiber network; (b) Through-thickness view revealing a reinforcing filament embedded between two cellulose layers.

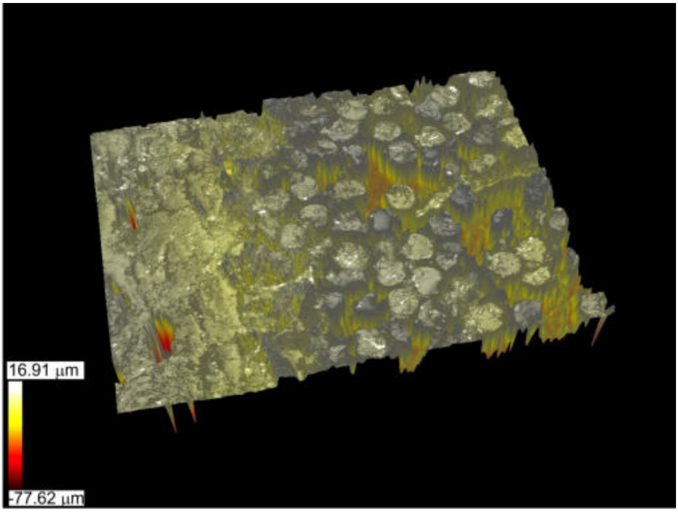

(a)

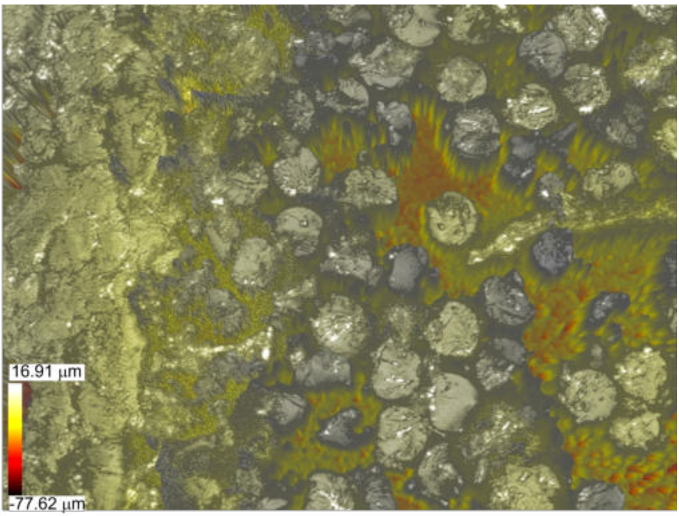

(b)

Figure 34: 3D surface topology of reinforced gummed paper. The image highlights the internal structure of the reinforcing filament, composed of multiple twisted fiberglass fibers with clearly visible circular cross-sections.

the three samples, whereas a slightly larger scatter is observed for the non-reinforced samples, especially in the post-peak branch. This difference can be attributed to the fact that the mechanical response of the reinforced samples is dominated by the fiberglass filament, while in the non-reinforced samples it is governed by the randomly distributed cellulose fibers. The presence of the fiberglass filament leads to a significant increase in the stiffness and in the ultimate tensile strength of the material. However, after the peak load, the sample without reinforcement exhibits a more brittle post-peak response, caused by the occurrence of a fast catastrophic failure triggered by the fiberglass failure.

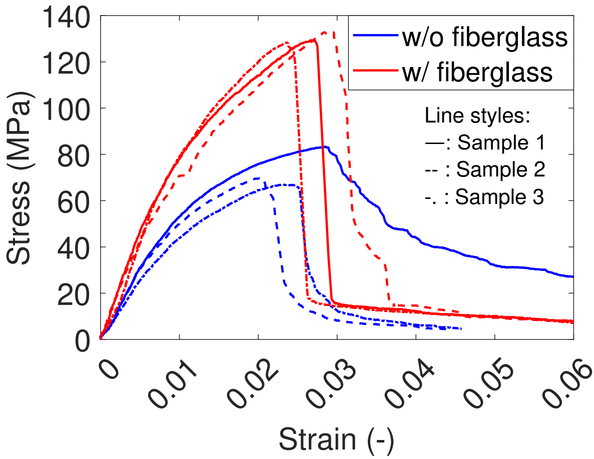

Figure 35: Stress–strain curves from uniaxial tensile tests: specimens without fiberglass reinforcement (blue); specimens with fiberglass reinforcement (red).

These results relate specifically to reinforced gummed paper incorporating fiberglass filaments, a synthetic form of reinforcement. However, this prompts an important question: *what if a more sustainable, natural fiber were used in place of fiberglass to reinforce the paper?* To shed light onto this issue, we extend the micro-mechanical model developed in [59, 85] to interpret the mechanical behavior of reinforced gummed paper, as detailed in the following section.

4.2 Stochastic network model

In this section, we extend the stochastic mechanics model developed in Chapter 2 to investigate the mechanical behavior of reinforced gummed paper materials by incorporating an additional population of fiberglass filaments. It should be noted that the proposed model adopts a reduced-order model representation in which the tensile response is governed by a representative cross-section of the material, and it does not explicitly resolve the spatial architecture of the fibrous network. Within this framework, load is assumed to be carried by fibers intersecting the cross-section, and failure is described through their statistical response. This assumption is physically justified under uniaxial tensile loading, where load paths are predominantly aligned and failure is often controlled by the weakest effective section. As such, the model provides a computationally efficient approximation that captures the dominant features of the tensile response relative to spatially resolved network simulations.

Reinforced gummed papers are manufactured by bonding together two strips of cellulose fiber networks with a set of reinforcing fibers, typically fiberglass filaments, embedded between them, see Fig. 33. This layered composite structure is assembled using heat-activated adhesives, resulting in a mechanically enhanced material suitable for sealing and packaging applications. A square sample made of size $\delta = 10$ mm and thickness $t = 0.1$ mm is considered, lying in the x–y plane of an orthogonal reference frame, see Fig. 32, in accordance with real samples. The fiber network in the plane is subjected to uniaxial tensile loading applied along the $x-$axis, inducing deformation in the constituent fibers based on their orientation and mechanical properties.

Each cellulose fiber is characterized by a randomly distributed orientation angle α_c, defined as the angle between the local fiber axis and the global $x-$axis. The method focuses on the potential cross-section in the $y-$direction, where the final sample failure occurs. Consequently, the total number of fibers intersecting this cross-section is given by:

$$N = N_c + N_r \tag{4.1}$$

where N_r denotes the number of reinforced fibers along the cross-section, e.g. fiberglass filaments for gummed paper, and N_c is the number of cellulose fibers which is defined as:

$$N_c = 2N_l N_f \tag{4.2}$$

where N_l is the number of layers in a single paper strip, and N_f is the average number of cellulose fibers of each layer that intersect the specimen cross-section. The coefficient 2 accounts for the presence of two paper strips bonded on either side of the reinforcement filaments in the reinforced gummed paper structure.

The value of N_f can be derived from the fiber density of each layer, ρ_c, defined as the number of fibers intersected by a straight cross-sectional line divided by its length, which can be experimentally obtained through microscopic imaging of the paper surface. This gives:

$$N_f = \rho_c B \tag{4.3}$$

where B is the width of the paper strips along the $y-$direction. The number of layers in a single paper strip is estimated by calculating how many fibers with maximum thickness, $t_{cf}^{\max}$, can be placed across the total thickness of the strip, $t_s = t/2$, which is:

$$N_l = \frac{t_s}{t_{cf}^{\max}} \tag{4.4}$$

On the other hand, the arrangement of reinforcing filaments in reinforced paper materials is typically longitudinal, aligned with the machine direction of the paper strips, in order to enhance tensile strength in that primary direction. However, in some configurations, additional filaments may be oriented diagonally or crossed in $X-$patterns, often at fixed angles such as $37°$, to improve multidirectional resistance and reduce the risk of failure under off-axis or eccentric loading conditions. In the modeling framework, each reinforcing filament is characterized by an orientation angle α_r, defined as the angle between the reinforcing filaments and the global $x-$axis.

The overall mechanical response of the reinforced paper results from the combined contribution of the cellulose fiber network and the reinforcing

filaments. As explained in the previous chapters, the constitutive response of cellulose fibers is governed by the underlying micromechanical mechanisms of fiber recruitment and failure. Accordingly, the constitutive response of the cellulose fibers, f_c, is computed using Eq. 3.5.
The axial strain in an individual cellulose fiber is obtained by projecting the macroscopic principal strain onto the fiber orientation direction. However, this local strain may be perturbed due to the failure of surrounding fibers. To account for this effect, a strain redistribution factor $r \in [0, 1]$ is introduced, representing the fraction of strain that is transferred to neighboring fibers. When a fiber fails, its strain is equally redistributed equally to its neighbors, thereby increasing their local strain and inducing a progressive strain localization in that point. The redistributed strain is denoted ϵ^{red}, and the total strain experienced by a given fiber is defined as:

$$\epsilon = (\epsilon_1 + \epsilon^{\text{red}}) \cos \alpha_c \tag{4.5}$$

It is important to remark that this formulation implies a load redistribution as well, since the fiber force is proportional to the fiber strain. Therefore, the model captures the strain localization effects due to progressive damage and local load transfer, which is a key mechanism in the failure evolution of disordered fiber networks.
As described in the previous chapters and detailed in [59], the recruitment and failure strains of cellulose fibers are governed by the free segment length between consecutive inter-fiber bonds. Accordingly, the recruitment strain, ϵ_c^r, and the failure strain, ϵ_c^f, are computed using Eqs. (3.9a) and (3.9b), respectively. These relations account for the influence of the network microstructure and the competing failure mechanisms of inter-fiber debonding and fiber breakage. Finally, the contribution of each cellulose fiber in the loading direction is obtained by projecting the axial fiber force onto the $x-$axis, as expressed in Eq. (3.7).
The reinforcing fibers used in reinforced paper structures are typically fiberglass filaments, which exhibit a significantly higher stiffness compared to cellulose fibers. Given that the macroscopic deformation of reinforced gummed papers under tensile loading is generally small, the mechanical behavior of the fiberglass reinforcement can be reasonably

modeled using a linear elastic constitutive law. Accordingly, under uniaxial tensile loading applied at the boundaries of the network, the axial force carried by an individual reinforcing filament crossing the cross-section and aligned at an angle α_r is given by:

$$f_r = \begin{cases} K_r\, \epsilon_1 \cos\alpha_r, & \text{if } \epsilon < \epsilon_r^f \\ 0, & \text{if } \epsilon \geq \epsilon_r^f \end{cases} \tag{4.6}$$

where we have assumed that the cross-section remains planar under deformation before catastrophic fracture. Therefore, the strain is the same for all the fibers within the linear elastic limit, above which strain localization takes place as a result of fracture. Here, K_r is the axial stiffness of the reinforcing filament defined as:

$$K_r = E_r A_r \tag{4.7}$$

where E_r denotes the Young's modulus of the reinforcing fibers and A_r is the total effective cross-sectional area of the filaments intersecting the loaded cross-section. To determine the total contribution of the reinforcing fibers to the macroscopic response, the axial forces carried by reinforcing filaments are projected onto the loading direction, i.e., the $x-$axis:

$$F_r = \begin{cases} K_r\, \epsilon_1 \cos^2\alpha_r, & \text{if } \epsilon < \epsilon_r^f \\ 0, & \text{if } \epsilon \geq \epsilon_r^f \end{cases} \tag{4.8}$$

In the present model, to predict the emergent response of the reinforced paper, we examine a configuration that could be adopted in future specialized qualification standard tests that, according to the authors' best knowledge, they have not yet been proposed for reinforced paper. The specimen is such that the reinforcing filament(s) are distributed symmetrically with respect to the barycenter of the specimen cross-section, such that rotational equilibrium of moments is automatically satisfied when a uniaxial tension state is applied via an imposed axial displacement at the clamped edges. Under this assumption, the axial equilibrium of the specimen leads to an expression for the macroscopic stress σ which is given by the mechanical contribution of the reinforcing filaments superimposed on that of the cellulose network response:

$$
\begin{aligned}
\sigma = \frac{N_c}{Bt} \int_{r=0}^{1} \int_{\alpha_c=-\pi/2}^{\pi/2} \int_{\lambda=\lambda_{\min}}^{\lambda_{\max}} F_c \, p(\alpha_c, \lambda, r) \, \mathrm{d}\alpha_c \, \mathrm{d}\lambda \, \mathrm{d}r \\
+ \frac{1}{Bt} \sum_{m=1}^{N_r} F_{r_m} \delta(y - y_r^m)
\end{aligned}
\tag{4.9}
$$

where the first term is related to the emergent response of cellulose fibers, including redistribution effects, and the second term corresponds to the contribution of the reinforcing filaments that are concentrated in space at coordinates y_r^m and thus their distributions are Dirac delta functions, $\delta(y - y_r^m)$, both divided by the nominal cross-section area Bt.
The function $p(\alpha, \lambda, r)$ in the term related to the fiber network response represents the joint probability density function (PDF) that describes the likelihood of encountering a cellulose fiber in the network with a given orientation angle α_c, free segment length λ, and redistribution factor r. This joint distribution plays a central role in the micromechanical model, as it captures the inherent heterogeneity and randomness of the cellulose fiber network. Assuming that the redistribution factor r is uniformly distributed across the cellulose network and independent of both fiber orientation and segment length, and that α_c and λ are also statistically independent, the joint PDF can be factorized as:

$$
p(\alpha_c, \lambda, r) = p_{\alpha_c}(\alpha_c) \, p_\lambda(\lambda) \, p(r) \tag{4.10}
$$

where $p(r)$ implicitly depend upon the deformation of the population of cellulose fibers. In the linear regime, before strain redistribution, $r = 0$ everywhere and $p(r) = 1$. The probability density $p_{\alpha_c}(\alpha_c)$ represents the marginal probability density function associated with the fiber orientation angle α_c, and is computed using Eq. (3.11). Similarly, $p_\lambda(\lambda)$ denotes the marginal probability density function associated with the free segment length λ obtained from Eq. (3.12).
The integrals in Eq.(4.9) cannot be solved in closed form due to the nonlinear dependency of the cellulose fibers' contributions on the deformation process. For its solution, a discrete formation proposed in [59] is herein

pursued, in which the integrals are replaced by discrete summations over a randomly generated fiber network.

In this formulation, a population of cellulose fibers indexed by (i, j), where $j = 1, \ldots, N_f$ denotes the fiber number within a single layer and $i = 1, \ldots, N_l$ denotes the layer index through the thickness, is randomly generated, with each fiber assigned geometrical properties, $\alpha_{c_{i,j}}$ and $\lambda_{i,j}$, drawn from the prescribed probability distributions. A uniform macroscopic strain ϵ_1 is applied in $N_s = 100$ incremental loading steps, following a linear ramp. The strain experienced by each fiber at the n^{th} loading step is computed as:

$$\epsilon_{i,j} = \frac{n}{N_s}\epsilon_1 + \epsilon_{i,j}^{\text{red}}, \tag{4.11}$$

where $\epsilon_{i,j}^{\text{red}}$ represents the redistributed strain received by the $(i, j)^{th}$ fiber due to the failure of its neighboring fibers at the n^{th} loading step. One could consider a general model where redistribution is affecting all the neighboring fibers within a distance d_n from the failed one, where d_n would physically represent an internal length scale for nonlocal effects. While such a distance is certainly function of the degree of cross-linking and material density –higher cross-linking or material density are expected to induce a wider spatial redistribution–, for conventional industrial paper the authors had excellent results by considering an internal length scale corresponding to $d_n = 2/\rho_c$, which includes only the two closest adjacent fibers to the failed one in the redistribution process. Under these conditions, the redistributed strain is:

$$\epsilon_{i,j}^{\text{red}} = \frac{r}{2}\left(L_{i,j-1}\,\epsilon_{c_{i,j-1}}^{f} + L_{i,j+1}\,\epsilon_{c_{i,j+1}}^{f}\right) \tag{4.12}$$

where $r \in [0, 1]$ is the redistribution factor, $\epsilon_{c_{i,j-1}}^{f}$ and $\epsilon_{c_{i,j+1}}^{f}$ are the failure strains of the neighboring fibers $(i, j-1)$ and $(i, j+1)$, respectively, as defined in Eq. (3.9b). The function $L_{i,j}$ is a logical labeling operator that identifies the failure status of the $(i, j)^{th}$ fiber under the applied load at the $(n-1)^{th}$ loading step:

$$L_{i,j} = \begin{cases} 0, & \text{not failed} \\ 1, & \text{failed} \end{cases} \tag{4.13}$$

Therefore, the average macroscopic stress in Eq. (4.9) can be expressed in discrete form as:

$$
\begin{aligned}
\sigma &= \frac{1}{Bt}\sum_{n=1}^{N_s}\left(\sum_{i=1}^{N_l}\sum_{j=1}^{N_f} F_{c_{i,j}} + \sum_{m=1}^{N_r} F_{r_m}\right) \\
&= \frac{1}{Bt}\sum_{n=1}^{N_s}\left[\sum_{i=1}^{N_l}\sum_{j=1}^{N_f} K_c\left(\frac{n}{N_s}\epsilon_1 + \epsilon_{i,j}^{\text{red}}\right)\cos^2\alpha_{c_{i,j}} + \sum_{m=1}^{N_r} K_r\frac{n}{N_s}\epsilon_1\cos^2\alpha_{r_m}\right]
\end{aligned}
\tag{4.14}
$$

This discrete formulation provides a comprehensive framework for modeling the mechanical response of reinforced paper networks by explicitly accounting for the statistical variability in fiber orientation and cross-linking, as well as the key micromechanical mechanisms of recruitment, failure, and post-failure load redistribution.

4.3 Material characterization and model validation

In this section, we begin by identifying the model parameters for sample 1, which consists solely of cellulose paper strips without reinforcing filaments. These parameters are calibrated by validating the model against the corresponding uniaxial tensile test results. Once validated, the same set of parameters, representing the intrinsic mechanical behavior of the cellulose fiber strips, is employed in the modeling of sample 2, which additionally incorporates the mechanical contribution of the embedded reinforcing filament. The extended model is then verified against the experimental response of sample 2 and subsequently used to investigate the influence of reinforcement with alternative natural fibers, offering a theoretical framework to support the design of more sustainable reinforcements than synthetic materials such as fiberglass.

To construct the fiber network for sample 1, two strips of cellulose paper are modeled, each composed of N_l layers with N_f fibers per each layer. In this regard, morphological parameters were extracted from confocal microscopy performed on sample 1. The key parameters include the fiber density per layer ρ_c, and the minimum, average, and maximum free segment lengths, denoted as $\lambda_{\min}$, λ_{avg}, $\lambda_{\max}$, respectively. These parameters are defined for sample 1 in the same manner as those previously introduced for other paper materials in [59], and their numerical values are reported in Tab. 7. Additional geometrical parameters were obtained from the literature, including the average cellulose fiber cross-sectional area $A_c = 237\ \mu\text{m}^2$ and the maximum fiber thickness $t_{cf}^{\max} = 12.5\ \mu\text{m}$ [32].

Parameter	Value
ρ_c (fibers/mm)	35.6
d_n (μm)	56
λ_{min} (μm)	6.2
λ_{avg} (μm)	37
λ_{max} (μm)	187
ϵ_c^r	0.002
ϵ^d	0.165
ϵ^b	0.32
E_c (GPa)	24

Table 7: Identified model parameters for sample 1 (w/o fiberglass).

Using this set of parameters, the cellulose fiber network is constructed with $2 \times N_l = 0.1/0.0125 = 8$ cellulose layers, containing $N_f = 35.6 \times 10 = 365$ fibers each. A random orientation angle $\alpha_{c_{i,j}}$, sampled from a Gaussian distribution centered at $\mu_{\alpha_c} = 0$, which corresponds to alignment along the machine direction, is assigned to each fiber. Additionally, a free segment length $\lambda_{i,j}$, randomly sampled from an exponential distribution as described in Eq. (3.12), is also assigned to each fiber. It should be recalled that the indices i and j refer to the j^{th} fiber placed in the i^{th} layer of the network.

The mechanical parameters, namely the recruitment strain ϵ_c^r, the debonding strain ϵ^d, the breakage strain ϵ^b, and the Young's modulus of cellulose fibers E_c are identified by calibrating the model to match the experimental stress vs. strain response of sample 1. The calibrated values of these parameters are reported in Tab. 7. The methodology for linking each of these parameters to specific features of the experimental curve (e.g., initial stiffness, onset of nonlinearity, and failure point) follows the procedure described in detail in [59].

With the model parameters so identified, the stress–strain response of the cellulose fiber network is predicted by evaluating the first term in Eq. (4.14), which corresponds to the mechanical contribution of the cellulose network alone, without reinforcement. Figure 36 compares the experimental mechanical response of sample 1 with the corresponding model predictions for different values of the redistribution factor r. The effect of r was investigated to account for the possible mechanical contribution of the adhesive layer located between the two cellulose paper strips. The parametric analysis shows that variations of r do influence the predicted tensile response, particularly in the post-peak regime, as illustrated in Fig. 36. However, comparison with the experimental results indicates that satisfactory agreement is obtained for relatively low values of r.

This observation suggests that, under the present uniaxial tensile loading conditions, the adhesive layer has a limited influence on the dominant deformation and damage mechanisms governing the cellulose network response. Nevertheless, the role of r could become more relevant under other loading conditions, particularly those involving interfacial debonding, or out-of-plane deformation. In the present study, however, we focus solely on in-plane uniaxial tension, and such effects are not considered and left for further research.

To evaluate the mechanical response of sample 2 under uniaxial tensile loading using the proposed model, the cellulose fiber network is constructed using the validated parameters identified for sample 1, as reported in Tab. 7. In addition to the cellulose network, sample 2 contains a single fiberglass filament aligned along the machine direction and located approximately in the mid-plane of the specimen. This configuration results in $N_r = 1$ and an orientation angle of $\alpha_r = 0°$.

The geometrical parameter related to the cross-sectional area of the fiberglass filament, denoted by A_r, was identified through confocal microscopy and subsequent image analysis using ImageJ software. As shown in Fig. 37, this analysis yielded an effective filament cross-sectional area of $A_r = 0.022\ \mathrm{mm}^2$.

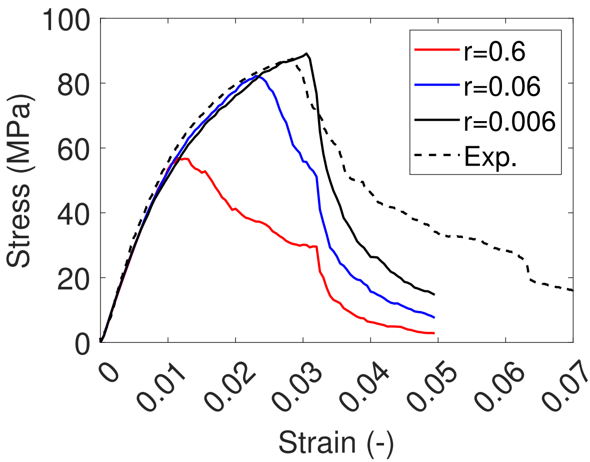

Figure 36: Comparison between the experimental stress–strain response of sample 1 (w/o fiberglass) and model predictions for different values of the redistribution factor r

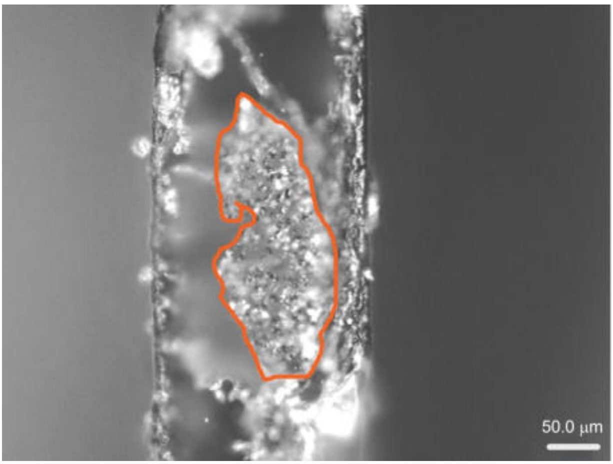

Figure 37: Confocal microscopy image of the reinforced paper cross-section of sample 2, analyzed with ImageJ software to determine the cross-sectional area of the fiberglass filament (within the orange curve).

To model the mechanical behavior of the reinforcing fiberglass filament, its Young's modulus and failure strain are required. The classification and mechanical properties of various types of glass fibers have been studied in [92]. For reinforced paper used in packaging applications, the fiberglass must not only offer high mechanical strength and water resistance, but also be environmentally friendly. Based on these criteria, this study adopts the mechanical properties of ECR-glass fiber, which is highlighted in [92] for being a more sustainable alternative to conventional glass fibers. Accordingly, we used a Young's modulus of $E_r = 80$ GPa and a failure strain of $\epsilon_r^f = 0.043$ for the fiberglass filament in our model to simulate the response of sample 2, which includes the embedded reinforcement.

The predicted stress–strain response of sample 2, represented by the red solid line in Fig. 38, shows excellent agreement with the experimental data (black dashed line) up to the peak load. This result highlights the robustness of the proposed model: by using the same calibrated cellulose fiber properties identified from sample 1 and superimposing the mechanical contribution of the fiberglass filament, the model successfully captures the composite behavior of the reinforced paper under uniaxial tension. However, a discrepancy is observed in the post-peak regime, where the experimental response softens more rapidly than the model prediction.

To better capture this behavior, a reduced strain at failure of the fiberglass, $\epsilon_r^f = 0.032$, was considered in the model. As shown in Fig. 38 by the blue line, this adjustment leads to improved agreement with the experimental curve beyond the peak, accurately reflecting the observed post-failure response. It should be emphasized that this reduced failure strain is introduced here as an effective modeling parameter to represent the observed composite response, rather than as a directly validated material property or a mechanistically derived degradation model, which might include additional microscopical failure mechanisms herein lumped into a single mesoscopic failure strain parameter.

This difference in the effective failure strain of the fiberglass filament may be attributed to the thermal effects introduced during the manufacturing process. Specifically, during the production of reinforced gummed paper, the cellulose strips and fiberglass filament are hot-glued together at approximately 70°C. This elevated temperature may have altered the mechanical properties of the fiberglass, particularly reducing its ultimate elongation from the 4.3% to approximately 3.2%.

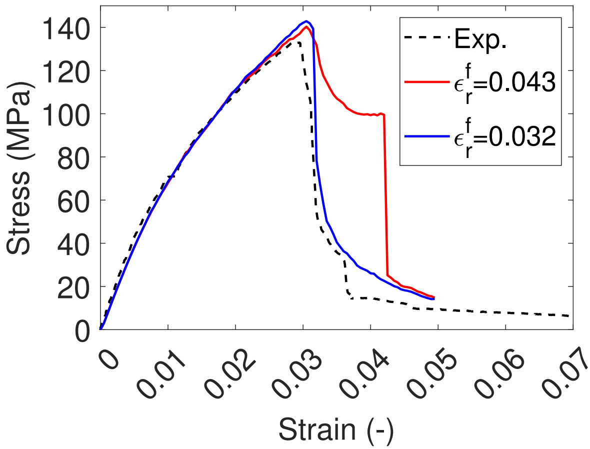

Figure 38: Comparison of experimental and modeled stress–strain curves for the sample 2 (w/ fiberglass), highlighting improved post-peak accuracy using a reduced failure strain, $\epsilon_r^f = 0.032$.

The confocal image of the cross-section where fracture takes place, showing the bridging action exerted by the fiberglass, can be appreciated in Fig. 39.

4.4 An insight into reinforced paper with natural fibers

Natural fiber composites (NFCs), primarily composed of cellulose-based fibers, have attracted renewed attention in the engineering and materials science communities due to their compelling combination of mechanical performance, sustainability, and economic viability. Natural fibers such as hemp, flax, and kenaf offer several advantages over conventional synthetic reinforcements like fiberglass. These include lower density

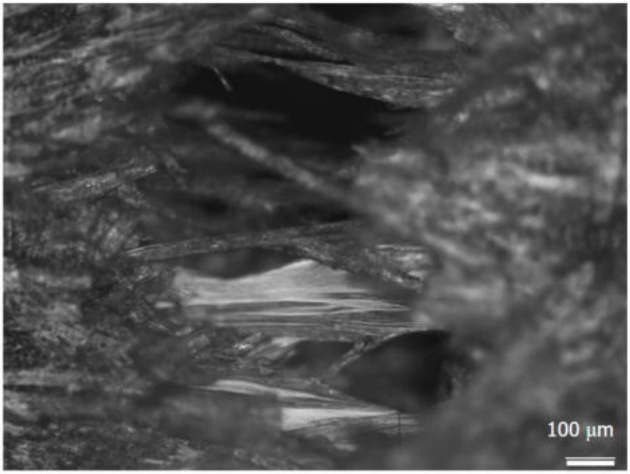

Figure 39: Confocal image of the cross-section where fracture takes place. The fiberglass is of white color.

(approximately half that of fiberglass), high specific strength and stiffness, rapid renewability, and significantly reduced environmental impact [93]. Coupled with their lower cost and biodegradability, these characteristics make natural fibers especially suitable for sustainable packaging applications, such as reinforced gummed papers, where lightweight and environmentally friendly materials are increasingly prioritized.
Despite their potential, the integration of natural fibers into reinforced paper products remains largely unexplored, and the present simulation method could offer support for innovative design.
To identify the most suitable natural fiber alternative to fiberglass in reinforced paper materials, we employed the proposed statistical mechanics model to predict the mechanical response of reinforced gummed papers incorporating various natural fibers. Figure 40 shows the predicted stress-strain curves for reinforced gummed paper samples incorporating hemp, kenaf, or two different types of flax fibers, in comparison with the reference sample reinforced with fiberglass. These simulations were performed using the proposed model validated against experimental results, chang-

ing only the mechanical properties of the reinforcing filament. For that, the fibers' model parameters have been taken from [94] where uniaxial tensile tests on single fibers have been conducted, and are summarized in Tab. 8.

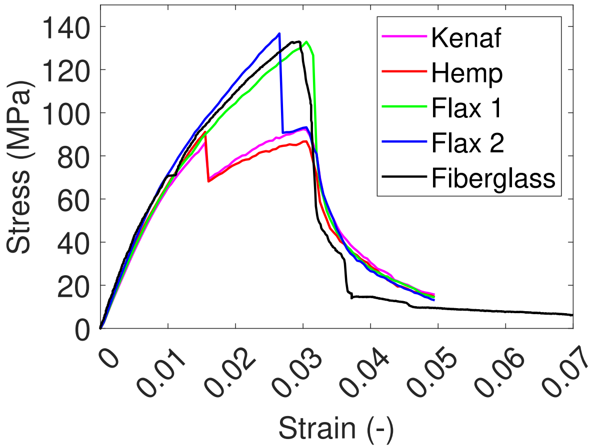

Figure 40: Predicted stress–strain responses of reinforced gummed paper with hemp, kenaf, flax 1, and flax 2 fibers, compared to the fiberglass-reinforced reference, sample 2.

Fiber	ϵ_r^f	E_r (GPa)
Kenaf	0.016	53
Hemp	0.016	70
Flax 1	0.032	60
Flax 2	0.027	80

Table 8: Mechanical parameters of natural fibers, from [94].

The simulations suggest that flax fibers, particularly flax 2, exhibit a mechanical performance very close to that of fiberglass. Both flax variants enhance stiffness and peak load as compared to hemp and kenaf, indicating that flax could serve as a viable natural replacement for synthetic fibers in terms of load-bearing capacity. Flax 1 demonstrates a more

progressive post-peak failure, while flax 2 achieves a slightly higher maximum force followed by an abrupt drop, highlighting the sensitivity of the mechanical response to the breakage strain of the reinforcing fiber. Hemp and kenaf show lower peak forces and stiffness but still provide substantial reinforcement relative to the baseline unreinforced paper.
The load drop observed after the first peak in the kenaf and hemp curves corresponds to the onset of reinforcement failure. In these cases, the reinforcing filament reaches its critical strain before complete failure of the surrounding cellulose network. Consequently, the filament abruptly loses its load-carrying contribution, leading to a temporary decrease in the global tensile force. Following this initial damage event, the applied load is progressively redistributed within the remaining cellulose network, which continues to deform and sustain part of the applied load.
It is important to emphasize that these results should be interpreted as a parametric mechanical feasibility study, in which only the intrinsic mechanical properties of the reinforcing fibers have been varied. The present model does not account for additional factors that may influence the actual performance of papers reinforced with natural fiber filaments, including processing-induced damage to the fibers, moisture sensitivity, and the quality of the fiber–paper interface. From a broader perspective, natural fibers offer well-established advantages in terms of lower environmental impact, renewability, and reduced cost compared to synthetic fibers such as fiberglass. These aspects further motivate the exploration of natural fiber reinforcements. Therefore, while flax appears to be a mechanically promising candidate, as well as attractive from sustainability and cost perspectives, further experimental validation and more detailed modeling are required before confirming its suitability as a direct replacement for fiberglass in industrial applications.

4.5 Discussion

To the best of the authors' knowledge, no previous studies have systematically investigated the mechanical response of reinforced gummed paper or quantified the role of the embedded reinforcing filament. While the underlying mechanisms governing paper behavior under different conditions are well established in the literature, the present work contributes by adapting these established concepts to a specific industrial material and by introducing a practical modeling strategy in which the response of the paper network is combined with a deterministic representation of the reinforcing filament. This approach provides a computationally efficient tool for predicting the tensile behavior of reinforced gummed paper and for exploring design modifications without resorting to full-scale experimental campaigns.

Within this framework, the parametric analysis indicates that replacing the conventional synthetic fiberglass filament with a natural flax fiber can preserve, and in some cases even enhance, the mechanical performance of the reinforced paper. Beyond mechanical considerations, this substitution offers additional advantages in terms of reduced environmental impact, renewability, and lower cost, making natural fibers particularly attractive for sustainable packaging applications. However, it is important to emphasize that these findings should be interpreted as part of a parametric mechanical feasibility study, in which only the intrinsic properties of the reinforcing fibers are varied. Factors such as processing-induced damage, moisture sensitivity, and the quality of the fiber–paper interface are not considered in the present model, although they could affect the actual performance.

In particular, the sensitivity of natural fibers to moisture represents an important aspect that should be taken into account when evaluating their practical applicability. Due to their cellulose-rich structure and porous nature, fibers such as flax and hemp are inherently hydrophilic and tend to absorb moisture from the environment. This moisture uptake alters the internal hydrogen bonding within the fiber cell wall, leading to a reduction in stiffness and strength and promoting a more ductile mechanical response. At the composite scale, the presence of moisture can also weaken the bonding between the fibers and the surrounding paper matrix, thereby reducing load-transfer efficiency [95, 96, 97].

Surface treatments can help mitigate some of these effects by reducing fiber hydrophilicity and improving fiber–matrix adhesion. In general, treated fibers exhibit enhanced mechanical performance and lower moisture absorption, contributing to improved durability of the composite system [98, 99, 97]. In this context, a more comprehensive representation of moisture-dependent behavior would require dedicated experimental characterization under controlled environmental conditions. For this reason, the present analysis is limited to dry fiber conditions. A more detailed investigation of moisture effects represents an important direction for future work, particularly for assessing the long-term performance and reliability of natural fibers in reinforced gummed papers.

At the same time, the proposed framework relies on a number of simplifying assumptions that define its range of applicability. The model adopts a reduced-order, cross-sectional representation of the paper network, whereby the tensile response is governed by a representative section. As a consequence, the spatial architecture of the fibrous network is not explicitly resolved, and localized damage evolution, crack initiation, and progressive failure mechanisms associated with non-uniform stress redistribution cannot be captured. In addition, the reinforcing filament is modeled as a linearly elastic component that is fully strain-compatible with the surrounding paper network, without explicit consideration of interfacial behavior. Therefore, effects such as interfacial slip, debonding, or shear transfer through the adhesive layer are not included in the formulation.

Therefore, the present study proposed a simple yet effective approach to investigate and interpret the response of filament-reinforced gummed paper in relation to a uniaxial testing setup that can be easily replicated in the paper industry framework. Failure strain parameters should be considered as lumped parameters for mesoscale simulations. Their identification according to experimental tests would provide single key numbers to be used for the classification of the efficiency of new eco-sustainable solutions based on natural reinforcing fibers.

Extending the analysis to multiple filaments or different reinforcement patterns would require a different computational approach that is left for future research. In this regard, we know that the presence of sub-network structures with different material and geometrical arrangements has a significant effect on the overall evolution of damage in the material, as recently shown using a finite element-based discrete model of a lattice material with fully-bonded joints but with phase field damage evolution on the lattice elements [100]. Hence, one interesting possibility to pursue could be to extend the methodology recently published in [101], explicitly incorporating the filaments and their joint properties into the model.

Chapter 5

An experimental investigation of the anisotropic fracture behavior of paperboard under uniaxial tension

Paper-based materials such as paperboard exhibit mesostructural anisotropy due to the alignment of fibers along a preferred direction during manufacturing, referred to as the machine direction (MD). This inherent anisotropy significantly influences both the elastic response and the fracture path under tensile loading. Depending on the relative orientation between the applied load and the fiber alignment, cracks may propagate along the fibers, across them, or at oblique angles. Understanding the relationship between the anisotropy angle and crack propagation is therefore useful for predicting the failure mechanisms of paper structures.

In this study, an experimental campaign was conducted to investigate the anisotropic fracture behavior of paperboard under uniaxial tensile loading. Dog-bone specimens were prepared by laser cutting at orientations of 0°, 30°, 45°, 60°, 90° with respect to the MD, see Fig. 41. For each orientation, a minimum of four samples were tested. The specimens had a uniform thickness of $t = 1$ mm, a span length of $L = 26.4$ mm, and a width of $B = 10$ mm.

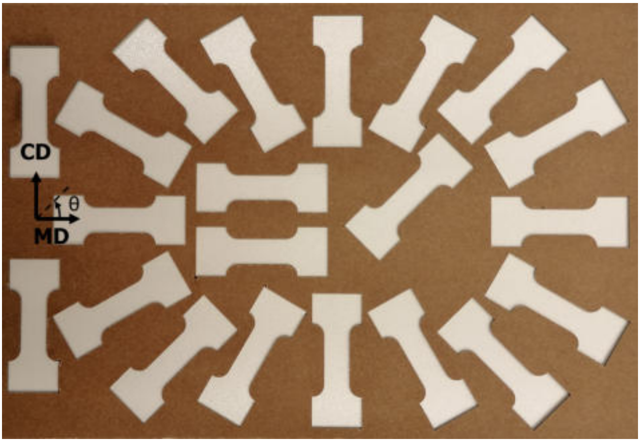

Figure 41: Schematic representation of the dog-bone specimens cut from the paperboard at different orientations relative to the machine direction.

For each anisotropy orientation, uniaxial tensile tests were performed using a DEBEN micro-mechanical tensile stage at the MUSAM laboratory. The specimens were clamped at both ends, and the corresponding force–displacement response was recorded during testing. Stress–strain curves were then obtained by normalizing the measured displacement by the specimen gauge length and the applied force by the specimen cross-sectional area. The resulting curves for all anisotropy angles are presented in Fig. 42. Curves corresponding to the same anisotropy angle are plotted in the same color, while different line styles (solid, dashed, etc.) distinguish between replicates. The results clearly demonstrate the anisotropic mechanical behavior of the paperboard: the elastic modulus, maximum load-bearing capacity, and strain at failure all vary with orientation. As expected, the machine direction ($0°$) exhibits the highest stiffness and strength due to fiber alignment, whereas the cross direction ($90°$) shows lower stiffness but greater elongation at failure.

To analyze the fracture anisotropy of the paperboard, the fractured region

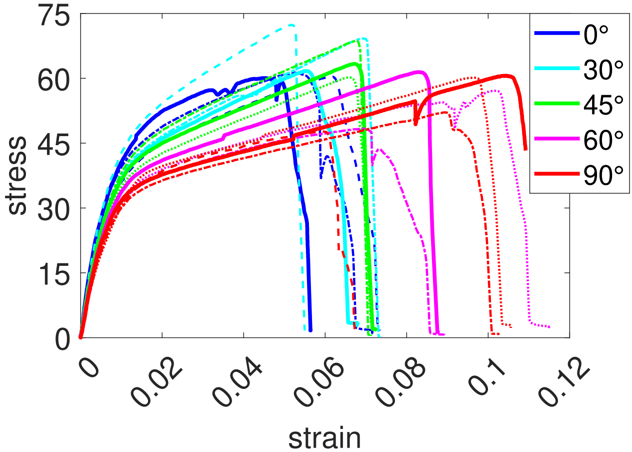

Figure 42: Stress–strain curves of paperboard specimens at different anisotropy orientations (0°, 30°, 45°, 60°, 90°). Each color represents one orientation, and line styles distinguish the individual specimens within each group.

of each specimen was recorded and examined. Representative images of three specimens for each anisotropy orientation are presented in Figs. 43, 44, 45, 46 and 47, except for the cross machine direction (90°), where images of two specimens are shown. These images were captured using optical microscopy after the completion of the tensile tests. As observed, the crack propagation angles vary for each anisotropy orientation, yet they appear to exhibit a certain relationship across orientations, reflecting the anisotropic nature of the fracture behavior.

To investigate a possible correlation between crack propagation and anisotropy orientation, different measurement procedures were applied to quantify the crack angles. The first procedure focused on the crack angle at the initial stage of nucleation. For example, in the specimen shown in Fig. 48, the crack originated from the left edge and propagated toward the right side of the sample. Since the crack path may consist of several segments with different orientations, only the angle at the very onset of nucleation (e.g., from the left edge in Fig. 48) was considered

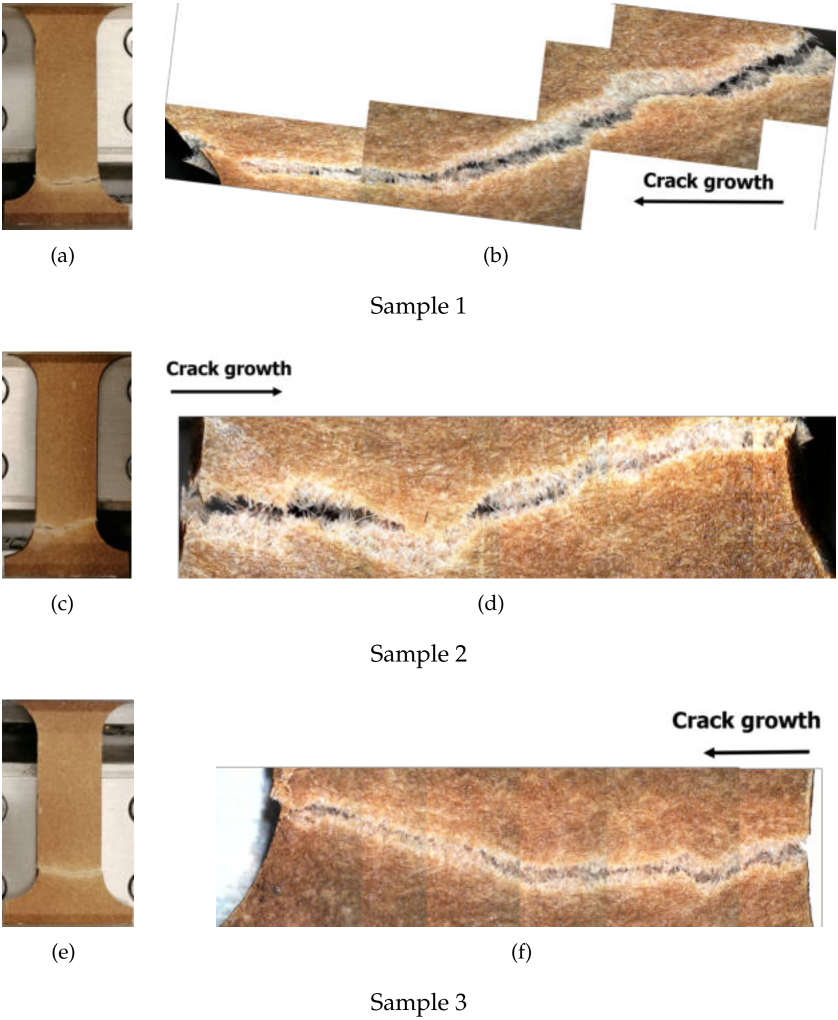

Figure 43: Fracture surfaces of paperboard samples at the anisotropy angle of 0°.

(a)

(b)

Sample 1

(c)

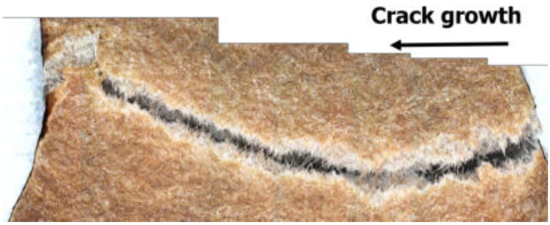

(d)

Sample 2

(e)

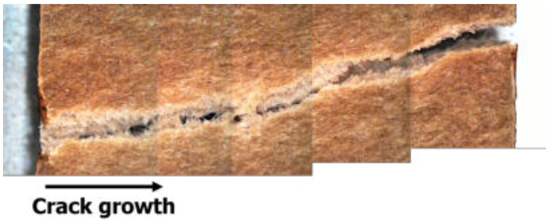

(f)

Sample 3

Figure 44: Fracture surfaces of paperboard samples at the anisotropy angle of 30°.

(a)

(b)

Sample 1

(c)

(d)

Sample 2

(e)

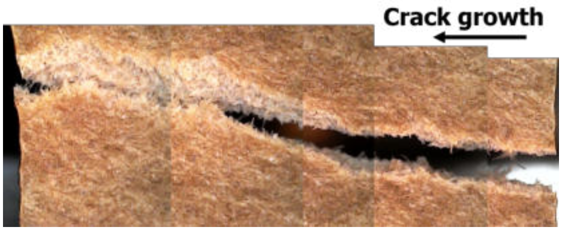

(f)

Sample 3

Figure 45: Fracture surfaces of paperboard samples at the anisotropy angle of 45°.

(a)

(b)

Sample 1

(c)

(d)

Sample 2

(e)

(f)

Sample 3

Figure 46: Fracture surfaces of paperboard samples at the anisotropy angle of 60°.

(a)

(b)

Sample 1

(c)

(d)

Sample 2

Figure 47: Fracture surfaces of paperboard samples at the anisotropy angle of 90°.

in this approach. The crack angle, denoted as β, was measured for each specimen using the image-processing software ImageJ, which enabled precise angle determination.

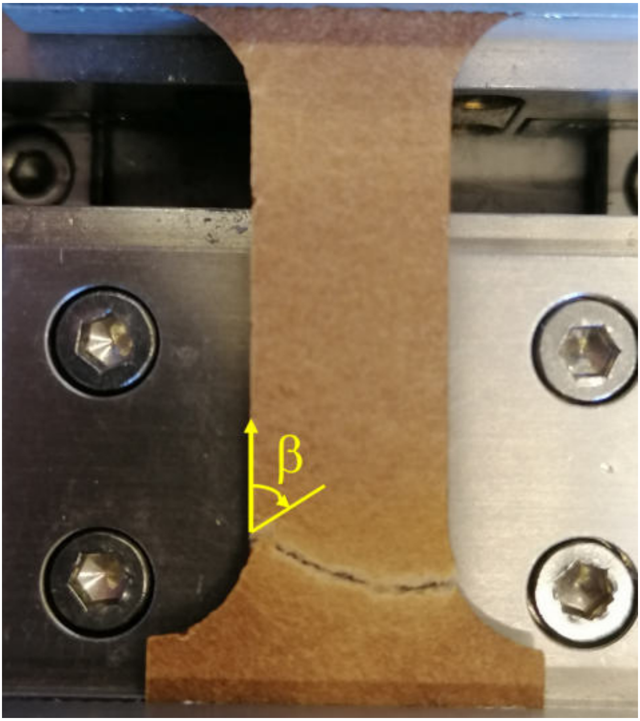

Figure 48: Illustration of the procedure used to measure the crack nucleation angle, β. The angle was determined at the very onset of crack initiation, starting from the edge where the crack originated (in this example, the left side of the specimen).

The measured values of β were then compared with the corresponding anisotropy orientations, denoted as θ, as presented in Fig. 49. Each data point represents an individual specimen, color-coded according to its anisotropy orientation, ranging from 0° to 90°. The figure supports the hypothesis that anisotropy orientation significantly influences the initial crack angle in uniaxial tensile tests. While some orientations (e.g., 45°–60°)

yield consistent crack directions, others (e.g., 0° and 90°) exhibit greater variability. This trend suggests that the internal fiber architecture and its alignment relative to the loading axis play a critical role in fracture behavior.

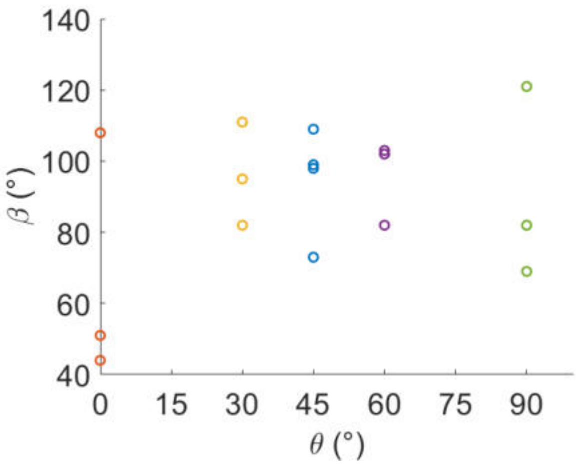

Figure 49: Relationship between crack angles at nucleation onset β and anisotropy orientations θ in paperboard specimens. Each data point represents an individual test, color-coded by θ.

To further investigate the relationship between crack propagation and anisotropy orientation in paperboard specimens, a second measurement method was employed. Unlike the first approach, which focused solely on the crack angle at the onset of nucleation, this method quantified the angle of the longest segment of the crack path during nucleation. This segment was selected to better represent the dominant direction of crack propagation, especially in cases where the crack path exhibited curvature or multiple directional changes.

Fig. 50 presents the angles measured along the longest segment of the nucleation path, plotted against their corresponding anisotropy orientations. This second measurement approach reveals a more distinct correlation between anisotropy direction and crack propagation. Notably, specimens with anisotropy angles between 30° and 60° exhibit more consistent crack angles, indicating that the internal fiber architecture at these orientations plays a significant role in guiding fracture behavior.

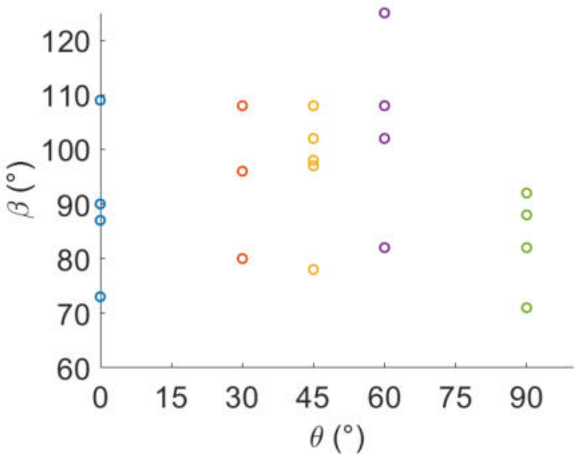

Figure 50: Relationship between angles of the longest portion of crack at nucleation onset β and anisotropy orientations θ in paperboard specimens. Each data point represents an individual test, color-coded by θ.

Finally, another procedure was applied to characterize the overall crack orientation by averaging the angles of the different crack segments. As illustrated in Fig. 51, the fracture path of a specimen may consist of several portions with distinct orientations. To obtain a representative value, a length-weighted average crack angle was computed as:

$$\beta_{\mathbf{avg}} = \frac{\sum_{i=1}^{N} \beta_i L_i}{\sum_{i=1}^{N} L_i} \tag{5.1}$$

where β_i and L_i are the orientation and the length i^{th} portion of the crack, respectively, and N is the total number of segments. For example, in the sample shown in Fig. 51, the crack path can be devided into 4 segments with different orientations. By convention, β_i is defined as positive for counterclockwise orientations. Accordingly, in this example (shown in Fig. 51), the third crack segment is characterized by a negative angle.

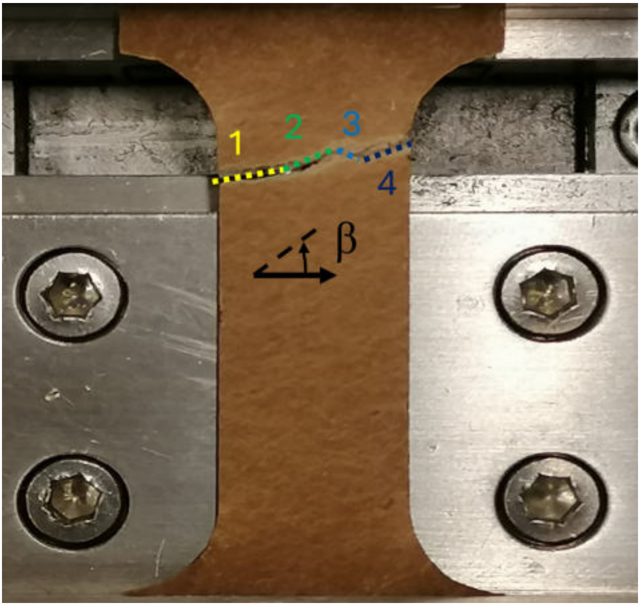

Figure 51: Example of a fractured specimen with the crack path divided into four segments. Segment orientations (β_i) and lengths (L_i) are used to compute the weighted average crack angle $\beta_{\mathbf{avg}}$.

Figure 52 shows the average crack angles of all specimens for different anisotropy orientations. This method, which considers the entire crack path, minimizes the effect of local irregularities and provides a more reliable measure of crack direction. The results indicate that $\beta_{\mathbf{avg}}$ remains relatively small and consistent across orientations, suggesting that while local deviations occur, the overall crack trajectory is mainly controlled by the fiber alignment. This demonstrates that anisotropy influences both the initiation and the global propagation of cracks.

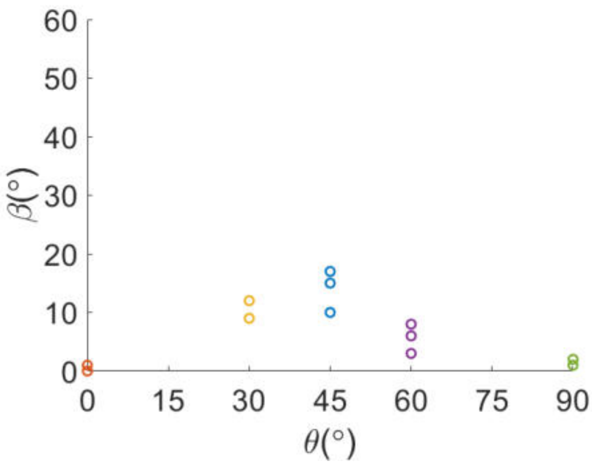

Figure 52: Average crack angles, $\beta_{\mathbf{avg}}$, of specimens at different anisotropy orientations. Values are obtained by integrating the orientations of all crack segments along each fracture path.

Chapter 6

Conclusion

This final chapter synthesizes the key findings obtained throughout the thesis. The work began with the experimental evaluation of micromechanical phenomena governing the fracture of paper materials. Based on these observations, a stochastic micromechanical model was developed to better understand and predict the fracture behavior of anisotropic paper networks under uniaxial tensile loading. To extend the analysis toward engineering applications, where reliable predictions of the mechanical behavior under complex loading conditions are required, a continuum framework was then employed. Within this framework, two nonlinear anisotropic models were formulated, enabling the prediction of paper responses under biaxial stress–strain states. Importantly, these models were designed to maintain a direct correlation with the stochastic micromechanical model, allowing the evaluation of local fracture processes occurring at each material point.

Furthermore, by extending the proposed stochastic micromechanics approach, the mechanical behavior of reinforced gummed papers was analyzed and predicted. This led to the identification of natural fibers as sustainable alternatives to synthetic glass fibers in such composites, contributing to the development of environmentally friendly paper-based packaging materials. Finally, the thesis presented an experimental investigation of the anisotropic fracture behavior of paperboard, providing additional validation and insight into the fracture mechanisms of cellulose-based materials. The following sections summarize and discuss the main outcomes of each study, emphasizing their interconnections and their collective contribution to advancing predictive models for paper and paperboard.

6.1 Conclusion for a novel in-situ micro-mechanical testing of paper fracture and its stochastic network model [1]

In Chapter 2 in order to understand the micro-structural mechanisms governing the fracture behavior of paper materials, we conducted a campaign of in-situ tensile tests using the DEBEN micro-mechanical tensile stage combined with the confocal microscope Leica DCM3D. This setup enables the simultaneous visualisation of the cellulose fibers' deformation during the loading process, observing microstructural mechanisms such as fiber activation and recruitment, fiber debonding and fiber failure. Notably, these individual mechanisms are found to be dependent on the fiber average free length between subsequent bonds.

Inspired by our experimental findings, we proposed a stochastic mechanics model as a valuable tool for comprehensively examining the mechanical response of paper sheets under uniaxial loading. The model clearly decouples the information on the topology of the fiber network from the mechanical constitutive response of each single fiber. Micro-geometrical data that can be identified from microscopy images include the new morphological parameter called mean free path λ between two subsequent bonds, the mean fiber diameter, the fiber orientation and the fiber length, in addition to the number of fibers along a cross-section. Fiber orientation and fiber length are considered as random fields obeying a Gaussian distribution. The mean free path is also modelled as a random field obeying an exponential distribution with an average value that can be estimated from images. Through the functional dependencies

[1] This section is based on our publication Fallah, Zarei, and Paggi [59].

of the model, the activation strain and the failure strain of the fibers become random fields as well. The constitutive model of the fibers has been considered as linear elastic. It has to be remarked that the model is not a pure cross-sectional model, since the parameters include the free segment length of the fibers which is an additional information relevant for this type of networks and includes longitudinal features of the network. This allows for a more comprehensive analysis that acknowledges the non-affine behavior introduced by phenomena like fiber recruitment and debonding failure.

The model parameters were determined based on three paper materials with different densities, aligning the simulation outcomes with the corresponding experimental results for each sample. The simulations emphasized the critical influence of density and the papermaking process on the strength of paper materials, showcasing substantial changes in mechanical properties. Furthermore, the simulations highlighted that paper fracture predominantly arises from fiber debonding rather than breakage, especially in the cross-machine direction (CD). The disparity in the number of active fibers between the machine direction (MD) and CD contributes to the anisotropy observed in paper materials. Additionally, an investigation into the changes in the slope of stress-strain curve was conducted by correlating it with the percentage of failed fibers versus strain.

The sensitivity analysis led to the observation that the inter-fiber bond strength and the fiber elongation at failure are significantly affecting the overall mechanical response. The constitutive model of the fibers also plays an important role, in which the Young modulus of the fibers significantly influences the paper stiffness and the peak force. Redistribution effects, on the other hand, impact on the shape of the stress-strain curve near the peak load, with an increased smoothing and flattening of the curve for higher values of r.

6.2 Conclusion for nonlinear anisotropic hypoelastic continuum models for paper materials and their relation to statistical micromechanics [2]

In chapter 3 we tackled the fundamental problem of modeling and simulation of biaxial plane stress states on paper sheets with arbitrary geometry, imperfections like holes, and subject to arbitrary loading conditions. Contrary to uniaxial stress states, these structural problems cannot be solved using semi-analytical equations or fiber-bundle models, and continuum formulations have to be addressed within the finite element method.
First, departing from the experimental evidence that paper damage is triggered by the direction of the maximum principal strain and it is the result of progressive debonding of the cross-links between cellulose fibers and by fibers breakage, we explored the possibility to introduce in the continuum formulation a damage variable function of the maximum principal strain and its direction. Moreover, the fact that the nonlinear mechanical response in the unixial tensile tests is captured very well according to the statistical micromechanics approach which does not include any plastic effect further motivated the use of a nonlinear elastic framework rather than elasto-plasticity, at least for the type of cellulose fibers herein analyzed.
Based on those premises, we accounted for the effect of material anisotropy under two forms. The former model employed an orthotropic constitutive tensor with a degradation function dependent on the maximum principal strain and on the mismatch angle $\overline{\phi}$ between the the average fiber direction and the direction of the maximum principal tensile strain. The latter adopted an isotropic constitutive tensor with an effective elastic modulus E function of $\overline{\phi}$, and with the same degradation function as the orthotropic model. The relation governing the effective elastic modulus $E(\overline{\phi})$ has been determined by fitting experimental results from uniaxial tensile tests and it has been found to be simply linear.

[2]This section is based on our publication Fallah, Lenarda, and Paggi [85].

Using the same parameters identified from uniaxial tensile tests, two independent validation tests under biaxial conditions have been made and results are quite promising up to the peak load, with the isotropic nonlinear model with an effective elastic modulus function of $\overline{\phi}$ performing very well.
The nonlinear anisotropic damage function $d(\epsilon_1, \overline{\phi})$ used in both continuum models allowed simulating the progressive stiffness degradation by assuming that, at the point level, damage is governed by the fibers activated and deformed along the direction β of the maximum principal strain. Since such quantities are governing also the mechanical response predicted by the statistical micromechanics model, this opened the possibility to call it at the material point level to provide further predictions on the percentage of fibers debonded or broken on a representative RVE in that location. Such information cannot be gained from standard continuum approaches and, as discussed in relation to the two validation tests, provided relevant insight into the mechanical failure phenomena that take place in paper materials as a result of their intrinsic anisotropy.
As prospective research directions, nonlocal damage formulations could be considered to follow the post-peak branch of the force-displacement curves and the evolution of the crack path. Moreover, due to the analogies between cellulose paper materials and collagen tissues in terms of cross-linking effects, the possibility to explore modeling approaches based on refined statistics used in tissue engineering [102, 103, 104, 105, 106] could be interesting to make further progress on the accurate assessment of the average and dispersion of the material stiffness in the linear and nonlinear regimes. Finally, assessing the dependency of the model parameters on different types of cellulose fibers would be relevant for sustainability considerations, since the model could provide an insight onto the use of other biological sources than wood, such as cellulose extracted from cotton or hemp.

6.3 Conclusion for modelling and experiments of filament-reinforced paper for sustainable packaging

In chapter 4, we developed a statistical micro-mechanical model to investigate the tensile response of fiber-reinforced paper, with the specific technological goal of evaluating the potential replacement of synthetic fiberglass filaments with more sustainable natural fibers. The model incorporates the statistical variability of fiber orientation and free segment length, as well as failure mechanisms and local strain redistribution within a layered cellulose network. To ensure accuracy, the model was validated using experimental data from samples without reinforcing filaments and then applied to simulate the mechanical response of fiberglass-reinforced paper by including the additional contribution of a single embedded filament.

The model predictions showed excellent agreement with the experimental stress–strain response of the fiberglass-reinforced sample, capturing both the increase in stiffness and peak strength due to the filament, as well as the post-peak behavior. This validation established the model as a reliable tool for investigating the specific effect of changing the reinforcement in layered paper systems. Leveraging this validated framework, we simulated the mechanical performance of reinforced gummed papers using natural fibers, specifically hemp, kenaf, and flax substitutes for fiberglass. The results revealed that flax fibers, particularly flax 2, provided mechanical behavior closest to fiberglass in terms of stiffness and tensile strength. Hence, natural fibers offer substantial reinforcement as compared to unreinforced paper and do so with a significantly lower cost and environmental impact.

Importantly, this study highlights a key industrial gap: while fiberglass filaments are currently used in commercial reinforced gummed papers, no existing products have adopted natural fiber reinforcements. Our modeling approach not only fills a crucial knowledge gap in understanding the mechanics of these hybrid paper systems but also introduces a pathway for industrial innovation. By identifying flax as a high-performing nat-

ural alternative, this work supports the development of fully bio-based packaging materials that are strong, recyclable, biodegradable, affordable and aligned with circular economy goals.
As a main conclusion, the present work demonstrates the versatility of the proposed analytical method to support the design of innovative packaging and compare alternative reinforcement strategies, providing a way to interpret uniaxial tensile tests on different gummed paper compositions that can be carried out within an industrial facility. More broadly, the model provides a predictive and computationally efficient tool that can assist in the material selection and optimization of reinforced paper systems at the design stage, reducing reliance on extensive experimental testing. This capability is particularly relevant for the development of next-generation sustainable packaging solutions, where performance, cost, and environmental impact must be simultaneously balanced. Moreover, the results suggest strong potential for industrial innovation, paving the way for the development of fully bio-based reinforced paper packaging solutions with minimal reliance on synthetic materials.

6.4 Summery and final remarks for an experimental investigation of the anisotropic fracture behavior of paperboard under uniaxial tension

Chapter 5 experimentally examined the anisotropic fracture behavior of paperboard through uniaxial tensile tests performed at different fiber orientations relative to the machine direction. The results revealed a clear dependence of both the elastic and fracture responses on the anisotropy angle. Specimens aligned with the machine direction exhibited higher stiffness and peak strength, whereas those loaded transversely showed lower stiffness but greater ductility before failure.
Analysis of fracture paths demonstrated that the crack propagation direction is strongly influenced by fiber alignment. Although local deviations and tortuous crack paths were observed, the overall crack trajectory re-

mained predominantly governed by the anisotropic fiber network. By quantifying the crack orientation through length-weighted averaging, it was shown that the global fracture direction correlates well with the intrinsic fiber alignment, confirming the coupling between mesostructure and macroscopic fracture.

These findings validate the predictive assumptions underlying the micromechanical and continuum models developed in earlier chapters. The observed relationship between anisotropy and fracture direction supports the modeling approach in which the damage evolution and stiffness degradation depend on the mismatch between fiber orientation and principal strain direction. Hence, the experiments provide a strong physical basis for the anisotropic damage formulation and demonstrate the capacity of the proposed framework to capture the interplay between material microstructure and fracture behavior.

In conclusion, the anisotropic fracture study bridges experimental evidence and computational modeling, reinforcing the reliability of the developed multi-scale approach. The results not only improve our understanding of paperboard failure mechanisms but also offer valuable guidance for the design of paper-based components where crack control and directional stiffness are critical.

6.5 Future works

The research presented in this thesis establishes a solid foundation for multi-scale modeling and experimental analysis of cellulose-based materials. Nevertheless, several aspects remain open for further investigation to deepen the understanding of paper mechanics and to extend the predictive capability of the developed framework.

A natural continuation of this work involves examining the influence of specimen size on the fracture behavior of paper materials. Experimental testing on samples of different dimensions would allow quantifying how size affects strength, fracture energy, and damage localization. The stochastic micromechanical model could then be employed to interpret these results, identifying which microstructural parameters—such as fiber orientation, free segment length, or bond density—are most sensitive to variations in sample size. This investigation could ultimately lead to defining a minimum representative specimen size beyond which the mechanical response of paper becomes statistically stable and independent of dimensions, providing an essential guideline for both experimental design and numerical modeling.

Another important direction concerns the refinement of the modeling formulations through the inclusion of fiber bending stiffness. In the current approach, fibers are primarily considered as axial load-carrying components, while their bending contributions are neglected. However, in real fibrous networks, bending plays a crucial role in the overall deformation process, especially at low strain levels or in regions where fibers bridge voids and misaligned bonds. Introducing fiber bending stiffness into the model would allow a more realistic representation of the mechanical interactions between fibers, including their tendency to resist local curvature and to recover partially after unloading.

Accounting for this effect would enable the simulation of additional deformation mechanisms that are particularly relevant in out-of-plane loading and bending-dominated configurations, such as those encountered in folding, creasing, or multi-layered paperboard applications. Moreover, incorporating bending stiffness would improve the model's ability to capture local instabilities and the interaction between tensile and flexural modes during damage evolution. This enhancement is therefore expected to significantly increase the predictive accuracy of the continuum model and provide a more comprehensive representation of the mechanical response of paper-based structures under a wide range of loading and boundary conditions.

In parallel, the effect of frictional interactions between fibers should be analyzed in greater detail. In fibrous materials such as paper, friction at fiber–fiber contacts plays a fundamental role in the redistribution of local stresses, in the onset of energy dissipation, and in the progressive damage process. Future work could introduce frictional contact laws into the stochastic micromechanical model, allowing the evaluation of how inter-fiber friction influences the nonlinear and hysteretic response observed during cyclic loading and unloading. A better understanding of this mechanism could significantly improve the modeling of stiffness recovery, energy dissipation, and the transition from elastic to damage-dominated behavior.

A further research avenue is the definition of a rigorous fracture criterion for paper and paperboard. While the current framework effectively describes the onset and evolution of damage, establishing a physically grounded failure criterion—based on local stress, strain, or energy release rate—would enable more quantitative predictions of crack initiation and propagation. Such a criterion could be developed by integrating micromechanical simulations with experimental fracture data, leading to a unified and transferable approach that connects the micro-scale processes of fiber failure and debonding to macroscopic fracture laws.

Extending the investigation to hand-made paper materials would also provide valuable insights into the role of fiber distribution and fabrication process on mechanical anisotropy. Since hand-made papers may exhibit nearly isotropic behavior, targeted experiments and model extensions could clarify which microstructural parameters—such as fiber alignment, bonding density, and surface roughness—govern the transition from isotropy to anisotropy. These findings would be particularly relevant for the development of sustainable, small-scale papermaking techniques where control over fiber orientation is limited but mechanical performance remains crucial.

Beyond these directions, additional research could explore the coupling between mechanical and environmental effects, such as humidity and temperature, which are known to influence fiber stiffness, bond strength, and overall damage evolution. Incorporating these hygro-mechanical interactions into the multi-scale framework would allow predicting the long-term durability of paper-based components under realistic service conditions. Another promising development involves the integration of machine learning strategies to accelerate parameter identification and uncertainty quantification within both the stochastic and continuum frameworks, thereby enabling efficient simulations of large-scale paper-based structures.

Altogether, these future research directions will further advance the understanding of cellulose-based materials across multiple scales. By combining improved physical modeling, extended experimental validation, and advanced computational tools, they will promote the predictive design of next-generation paper and paperboard systems for sustainable engineering and packaging applications.

Bibliography

[1] CW. Sanjon et al. “Methods for characterization and continuum modeling of inhomogeneous properties of paper and paperboard materials: A review”. In: *BioResources* 19.3 (2024), p. 6804.

[2] A. Vishtal and E. Retulainen. “Deep-drawing of paper and paperboard: The role of material properties”. In: *BioResources* 7.3 (2012), pp. 4424–4450.

[3] Y. Su et al. “Prospects for Replacement of Some Plastics in Packaging with Lignocellulose Materials: A Brief Review.” In: *BioResources* 13.2 (2018).

[4] A. Cordeiro et al. “Advancements in Packaging Materials: Trends, Sustainability, and Future Prospects”. In: *Circular Economy and Sustainability* 5 (2025), pp. 2959–2990.

[5] Md. Shafiqul Islam. “Fracture and delamination in packaging materials: A study of experimental methods and simulation techniques”. PhD thesis. Blekinge Tekniska Högskola, 2019.

[6] JC. Little, ET. Hester, and CC. Carey. “Assessing and enhancing environmental sustainability: a conceptual review”. In: *Environmental science & technology* 50.13 (2016), pp. 6830–6845.

[7] NM. Stark and LM. Matuana. “Trends in sustainable biobased packaging materials: A mini review”. In: *Material Today Sustainability* 15 (2021), p. 100084.

[8] RC. Picu. “Mechanics of random fiber networks—a review”. In: *Soft Matter* 7.15 (2011), pp. 6768–6785.

[9] RC. Picu. “Mechanics of random fiber networks: Structure–properties relation”. In: *Mechanics of Fibrous Materials and Applications: Physical and Modeling Aspects*. Springer, 2019, pp. 1–61.

[10] MR. Islam and RC. Picu. “Effect of network architecture on the mechanical behavior of random fiber networks”. In: *Journal of Applied Mechanics* 85.8 (2018), p. 081011.

[11] JW. Simon. “A Review of Recent Trends and Challenges in Computational Modeling of Paper and Paperboard at Different Scales.” In: *Archives of Computational Methods in Engineering* 28.4 (2021).

[12] BS. Ojelade, RI. Nethanani, and PO. Adesoye. “Cellulose-Based Materials as a Sustainable Alternative to Plastics: Mitigating Environmental Pollution Through Biodegradability and Reduced Toxicity”. In: *Nature Environment and Pollution Technology* 25.1 (2026), pp. 1–16.

[13] J. Wang et al. “Towards a cellulose-based society: opportunities and challenges”. In: *Cellulose* 28.8 (2021), pp. 4511–4543.

[14] BC. Brusso. “Development of stone writing and packaging materials [history]”. In: *IEEE Industry Applications Magazine* 27.6 (2021), pp. 8–11.

[15] ZY. Gao. “A Research on Early Spread of Traditional Hand-made Paper in East Asia Countries”. In: *Advanced Materials Research* 174 (2011), pp. 537–540.

[16] GJM. Goedvriend. “Papermaking past and present”. In: *Endeavour* 12.1 (1988), pp. 38–43.

[17] NA. Poirier et al. *'Papermaking'*. Tech. rep. 2016.

[18] ES. Abd El-Sayed, M. El-Sakhawy, and MA. El-Sakhawy. “Non-wood fibers as raw material for pulp and paper industry”. In: *Nordic Pulp & Paper Research Journal* 35.2 (2020), pp. 215–230.

[19] Z. Liu, H. Wang, and L. Hui. “Pulping and papermaking of non-wood fibers”. In: *Pulp and paper processing* 1 (2018), pp. 4–31.

[20] M. Pydimalla, HV. Chirravuri, and AN Uttaravalli. “An overview on non-wood fiber characteristics for paper production: sustainable management approach”. In: *Materials Today: Proceedings* (2023).

[21] LA. Worku et al. “Agricultural residues as raw materials for pulp and paper production: overview and applications on membrane fabrication”. In: *Membranes* 13.2 (2023), p. 228.

[22] A. Karimah et al. “A review on natural fibers for development of eco-friendly bio-composite: characteristics, and utilizations”. In: *Journal of materials research and technology* 13 (2021), pp. 2442–2458.

[23] P. Rousu, P. Rousu, and J. Anttila. “Sustainable pulp production from agricultural waste”. In: *Resources, Conservation and Recycling* 35.1-2 (2002), pp. 85–103.

[24] SH. Osong, S. Norgren, and P. Engstrand. “Processing of wood-based microfibrillated cellulose and nanofibrillated cellulose, and applications relating to papermaking: a review”. In: *Cellulose* 23.1 (2016), pp. 93–123.

[25] J. Phipps. “Current and potential use of highly fibrillated cellulose in the paper and board industry”. In: *Advances in Pulp and Paper Research* (2022), pp. 249–268.

[26] D. Klemm et al. “Nanocelluloses as innovative polymers in research and application”. In: *Polysaccharides ii*. Springer, 2006, pp. 49–96.

[27] A.L. Barabasi. “From physical network to network materials”. In: *APS Global Physics Summit*. Americal Physical Society, Mar. 2025.

[28] G. Chinga-Carrasco. “Exploring the multi-scale structure of printing paper–a review of modern technology”. In: *Journal of Microscopy* 234.3 (2009), pp. 211–242.

[29] G. Chinga-Carrasco. “Cellulose fibres, nanofibrils and microfibrils: The morphological sequence of MFC components from a plant physiology and fibre technology point of view”. In: *Nanoscale Research Letters* 6 (2011), pp. 1–7.

[30] Ch. Lorbach et al. “Automated 3D measurement of fiber cross section morphology in handsheets”. In: *Nordic Pulp & Paper Research Journal* 27.2 (2012), pp. 264–269.

[31] Y. Sharma, AB. Phillion, and DM. Martinez. “Automated segmentation of wood fibres in micro-CT images of paper”. In: *Journal of Microscopy* 260.3 (2015), pp. 400–410.

[32] S. Maraghechi et al. “Experimental characterisation of the local mechanical behaviour of cellulose fibres: an in-situ micro-profilometry approach”. In: *Cellulose* 30.7 (2023), pp. 4225–4245.

[33] C. Czibula et al. “Estimation of the in-situ elastic constants of wood pulp fibers in freely dried paper via AFM experiments”. In: *arXiv preprint 2012.03037* (2020).

[34] J. Kouko et al. “Understanding extensibility of paper: role of fiber elongation and fiber bonding”. In: *Tappi J* 19.3 (2020), pp. 125–135.

[35] A. Torgnysdotter et al. “Fiber/fiber crosses: finite element modeling and comparison with experiment”. In: *Journal of Composite Materials* 41.13 (2007), pp. 1603–1618.

[36] MS. Magnusson et al. “Interfibre joint strength under peeling, shearing and tearing types of loading”. In: *Adv. Pulp Pap. Res. Cambridge* (2013), pp. 103–124.

[37] MS. Magnusson, Xiaobo Zhang, and Sören Östlund. “Experimental evaluation of the interfibre joint strength of papermaking fibres in terms of manufacturing parameters and in two different loading directions”. In: *Experimental mechanics* 53.9 (2013), pp. 1621–1634.

[38] H. Zarei et al. “Digital Twin Model of Paper–Aluminum Laminates for Sustainable Packaging”. In: *ACS Omega* 9.41 (2024), pp. 42386–42395.

[39] M. Paggi and J. Reinoso. “An anisotropic large displacement cohesive zone model for fibrillar and crazing interfaces”. In: *International Journal of Solids and Structures* 69 (2015), pp. 106–120.

[40] M. Ali et al. “3D synchrotron X-ray microtomography for paper structure characterization of z-structured paper by introducing micro nanofibrillated cellulose”. In: *Nordic Pulp & Paper Research Journal* 31.2 (2016), pp. 219–224.

[41] MA. Charfeddine, JF. Bloch, and P. Mangin. “Mercury porosimetry and X-ray microtomography for 3-dimensional characterization of multilayered paper: nanofibrillated cellulose, thermomechanical pulp, and a layered structure involving both”. In: *BioResources* 14.2 (2019), pp. 2642–2650.

[42] S. Borodulina et al. “Extracting fiber and network connectivity data using microtomography images of paper”. In: *Nordic Pulp & Paper Research Journal* 31.3 (2016), pp. 469–478.

[43] JX. Liu, ZT. Chen, and KC. Li. “A 2-D lattice model for simulating the failure of paper”. In: *Theoretical and Applied Fracture Mechanics* 54.1 (2010), pp. 1–10.

[44] DV. Wilbrink, LAA. Beex, and RHJ. Peerlings. “A discrete network model for bond failure and frictional sliding in fibrous materials”. In: *International Journal of Solids and Structures* 50.9 (2013), pp. 1354–1363.

[45] A. Ekman et al. “Contact formation in random networks of elongated objects”. In: *Physical Review Letters* 113.26 (2014), p. 268001.

[46] V. Negi and RC. Picu. "Mechanical behavior of cross-linked random fiber networks with inter-fiber adhesion". In: *Journal of the Mechanics and Physics of Solids* 122 (2019), pp. 418–434.

[47] E. Sozumert et al. "Deformation and damage of random fibrous networks". In: *International Journal of Solids and Structures* 184 (2020), pp. 233–247.

[48] M. Alzweighi et al. "Anisotropic damage behavior in fiber-based materials: Modeling and experimental validation". In: *Journal of the Mechanics and Physics of Solids* 181 (2023), p. 105430.

[49] R. Mansour et al. "Stochastic constitutive model of isotropic thin fiber networks based on stochastic volume elements". In: *Materials* 12.3 (2019), p. 538.

[50] M. Harrysson and M. Ristinmaa. "Description of evolving anisotropy at large strains". In: *Mechanics of Materials* 39.3 (2007), pp. 267–282.

[51] P. Mäkelä and S. Östlund. "Orthotropic elastic–plastic material model for paper materials". In: *International Journal of Solids and Structures* 40.21 (2003), pp. 5599–5620.

[52] G. Kloppenburg et al. "Using numerical homogenization to determine the representative volume element size of paper". In: *PAMM* 22.1 (2023), e202200226.

[53] A. Brandberg et al. "Characterization and impact of fiber size variability on the mechanical properties of fiber networks with an application to paper materials". In: *International Journal of Solids and Structures* 239 (2022), p. 111438.

[54] V. Tojaga et al. "Modeling multi-fracturing fibers in fiber networks using elastoplastic Timoshenko beam finite elements with embedded strong discontinuities—Formulation and staggered algorithm". In: *Computer Methods in Applied Mechanics and Engineering* 384 (2021), p. 113964.

[55] AS. Shahsavari and RC. Picu. "Size effect on mechanical behavior of random fiber networks". In: *International Journal of Solids and Structures* 50.20-21 (2013), pp. 3332–3338.

[56] A. Kulachenko and T. Uesaka. "Direct simulations of fiber network deformation and failure". In: *Mechanics of Materials* 51 (2012), pp. 1–14.

[57] A. Torgnysdotter et al. “The link between the fiber contact zone and the physical properties of paper: a way to control paper properties”. In: *Journal of Composite Materials* 41.13 (2007), pp. 1619–1633.

[58] Y. Li et al. “Evaluation of the out-of-plane response of fiber networks with a representative volume element model”. In: *Tappi J* 17.6 (2018), pp. 329–339.

[59] M. Fallah, H. Zarei, and M. Paggi. “A novel in-situ micromechanical testing of paper fracture and its stochastic network model”. In: *International Journal of Solids and Structures* 300 (2024), p. 112930.

[60] M. Alava and K. Niskanen. “The physics of paper”. In: *Reports on progress in physics* 69.3 (2006), p. 669.

[61] YB. Yi, L. Berhan, and AM. Sastry. “Statistical geometry of random fibrous networks, revisited: waviness, dimensionality, and percolation”. In: *Journal of applied physics* 96.3 (2004), pp. 1318–1327.

[62] CTJ. Dodson and WW. Sampson. “Spatial statistics of stochastic fiber networks”. In: *Journal of Statistical Physics* 96 (1999), pp. 447–458.

[63] LH. Groom, L. Mott, and S. Shaler. “Mechanical properties of individual southern pine fibers. Part I. Determination of variability of stress-strain curves with respect to tree height and juvenility”. In: *Wood and Fiber Science 34 (1): 14-27* (2002).

[64] F. El-Hosseiny and DH. Page. “The mechanical properties of single wood pulp fibres: theories of strength”. In: *Fibre Science and Technology* 8.1 (1975), pp. 21–31.

[65] S. Johansson et al. “Microscale deformation mechanisms in paperboard during continuous tensile loading and 4D synchrotron X-ray tomography”. In: *Strain* 58.5 (2022), e12414.

[66] A. Marengo. “The phase-field modeling of fracture evolution in ductile materials with application to paperboard mechanics”. PhD thesis. Polytechnic University of Milan, 2022.

[67] A. Gizzi, M. Vasta, and A. Pandolfi. “Modeling collagen recruitment in hyperelastic bio-material models with statistical distribution of the fiber orientation”. In: *International Journal of Engineering Science* 78 (2014), pp. 48–60.

[68] X. He and J. Lu. “Explicit consideration of fiber recruitment in vascular constitutive formulation using beta functions”. In: *Journal of the Mechanics and Physics of Solids* 163 (2022), p. 104837.

[69] K. Li and GA. Holzapfel. “Multiscale modeling of fiber recruitment and damage with a discrete fiber dispersion method”. In: *Journal of the Mechanics and Physics of Solids* 126 (2019), pp. 226–244.

[70] S. Borodulina et al. “Stress-strain curve of paper revisited”. In: *Nordic pulp & paper research journal* 27.2 (2012), pp. 318–328.

[71] C. Borri et al. “Adhesive behaviour of bonded paper layers: Mechanical testing and statistical modelling”. In: *Proceedings of the Institution of Mechanical Engineers, Part C: Journal of Mechanical Engineering Science* 230.9 (2016), pp. 1440–1448.

[72] M. Paggi and J. Reinoso. “An anisotropic large displacement cohesive zone model for fibrillar and crazing interfaces”. In: *International Journal of Solids and Structures* 69 (2015), pp. 106–120.

[73] G. Kloppenburg et al. “Identifying microstructural properties of paper”. In: *PAMM* 23.3 (2023), e202300251.

[74] K. Niskanen. *Mechanics of paper products*. Walter de Gruyter, 2011.

[75] Y. Li et al. “multiscale modeling of paper”. In: *17th European Conference on Composite Materials* (2016).

[76] HL. Cox. “The elasticity and strength of paper and other fibrous materials”. In: *British journal of applied physics* 3.3 (1952), p. 72.

[77] S. Pradhan, A. Hansen, and BK. Chakrabarti. “Failure processes in elastic fiber bundles”. In: *Reviews of modern physics* 82.1 (2010), pp. 499–555.

[78] NM. Pugno, F. Bosia, and T. Abdalrahman. “Hierarchical fiber bundle model to investigate the complex architectures of biological materials”. In: *Physical Review E—Statistical, Nonlinear, and Soft Matter Physics* 85.1 (2012), p. 011903.

[79] K. Schulgasser. “Fibre orientation in machine-made paper”. In: *Journal of materials science* 20.3 (1985), pp. 859–866.

[80] T. Wahlstrom. “Influence of shrinkage and stretch during drying on paper properties”. In: 1999. URL: https://api.semanticscholar.org/CorpusID:202200828.

[81] S. Johansson et al. “3D strain field evolution and failure mechanisms in anisotropic paperboard”. In: *Experimental Mechanics* 61.3 (2021), pp. 581–608.

[82] MA. Hubbe, RA. Venditti, and OJ. Rojas. “What happens to cellulosic fibers during papermaking and recycling? A review”. In: *BioResources* 2.4 (2007), pp. 739–788.

[83] J. Kouko et al. “Effect of mechanically induced micro deformations on extensibility and strength of individual softwood pulp fibers and sheets”. In: *Cellulose* 26 (2019), pp. 1995–2012.

[84] HR. Motamedian, AE. Halilovic, and A. Kulachenko. “Mechanisms of strength and stiffness improvement of paper after PFI refining with a focus on the effect of fines”. In: *Cellulose* 26 (2019), pp. 4099–4124.

[85] M. Fallah, P. Lenarda, and M. Paggi. “Nonlinear anisotropic hypoelastic continuum models for paper materials and their relation to statistical micro-mechanics”. In: *Engineering Fracture Mechanics* (2025), p. 111325.

[86] A. Marengo et al. “An in-plane phase-field ductile fracture model for orthotropic paperboard material”. In: *International Journal of Solids and Structures* 294 (2024), p. 112763.

[87] GA. Holzapfel and RW. Ogden. “An arterial constitutive model accounting for collagen content and cross-linking”. In: *Journal of the Mechanics and Physics of Solids* 136 (2020), p. 103682.

[88] AF. Bauer. *Applied Mechanics of Solids*. CRC Press, 2009, p. 794. URL: https://solidmechanics.org/.

[89] A. Freed. “Anisotropy in hypoelastic soft-tissue mechanics, II: simple extensional experiments”. In: *Journal of Mechanics of Materials and Structures* 4.6 (2009), pp. 1005–1025.

[90] G. Baum, D. Brennan, and C. Habeger. “Orthotropic elastic constants of paper”. In: *Tappi J.* 54.8 (1981), pp. 97–101.

[91] F. Hecht. “New development in FreeFem++”. In: *Journal of Numerical Mathematics* 20.3-4 (2012), pp. 251–266.

[92] M. Farzana, M. Haque, SM. Sonali, et al. “Thermo-Mechanical Properties and Applications of Glass Fiber Reinforced Polymer Composites”. In: *Mod Concept Material Sci* 5.3 (2023), pp. 1–9.

[93] KM. Entwistle et al. “Review: Current international research into cellulosic fibers and composites”. In: *Journal of Materials Science* 36 (2001), pp. 2107–2131.

[94] N. Lu, RH. Swan Jr, and I. Ferguson. “Composition, structure, and mechanical properties of hemp fiber reinforced composite with recycled high-density polyethylene matrix”. In: *Journal of Composite Materials* 46.16 (2012), pp. 1915–1924.

[95] A. Shahzad. “Hemp fiber and its composites–a review”. In: *Journal of Composite Materials* 46.8 (2012), pp. 973–986.

[96] A. Moudood et al. “Flax fiber and its composites: An overview of water and moisture absorption impact on their performance”. In: *Journal of Reinforced Plastics and Compososites* 38.7 (2019), pp. 323–339.

[97] Sh. Islam and B. Hasan. “An overview of the effects of water and moisture absorption on the performance of hemp fiber and its composites”. In: *SPE Polymers* 6.1 (2025), e10167.

[98] SJ. Eichhorn et al. “Current international research into cellulosic fibres and composites”. In: *Journal of Material Science* 36.9 (2001), pp. 2107–2131.

[99] MS. Islam, KL. Pickering, and NJ. Foreman. “Influence of alkali treatment on the interfacial and physico-mechanical properties of industrial hemp fibre reinforced polylactic acid composites”. In: *Composites, Part A* 41.5 (2010), pp. 596–603.

[100] M. Paggi. “Mechanics of complex network materials: A formulation based on phase field damage evolution on graphs”. In: *Computer Methods in Applied Mechanics and Engineering* 450 (2026), p. 118637.

[101] M. Kaplan et al. “Fibre joint modifications and their effect on the mechanics of thin cellulose fibre network materials”. In: *International Journal of Solids and Structures* 332 (2026), p. 113932.

[102] G.A. Holzapfel and R.W. Ogden. “An arterial constitutive model accounting for collagen content and cross-linking”. In: *Journal of the Mechanics and Physics of Solids* 136 (2020), p. 103682.

[103] S. Teichtmeister and G.A. Holzapfel. “A constitutive model for fibrous tissues with cross-linked collagen fibers including dispersion — With an analysis of the Poynting effect”. In: *Journal of the Mechanics and Physics of Solids* 164 (2022), p. 104911.

[104] A. Pandolfi and M.L. De Bellis. “Continuum versus micromechanical modeling of corneal biomechanics”. In: *Mechanics of Materials* 199 (2024), p. 105162.

[105] M.L. De Bellis et al. “Modeling the deterioration of the stiffness and of the collagen fibril distribution in a discrete model of the cornea microstructure”. In: *International Journal of Non-Linear Mechanics* 163 (2024), p. 104736.

[106] R. Alberini et al. “A discrete fiber dispersion model with octahedral symmetry quadrature for mechanical analyses of skin corrective surgeries”. In: *Computer Methods in Applied Mechanics and Engineering* 438 (2025), p. 117809.